TRANSOM STERN HYDRODYNAMICS

by

Kevin John Maki

A dissertation submitted in partial fulfillment
of the requirements for the degree of
Doctor of Philosophy
(Naval Architecture and Marine Engineering)
in The University of Michigan
2006

Doctoral Committee:

Professor Armin W. Troesch, Chair
Professor Robert F. Beck
Professor Marc Perlin
Professor Bram Van Leer

ACKNOWLEDGEMENTS

I am grateful to a long list of many people that have positively influenced my life and therefore this thesis.

Specifically I must acknowledge my advisor Armin Troesch whose impact on my experience in engineering far outreaches the scope of this thesis. I would like to thank my other committee members, Robert Beck, Marc Perlin, and Bram van Leer for their service in aiding the compilation of this thesis.

A significant event in the course of my doctoral studies was my time spent at INSEAN in Rome, Italy. I want to thank Alessandro Iafrati who invited me, organized all logistical matters, and then generously shared his knowledge, time, and code with me.

Additionally, I am grateful for the assistance from Lawrence Doctors and his advice on many of the topics in this thesis.

TABLE OF CONTENTS

LIST OF FIGURES

Figure

LIST OF TABLES

Table

LIST OF APPENDICES

Appendix

CHAPTER 1

INTRODUCTION

The transom stern is a popular design choice found in all types of marine vessels. The truncated shape was found originally on planing recreational craft over 100 years ago, and was adopted during the Second World War for use on military vessels. More recently, the family of vessels incorporating the transom stern has grown to include commercial ships, particularly high-speed ferries and those ships propelled by a water-jet.

The advantages of this design feature are varied and not completely understood. Pleasure craft enjoy the extra usable interior volume, and the wide transom may improve the dynamic stability characteristics when running at high speed (planing). Military vessels use the transom stern for weight savings, manufacturing efficiency, and possible resistance reduction in the speed range of vessel operation. More recently, the transom stern has enabled small vehicle recovery through a docking bay in larger military vehicles.

The presence of the transom stern while providing operational benefits, introduces new challenges for the designer to predict performance characteristics. Particularly, the speed range in which the transom is partially wet, is difficult to model for a full-scale ship. When the transom is only partially ventilated, the stream wise dis-

continuity in the hull geometry either creates a viscous *dead-water* region, or with sufficient speed, allows for clean *separation* of the flow. This phenomenon of transom un-wetting therefore has many features that are governed by viscous forces. The current methods of predicting the performance of a full-scale ship, i.e. numerical simulation and model experiments, are plagued by modeling the full-scale effect of viscosity.

One set of present numerical methods are conducted using methods based on a velocity potential. These methods provide efficient predictions of wave resistance, but the inclusion of viscosity is completed *posteriori*. For these methods, the location of the free surface on the transom must be modeled. Only then do potential flow methods provide accurate predictions of wave resistance. To complete the resistance estimate, the viscous drag is modeled using experimental data. In fact, the viscous drag of a ship is important at all operating speeds, and is proportionally more important at low and high speeds. Therefore the quality of viscous resistance estimation can overpower the accuracy of sophisticated wave resistance calculations.

The prediction of full-scale viscous drag is difficult due to the disparity in Reynolds number between model and full-scale bodies. Viscous drag is sensitive to boundary layer separation, which is highly Reynolds number dependent. Not only is the prediction of the separation point on the body difficult, it is important as is shown by Milgram (1969). The inclusion of a transom stern further complicates viscous drag reduction, because the truncated shape converts a previously streamlined body to a blunt body.

While research has been conducted numerically and experimentally for many years, specific studies on the physics of the flow in the transom region have been limited. This thesis is a collection of experimental and numerical investigations of

the hydrodynamics of the aft/wake region of transom stern vessels.

1.1 Background

Early experimental research was first documented by Saunders (1957). His experimental observations suggest that the transom stern is advantageous for resistance reduction at speeds greater than that at which the transom ventilates (or the transom becomes dry). He suggests that the speed at which ventilation occurs is a transom Froude number in the range of 4.0 - 5.0. The transom Froude number is defined as $F_T = U/\sqrt{gT}$, with U being the vessel speed, and T is the transom draft.

The idea to model the transom stern as the two-dimensional flow past a semi-infinite body with constant draft was presented with the analytic work of Vanden Broeck and Tuck (1977). They use a velocity potential and solve for the free-surface by power-series expansion using a parameter related to the transom Froude number. Their free-surface solution is valid for very low Froude numbers, but the singularity at the transom free-surface intersection rises up the transom with increasing speed as it is a stagnation point, and this contradicts reality.

To supplement Vanden Broeck and Tuck (1977), Vanden Broeck (1980) contributes a solution for the free surface behind the semi-infinite body assuming the transom is dry. The combination of this high-speed solution and the previous low-speed solution leads to the conjecture that the transom ventilates at the speed at which the two solutions coincide. Curiously, the high speed solution reaches the critical breaking value of wave steepness ($s_{\text{crit}} = 2a/\lambda = 0.141$) at a transom draft Froude number of 2.26. The Froude number at which the two solutions coincide is near 2.7, where the wave steepness is approximately half the critical steepness, i.e. $s = 0.07$.

Next, Oving (1985) states that an immersed transom contributes to the resistance as the simple hydrostatic pressure integration (a thrust force) on the transom. For partial ventilation, the pressure is integrated from the keel to the mean dynamic free-surface on the transom. He hypothesizes that the process of the transom un-wetting is proportional to the square of the velocity.

Further theoretical analysis of the resistance of transom stern vessels is presented in Tulin and Hsu (1986). Here a new theory that assumes the ship is slender, solves a series of cross-plane boundary-value problems that represent stations along the hull. Good agreement with model experiments is shown, and results specifically suggest the design of the transom can significantly alter the resistance of the ship. Furthermore, it is reported in Wang et al. (1995) that the method of Tulin and Hsu (1986) compares well with experimental results for high Froude numbers, i.e. $F_N > 0.9$ (where F_N is the Froude number calculated with ship length).

An interesting modification to the transom stern that significantly affects the resistance of the vessel is the stern flap or wedge. A stern wedge can be recognized as a discontinuity in the hull buttock near the transom (usually located within 3% LWL of the transom). A flap results in a similar hull shape but is achieved by adding a downward angled extension to the transom. The impact of such appendages is significant on ship performance; Karafiath and Fisher (1987) shows that the the powering requirements can be reduced on the order of 10% relative to the un-appended configuration. The effects are highly dependent on the operating speed of the ship, so a resistance increase is usually realized for low Froude numbers. These appendages have been outfitted on numerous classes of naval vessels, including the FFG, DDG, and the CG. Though the experimental and full-scale trial documentation is extensive, e.g. Cusanelli, Chang III, and McGuigan (1995), among others, the physics of

resistance reduction is still not well understood.

Full body numerical simulations of the transom stern R/V Athena are presented in Cheng (1989). To calculate wave resistance, he uses a potential flow formulation, assumes that the transom is dry, and uses boundary conditions stating the flow exits tangentially at the transom and the pressure is atmospheric on the free-surface behind the vessel. The results as compared to experiment are agreeable for high speeds ($F_N > 0.35$), but differ noticeably for slower speeds. This is presumably because the assumption of a dry transom is violated at low speeds.

Subsequently, Reed et al. (1991) and Telste and Reed (1993) use potential flow theory and implement special panelizations on the free surface aft the transom to deal with the truncated hull form. They present results for the R/V Athena as well as the destroyer type hull DTMB Model 5415. Their results demonstrate the ability to solve for the free-surface of a transom stern vessel, but comparison of transverse wave spectra and longitudinal wave cuts are marginal.

Another treatment of the transom stern with potential flow theory is to consider that the transom stern creates a hollow or depression in the free-surface behind the vessel. To achieve the effect of a hollow, several methodologies have been developed with the basic result of adding extra singularities in the wake, e.g. Doctors and Day (1997), Couser et al. (1998), Doctors and Day (2000). These implementations necessitate further modeling of the *hollow* and assume a dry transom and therefore yield varied results.

A paper by Doctors (1999) investigates the influence of the transom stern on wave resistance. In this paper, simulations are performed on three vessels with three different stern geometries, namely a canoe stern, a full transom stern, and a blend of the two resulting in a *half*-transom stern. His findings show that the transom stern

shape has the smallest wave resistance.

To address the low speed operating range when the transom is partially wetted, Doctors (2003) introduces a model to determine the stage of ventilation in which the vessel is operating. He models the ventilation as a balance between the free-surface height in the hollow and the dynamic pressure in the outer flow of the body, i.e. the Bernoulli Equation. The coefficients for the model, which is quadratic in vessel speed, are determined by using a regression analysis on free-surface elevation measurements in the transom wake. When the model is implemented into a potential flow solver, the resistance predictions are greatly improved, but the applicability to ship types and Reynolds numbers outside the experimental dataset is unknown.

More sophisticated numerical simulations attempt to solve the non-linear Navier-Stokes equations. These techniques, popularly referred to as RANS (Reynolds Averaged Navier-Stokes), are computationally much more expensive than the velocity potential methods and therefore their use has been limited to research applications and a far fewer number of ship types. Unfortunately, while the viscous drag prediction is directly incorporated into the calculation in a RANS simulation, the complex turbulence is included via simple modeling, and therefore suffers like laboratory-scale experiments and potential flow methods from poor viscous drag prediction.

The state of the art of RANS methods is summarized in Larsson, Stern, and Betram (2003). This reference documents the results from the the benchmarking Gothenburg 2000 Workshop. Here simulations on three test cases, one of which was the transom stern model of the David Taylor Model Basin model 5415, were conducted by various international research institutions. The treatment of the transom stern is not specifically mentioned, but the agreement between the different participating bodies shows need for further development for these methods.

More recently, Wilson and Stern (2005) provides model-scale RANS simulations of the R/V Athena at two Froude numbers, one of which is at a speed with a partially wetted transom. The resistance predictions are within experimental accuracy, and more interestingly, specific comments on the flow in the transom are provided. It is shown that the unventilated transom results in a highly unsteady free-surface behavior in the near wake. It should be noted that this methodology needs no modeling to address the transom stern; the numerical results implicitly handle the given geometry.

1.2 Present Objectives

Considering the present state of transom stern hydrodynamics, the following questions were stated at the beginning of the research for this thesis.

1. At what speed does a transom fully ventilate? What are the important geometrical parameters that influence the un-wetting? What role does the Reynolds number play in the process of un-wetting?

2. What effects does the transom stern have on the wave pattern behind a vessel? What types of unsteadiness are introduced by the transom stern? What role does viscosity have in the development of residual transom waves?

3. How accurately can present state-of-the-art numerical methods predict the flow behind a transom stern? Are these methods realistic? What are their strengths and disadvantages?

This thesis addresses the above three areas and is organized as follows:
In the midst of investigating the process of un-wetting, it became clear that an understanding of the pressure distribution on the hull near the transom was not

well understood. A series of model tests on a 1:24.8 scale destroyer are undertaken. In these tests, pressures on the hull are measured in the transom region on the center-plane and two buttocks corresponding to the shaft buttock and the half-shaft buttock. To investigate the effects of a stern-flap, these tests are repeated with a 10 degree trailing edge down, and 1 % length of waterline flap. Chapter 2 describes the experimental setup and shows representative results from the measurements. The pressure measurements taken near the transom are given in comparison to the free-surface measurements made on a backward-facing step with a free-surface in chapter 5.

Next, experiments in the Low-Turbulence Free-Surface Water Channel (LTF-SWC) investigate the canonical problem of a backward facing step with a free-surface (BFSFS). This problem is a model of an infinite-beam transom stern, and has never before been studied experimentally. The experimental set-up and various measurement techniques will be described in chapter 3.

A two-dimensional, unsteady Navier-Stokes solver is used to make comparisons to the experimental data of the BFSFS. The numerical method developed by Alessandro Iafrati of *INSEAN* uses the level set method for interface capturing, and the Spalart-Allmaras turbulence model is added to solve the Reynolds averaged equations. Chapter 4 contains the details of the method, the boundary and initial conditions used for test cases simulated, as well as the grid convergence study.

Chapter 5 contains results and discussions of the BFSFS experiments and simulations. The general behavior of the free-surface is described in the context of four flow regimes. A detailed analysis of the location of the free-surface on the body is conducted with comparisons to the pressure measurements on the destroyer model. Also a frequency domain analysis is presented to describe an interesting vortex shed-

ding phenomenon. Throughout this chapter, numerical results will be compared to the experiments.

Finally, chapter 6 contains the conclusions and contributions of this thesis. The aforementioned questions are addressed, and suggestions for further work are offered.

CHAPTER 2

HULL PRESSURES IN THE PRESENCE OF A STERN FLAP

Many high speed marine vessels benefit and are fitted with stern flaps, wedges or trim tabs. Positive attributes associated with this style of appendages are resistance reduction, improved propeller cavitation characteristics, increased top speed, control of sinkage and trim, and reduced or altered wake signature, among other effects.

In the interest of design, model experiments have been conducted for many years because numerical tools are underdeveloped for this unsteady, turbulent region of the flow. Model tests successfully predict the resistance benefit of the flap, but the accuracy of the extrapolation suffers from little understood scaling issues.

While the number of tests over the years on various flaps are large, detailed pressure on the hull and flap near the stern have never been documented. A set of experiments was conducted at the University of Michigan Marine Hydrodynamics Laboratory (MHL) to investigate the effect of a stern flap on hull pressures near the stern.

A model of the United States Navy CG-47 class cruisers was tested with a flap of 10 deg trailing edge down relative to the centerline buttock, and length of 1% LBP. Pressure taps were fitted to the hull along the centerline, propeller shaft, and half-propeller shaft buttock planes to 15% LBP forward the transom. In the first

set of experiments the model was free to sink and trim while pressure, heave, trim, and resistance were measured. Another set of runs were conducted with the model fixed in sinkage and trim, while measuring the same quantities with exception of resistance. The model was towed at seven different speeds corresponding to a range of 10-34 knots full scale.

In this chapter a subset of the hull pressure data is presented in section 2.2. Additional data from the destroyer experiments are used for a detailed analysis of transom un-wetting in chapter 5.

2.1 Model Description

The experiments described here were conducted in the main model basin of the MHL with UM model 1550 (see the body plan in figure 2.3). The fiberglass model was constructed with a length scale factor of 24.842, and was ballasted to 9800 tons (1395.4 lbs or 632.9 kg model scale) corresponding to the CG-47 class. The model was towed un-appended except for the centerline skeg, with a full-scale trim of 0.5ft (0.152 m) bow down. To stimulate turbulence, studs of 0.432 cm diameter and 0.254 cm high were placed with a spacing of 2.54 cm along the model bow and sonar dome. Principle characteristics of the ship and details of the model can be found in tables 2.1-2.3.

The flap used in these experiments has a length of 1% of LWL and is affixed with an angle relative to the centerline buttock of 10 deg. The span of the flap is 80% of the beam of the transom, with rounded corners (see figures 2.1-2.2).

Pressure taps were placed along the centerline, the propeller shaft ($y/B_x = 0.207$), and half propeller shaft ($y/B_x = 0.104$) buttocks (see lines in figure 2.3). Here y is the transverse coordinate measured from the centerline, and B_x is the maximum

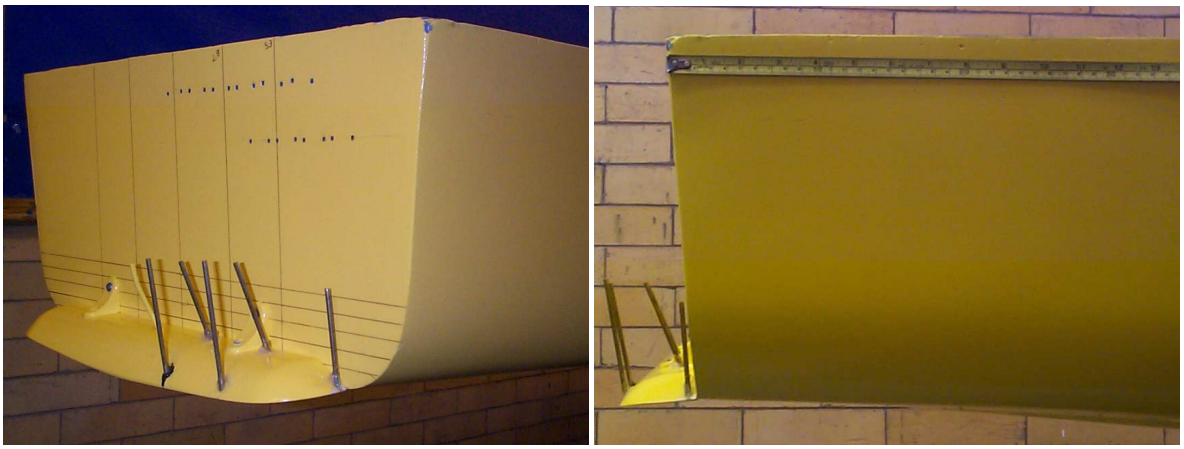

Figure 2.1: Perspective and side view of the transom with flap.

Figure 2.2: Top view of the transom and flap.

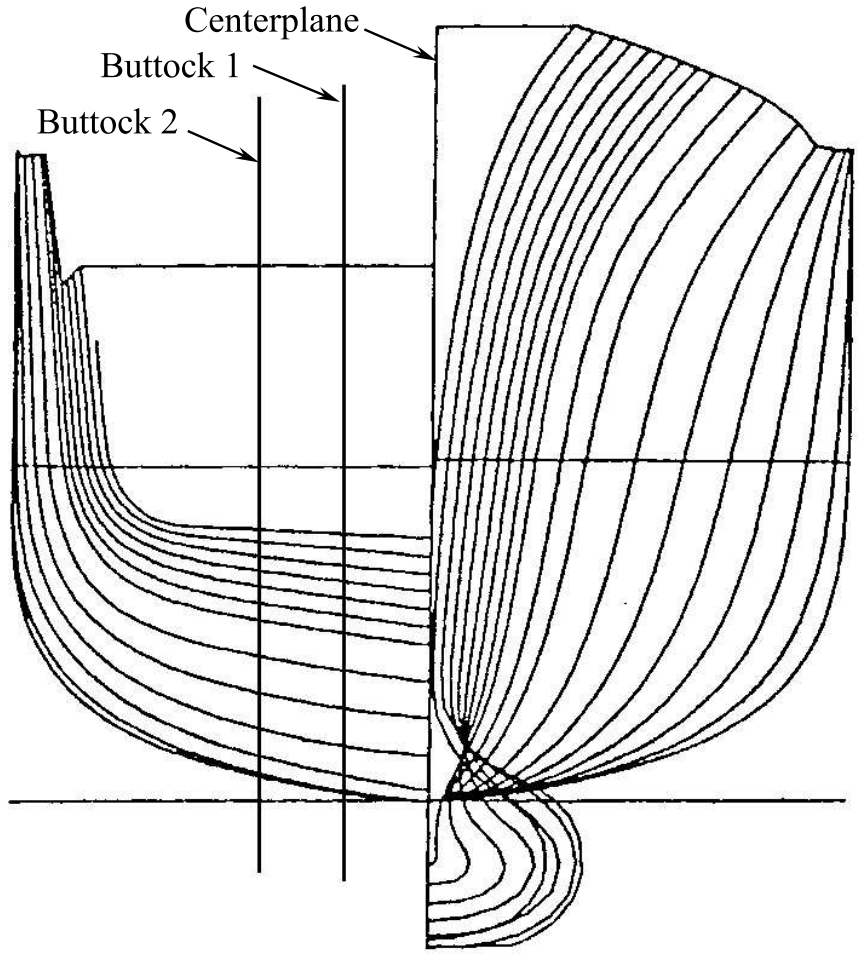

Figure 2.3: Body plan of destroyer model. The three measurement buttock lines are indicated

Length (LBP)	=	530.20 ft. (161.60 m)
Length (LWL)	=	532.93 ft. (162.44 m)
Beam (B_x)	=	54.98 ft. (16.76 m)
Draft (T_x)	=	22.57 ft. (6.91 m)
Trim (+bow↓)	=	0.50 ft. (0.15 m)
Displacement	=	9800.0 T (9957.0 t)
Wetted Surface	=	36490 ft^2 (3389.9 m^2)

Table 2.1: Ship Principal Particulars

Scale Ratio	=	24.824
Length (LBP)	=	21.36 ft. (6.51 m)
Length (LWL)	=	21.47 ft. (6.54 m)
Beam (B_x)	=	2.21 ft. (0.68 m)
Draft (T_x)	=	0.91 ft. (0.28 m)
Displacement	=	1395.4 lbs (632.9 kg)
Wetted Surface	=	59.22 ft^2 (5.50 m^2)

Table 2.2: Destroyer Model Data

C_b	=	0.516	C_p	=	0.603	C_x =	0.856
C_{wp}	=	0.751	L_{wl}/B_x	=	9.592	B_x/T_x =	2.426
A_t/A_x	=	0.196	B_t/B_x	=	0.780	T_t/T_x =	0.247

Table 2.3: Destroyer Nondimensional Coefficients

beam on the waterline. To measure pressure, 0.305 cm i.d. brass tubes were mounted flush to the hull and extended 7.62 cm inside the model. Flexible plastic tubing was used to connect the brass tubes to the sensors which were mounted to the inside of the hull. To measure pressure, diaphragm type transducers from SenSym ICT, model SCX01DN were used. These sensors have a full scale range of 1 psig and use an electrical circuit on a silicon diaphragm to measure strain that is calibrated to applied pressure.

The model was either fixed in all degrees of freedom, or free to heave and pitch while being restrained in yaw with a bow mounted yaw restraint.

The data acquisition system consisted of a 16 bit analog to digital converter with four pole low-pass butterworth filters. All data were collected with a 100 Hz sampling rate and a 50 Hz filter cut-off frequency. The pressures are reported as an average over the *steady-state* portion of the time series. The record length was 40 seconds, and for the highest speed runs, the averaging window is approximately 7 seconds.

2.2 Pressure Distribution Profiles

All of the data presented are nondimensionalized with L_{LWL}, fresh water density at 65 deg F ($\rho = 1.937\frac{lb-s^2}{ft^4}$ or $998.7\frac{Ns^2}{m^4}$), and model scale ship speed.

Figures 2.4-2.10 depict the pressure profile along the hull. The coordinate x is the longitudinal distance from the transom, positive forward. In these figures the model was fixed in sinkage and trim. The pressures reported are relative to the mean calm water hydrostatic. The pressure was measured in unit of inches of water and are also presented here as a pressure coefficient:

$$C_p = \frac{p}{1/2\rho U^2}$$

In each figure, three sets of data are displayed corresponding to each buttock plane. These measurements were repeated with the model free to heave and trim, and the results were characteristically identical. The difference between fixed and free was an offset in pressure due to the local sinkage relative to the mean free surface. The vertical range for each plot is the same in non-dimensional coordinates (printed on the right of each figure). The scale on the left of each figure is that of the respective physical model units corresponding to the non-dimensional scale. The profiles behave similarly for each of the seven speeds indicating the pressure scaling chosen here is appropriate. The error bars represent manufacturer specified uncertainty (see Appendix for discussion on error analysis).

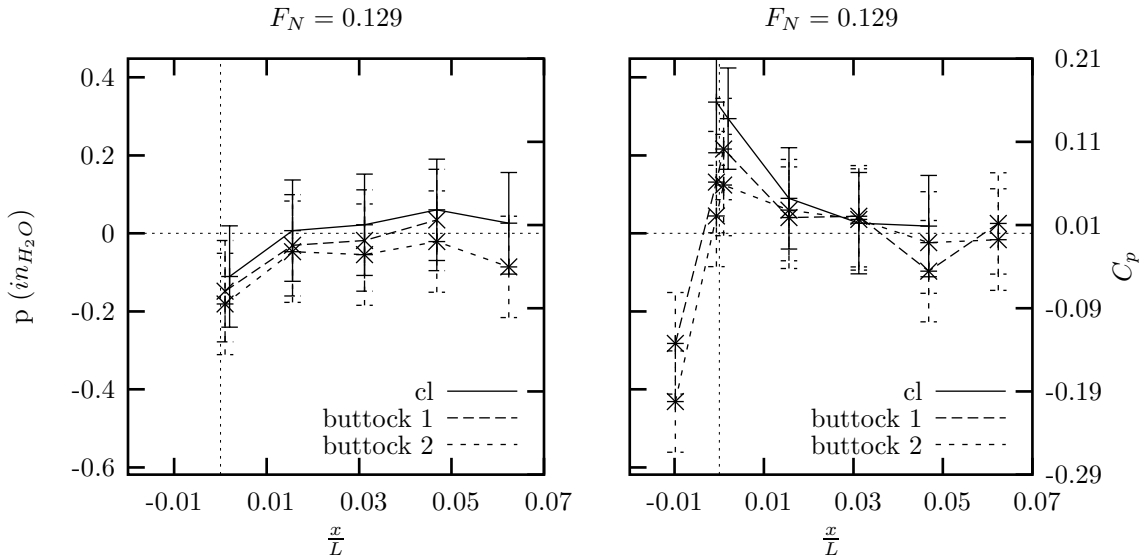

Figure 2.4: Hull pressure, 10 knots, no flap (left), with flap (right), model fixed.

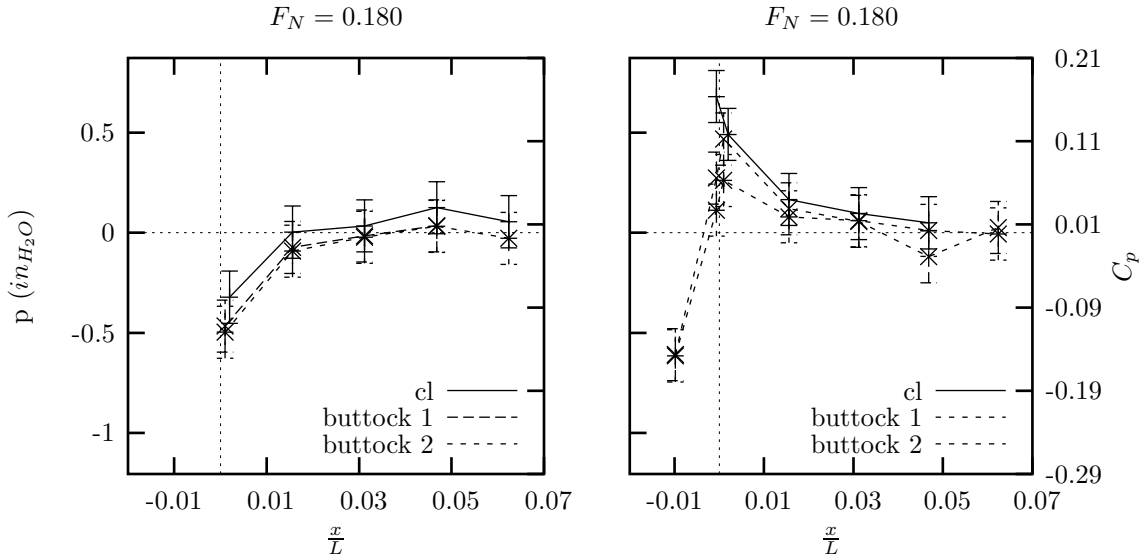

Figure 2.5: Hull pressure, 14 knots, no flap (left), with flap (right), model fixed.

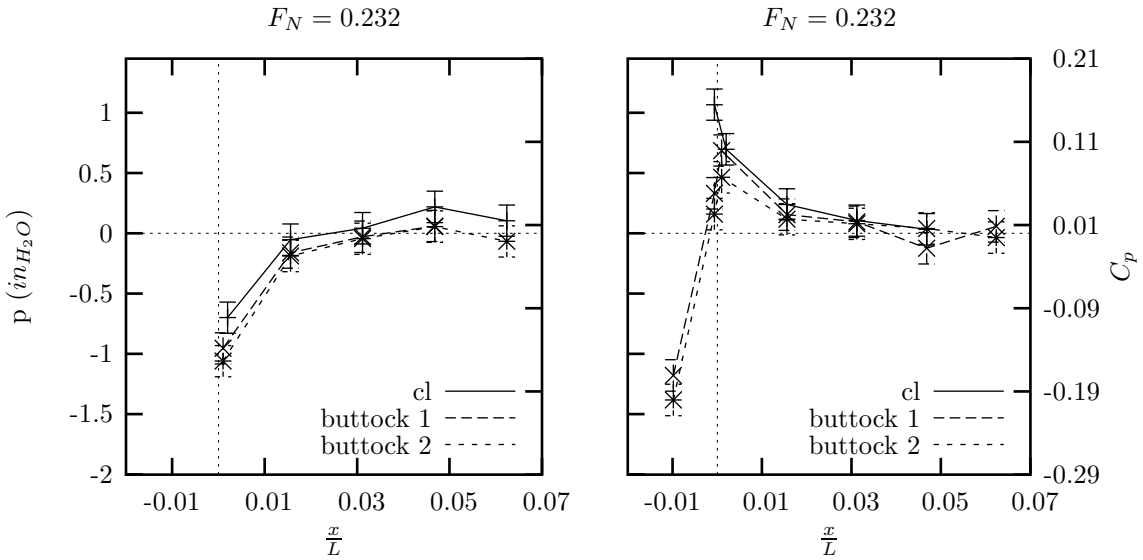

Figure 2.6: Hull pressure, 18 knots, no flap (left), with flap (right), model fixed.

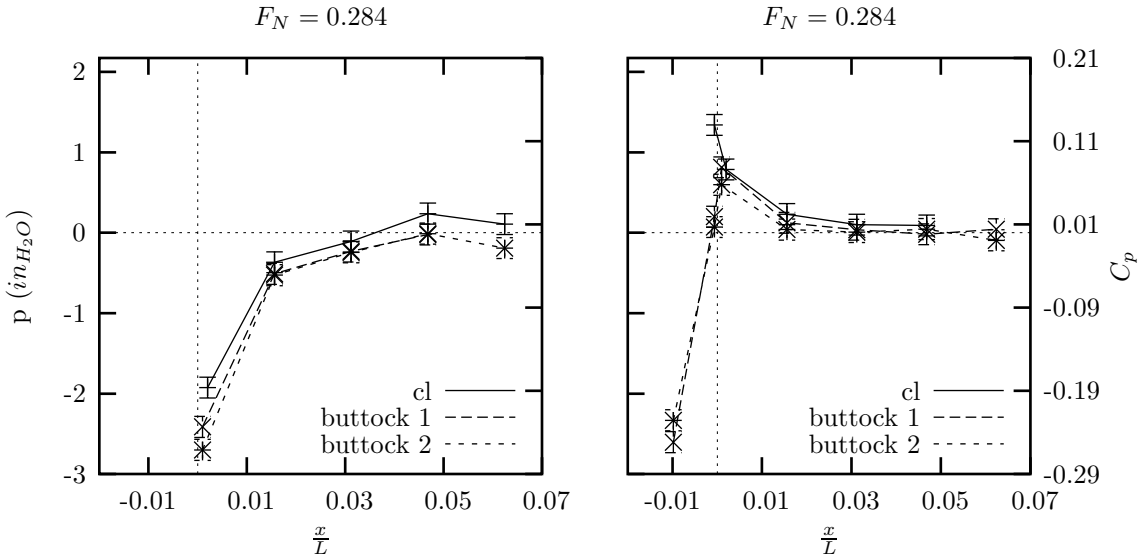

Figure 2.7: Hull pressure, 22 knots, no flap (left), with flap (right), model fixed.

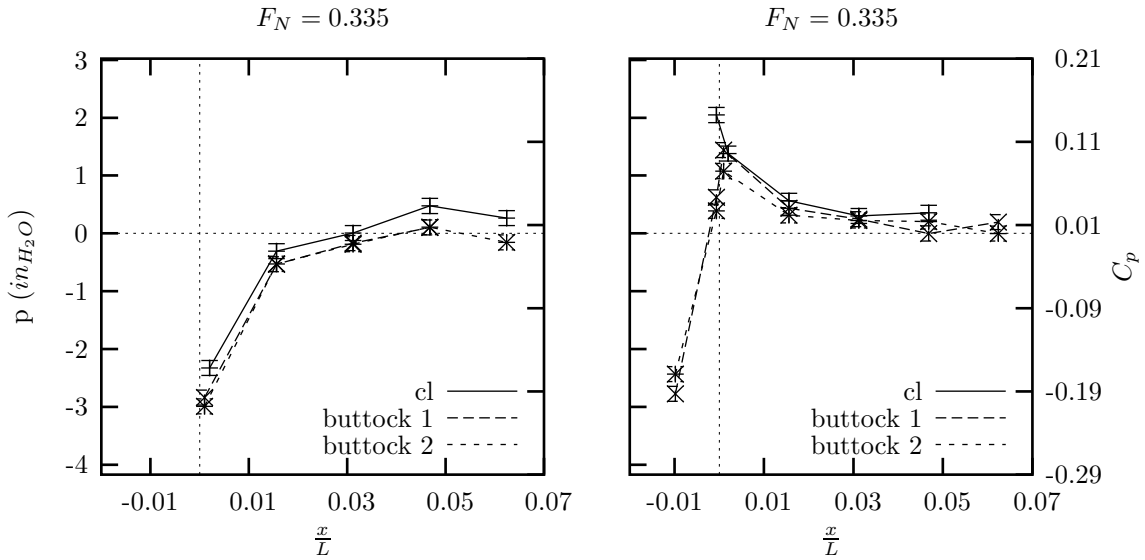

Figure 2.8: Hull pressure, 26 knots, no flap (left), with flap (right), model fixed.

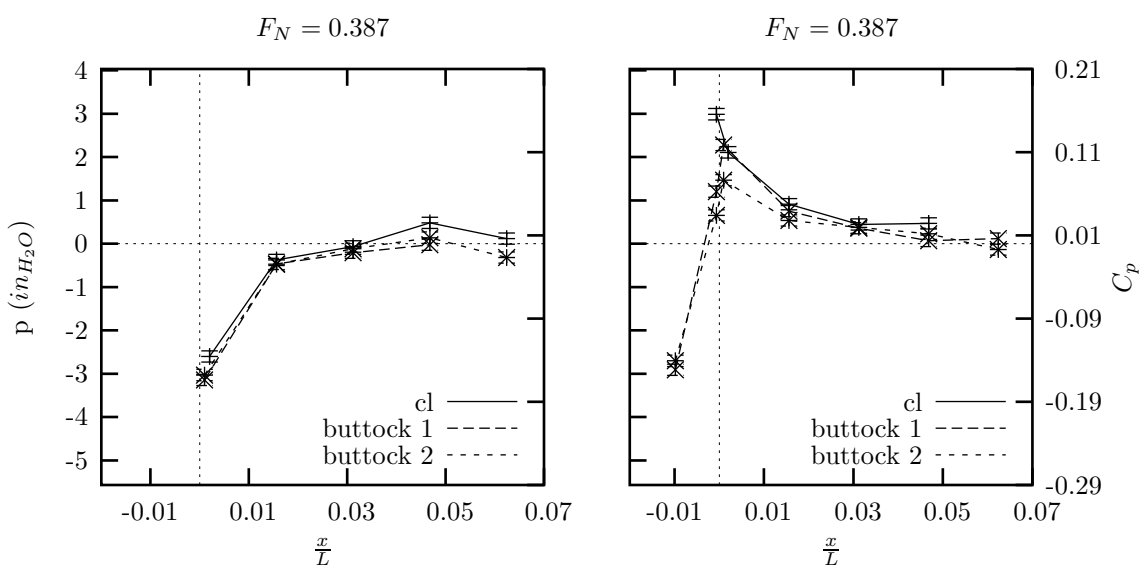

Figure 2.9: Hull pressure, 30 knots, no flap (left), with flap (right), model fixed.

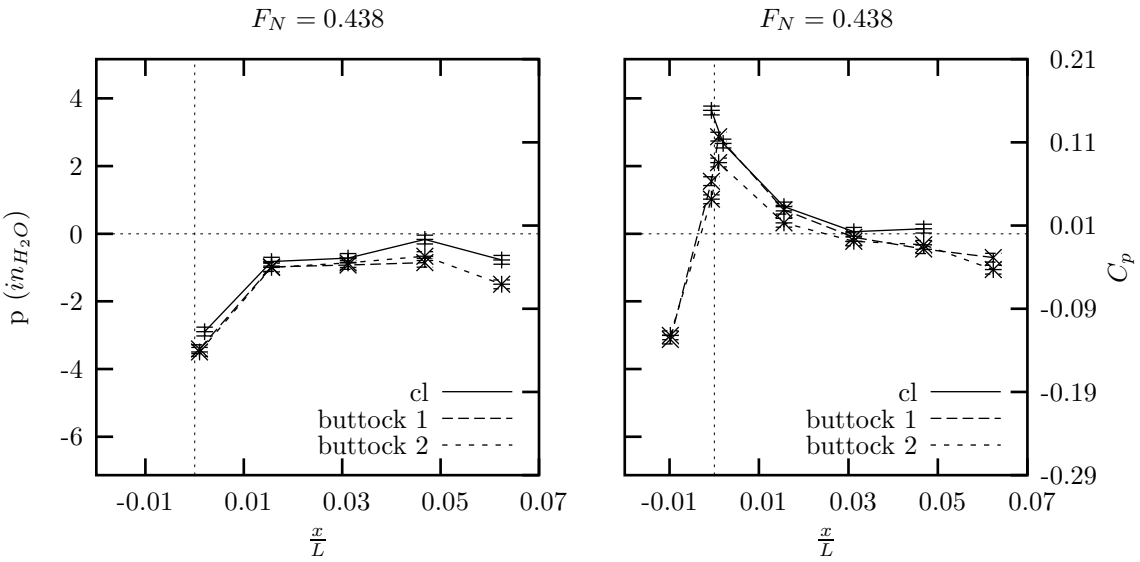

Figure 2.10: Hull pressure, 34 knots, no flap (left), with flap (right), model fixed.

2.3 Summary

Either with or without the flap, the behavior of the pressure profile is similar near the "end of the body". When the transom is fully ventilated, the pressure must return to atmospheric where the body meets the free-surface. In figures 2.4-2.10 the pressure does indeed decrease with increasing Froude number, and after ventilation ($F_N \approx 0.28$) the change in pressure remains relatively constant in absolute units.

Oving (1985) modeled the water on a partially ventilated transom as being purely hydrostatic. A subset of these pressure profiles consisting of the measurements from the aft-most location will be presented again in chapter 5 in comparison to the measurements from the backward-facing step with a free-surface.

Understanding the pressure on the hull of a vessel ultimately leads to the determination of form drag. The process of ventilation (regardless of a transom geometry) counteracts the process of pressure recovery on a body. When a flap is not present, the ventilation overpowers any pressure recovery, and therefore contributes to the drag.

When the flap is present, the pressure increases relative to the calm-water reference value, with the maximum occurring where the flap meets the body. Due to the local buttock angle on the vessel, this pressure recovery ($C_p \approx 0.2$) results in a thrust on the body, reducing resistance. The pressure on the flap, decreases to atmospheric (or some fraction of atmospheric for partial ventilation) consistently with the flapless case. The integrated pressure on the flap is impossible to quantify with only two data points, but it is noted that the buttock angle on the appendage is opposite that of the hull. Therefore, if the integrated pressure is negative, this will result in further drag reduction.

In examining the drag reduction due to a stern flap, many factors are considered to contribute to this positive effect, see Cusanelli, Chang III, and McGuigan (1995), Cusanelli (1998), and Hundrey and Brodie (1998). Amongst the lore, the flap is thought to increase the pressure in the propeller plane, therefore increasing the efficiency of the propeller by warding off cavitation. In the present experiments, the pressure was measured at the longitudinal location of the propeller plane (15%L_{wl} forward the transom). The data between the cases with and without the flap were inconclusive as to whether the flap increases the pressure in the propeller plane.

In chapter 5, the pressure measurements collected at the aft-most location on the body will be used in a transom un-wetting analysis. When the transom is ventilated, it is known that the pressure where the free-surface meets the body is atmospheric. It is hypothesized that when the vessel is partially ventilated, the pressure at the aft-most location represents the mean free-surface elevation on the transom. To evaluate this conjecture, simultaneous free-surface and pressure measurements from the BFSFS will be compared to the destroyer data and will be used to describe the un-wetting of the ship model in chapter 5.

CHAPTER 3

EXPERIMENTS ON A BACKWARD FACING STEP WITH A FREE SURFACE

Experiments were performed on a backward-facing step with a free-surface in the University of Michigan Low-Turbulence Water Channel, located at the Marine Hydrodynamics Laboratory. To describe the backward-facing step with a free-surface (BFSFS), high-fidelity time-accurate free-surface measurements were made. Additionally, mean-velocity profiles in the wake were documented. The free-surface data are used to describe the wave profiles statistically for a large range of Froude number, and the unsteadiness of the free-surface is documented in the frequency domain. This chapter is dedicated to describing the subtle but essential details of the the experimental set-up. The facility and model will be described, the qualification of the channel properties will be presented, and the details of the experimental techniques will be explained.

The recirculating water channel conventionally uses a contraction to accelerate the flow in the test section. Consequently, the free-surface rises in the region of slower velocity before the contraction, and drops in the test section. An understanding of this process is vital in determining the length scale of the problem - the transom draft.

Secondly, as with any channel or tunnel, the velocity is not uniform across the

test section due to the no slip of the fluid at the walls, and any asymmetry of the contraction. In this case, there is a velocity excess near the floor of the test section due to the contraction. Velocity surveys were conducted with a pitot-static tube, and regression analysis used to determine a depth averaged free-stream velocity.

Finally each of the measurement techniques will be described.

3.1 Problem Description

The BFSFS consists of a semi-infinite flat-bottomed body, and a free-surface. A diagram of the body, free-surface, and coordinate systems used are shown in figure 3.1. The problem is described by the length scale T_{d}, which is defined as the distance from the the water's potential energy datum to the bottom of the body. The important physical quantities are the free-stream fluid velocity U, the acceleration due to gravity g, and the air and water kinematic viscosities ν_{air}, ν_{water} and densities ρ_{air}, ρ_{water}.

The non-dimensional parameters used in this study include the transom draft Froude number ($F_T = U/\sqrt{gT_{\mathrm{d}}}$). While conceptually the problem has a semi-infinite body, for these experiments, the body does have a finite length L. Therefore two Reynolds numbers describe the flow, one calculated with the the length of the body ($Re_L = UL/\nu$), and the other with height of the step ($Re_T = UT_{\mathrm{d}}/\nu$). Additionally, the Reynolds numbers in air can also be computed using the ratio between the air and water viscosities, along with the model lengths.

In figure 3.1, two coordinate systems are referenced. To describe the water channel a system (x', y', z') that is fitted to the bottom of the body is the most appropriate. For describing the characteristics of the canonical problem, and for comparing to a ship, a system that is attached to the location where the free-surface intersects the

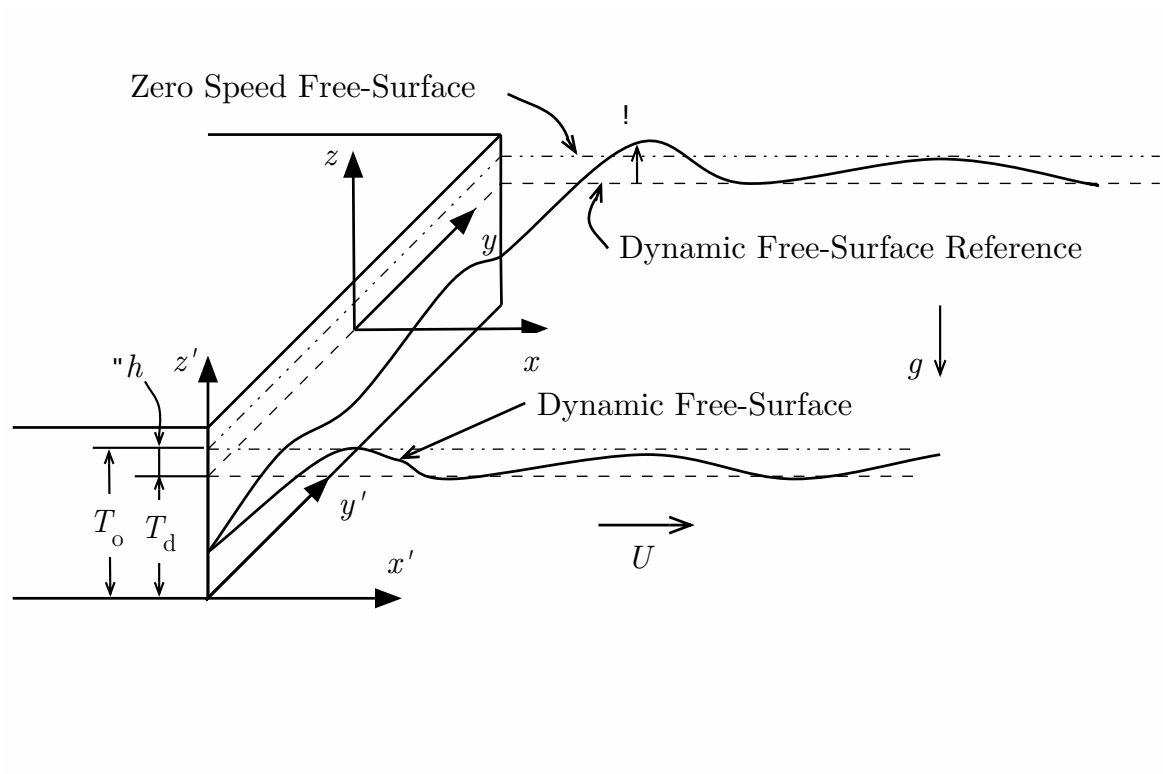

Figure 3.1: Backward Facing Step with Free-Surface flow configuration.

body (x, y, z) is best.

The vertical position of the free-surface above the $x - y$ plane is labeled $\zeta(x, y, t)$, and when it is non-dimensionalized by transom draft, it is reported as $\eta = \zeta/T_{\mathrm{d}}$.

3.2 Description of Water Channel

The low-turbulence water channel is depicted in figure 3.2. This facility, which spans two floors of the laboratory, holds roughly 8000 gallons and is able to achieve speeds in the test section of less than 2 m/s. The flow in the test section is conditioned before the contraction with a 10 cm long honeycomb section, followed by six stainless steel screens spaced at 20 cm. The two-dimensional contraction (in the vertical direction) is approximately 4:1 depending on water depth. The turbulence kinetic energy (k) level in the test section has been documented with a two component

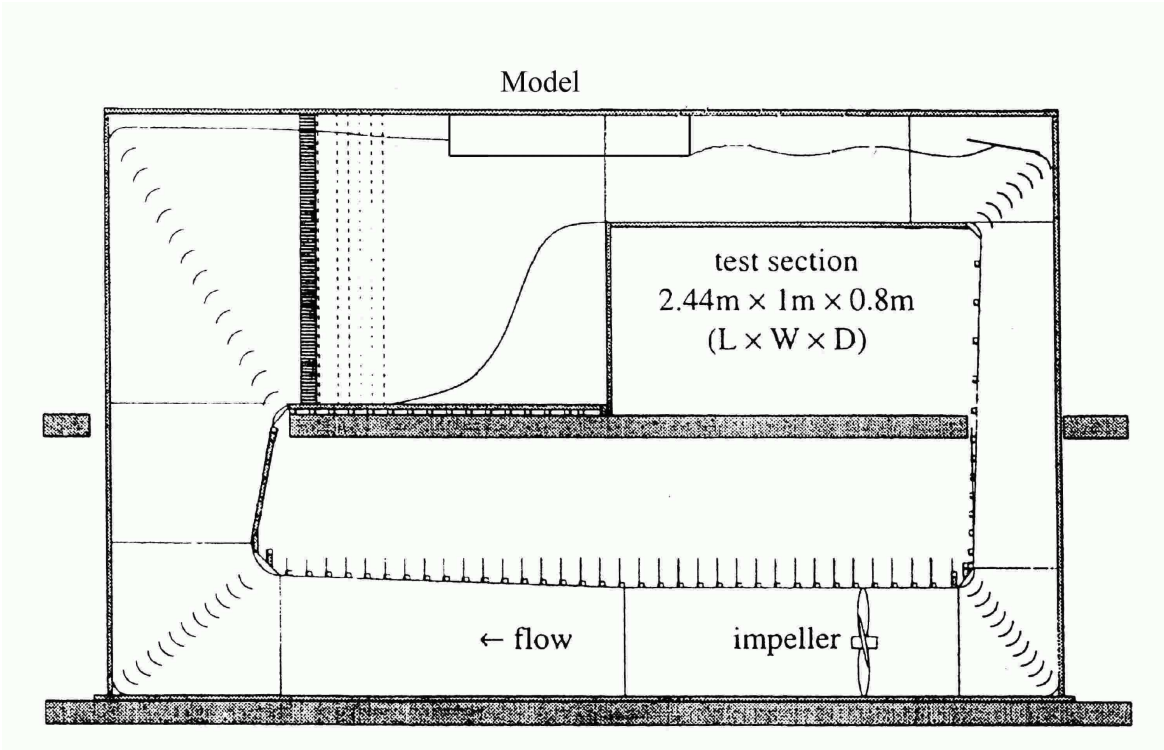

Figure 3.2: Schematic of the recirculating water channel depicting the location of the model in the test section. Taken from Walker et al. (1996).

hot-film anemometer (Walker, Lyzenga, Ericson, and Lund 1996). The turbulence intensity normalized by the free-stream velocity was reported at 0.095%.

The test section is constructed from 2.54 cm thick clear acrylic to allow optic access from the sides and bottom. There is a computer controlled traverse located above the channel. Two rails run along the two sides of the test section, and the traverse has movement in the stream wise, span wise, and vertical directions. Further details on the facility design and construction can be found in Walker (1996).

The model was constructed from 12 mm thick, 9-ply Latvian birch plywood to dimensions of 1.79m x 1.00m x 0.23m (L x W x H). The bottom and sides of the model were covered in fiberglass and epoxy resin. To finish the model, it was primed and painted with a two-part polyurethane manufactured by AWLGRIP ©. The

model was fitted in the tank to extend 0.63 m into the test section, and the keel (or bottom of the box) was 0.503 m above the bottom of the tank. The model was then leveled in the horizontal plane with a machinist level to within 0.035 degrees. The fit between the model and the tank walls would generally be considered as a press-fit, but there were gaps less than 0.5 mm in the forward area of the model before the test section, due to non-zero tolerances of the tank walls.

To stimulate turbulence in the boundary layer of the model, a sand strip of width 2.54 cm was fitted on the forward-most-point of the bottom skin.

3.2.1 Definition of Model Length Scale

In a free-surface water channel, the water level drops in the test section as the speed of the fluid increases (figure 3.3). The steady Bernoulli equation (3.1) written along the streamline of the free-surface between a point before the contraction and a point in the test section is,

$$\frac{1}{2}u_1^2 + gh_1 = \frac{1}{2}u_2^2 + gh_2 \tag{3.1}$$

By assuming a contraction of 1:4 the total change in free-surface height is,

$$h_1 - h_2 \cong \frac{15}{32g}u_2^2 \tag{3.2}$$

For the nominal speed in the test section of 1 m/s, this would yield a total change in elevation of 4.8 cm. In the problem of a backward-facing step with a free-surface, the length scale is defined as the distance from the far field free-surface and the bottom edge of the step. For these experiments, this length ranges from 8 cm to less than 1 cm. The magnitude of the drop, relative to the problem's characteristic length scale, necessitates an accurate measurement of the change in free-surface due to the speed of the flow in the channel.

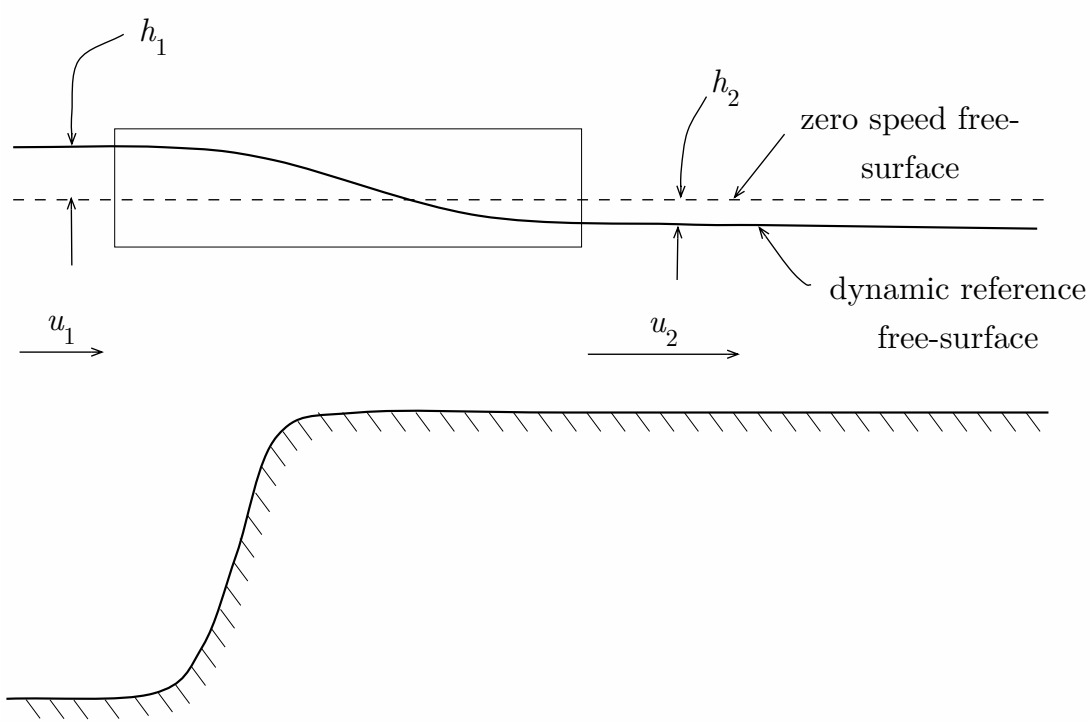

Figure 3.3: Dynamic free-surface in an open water channel.

To determine the vertical change in the free-surface for this specific experiment, the static port on a pitot tube was used. Details of the measurement of the small pressure changes can be found in section 3.3.2. The concept is to calibrate the change in static pressure with the speed in the test section. The next issue is to determine an appropriate location to measure the static pressure in the test section. As will be shown in this thesis, the free-surface behind the model at low speeds is relatively unaffected; as the speed increases, the free-surface becomes highly unsteady, and then at sufficient speed, the free-surface has a steady gravity wave attached to the body. All of these characteristics affect the pressure under the body, and complicate the decision of where to measure the static pressure. Figure 3.4 shows the step with the free-surface, and contours of constant pressure.

In this work, the following process was chosen: starting at a location 1 cm below

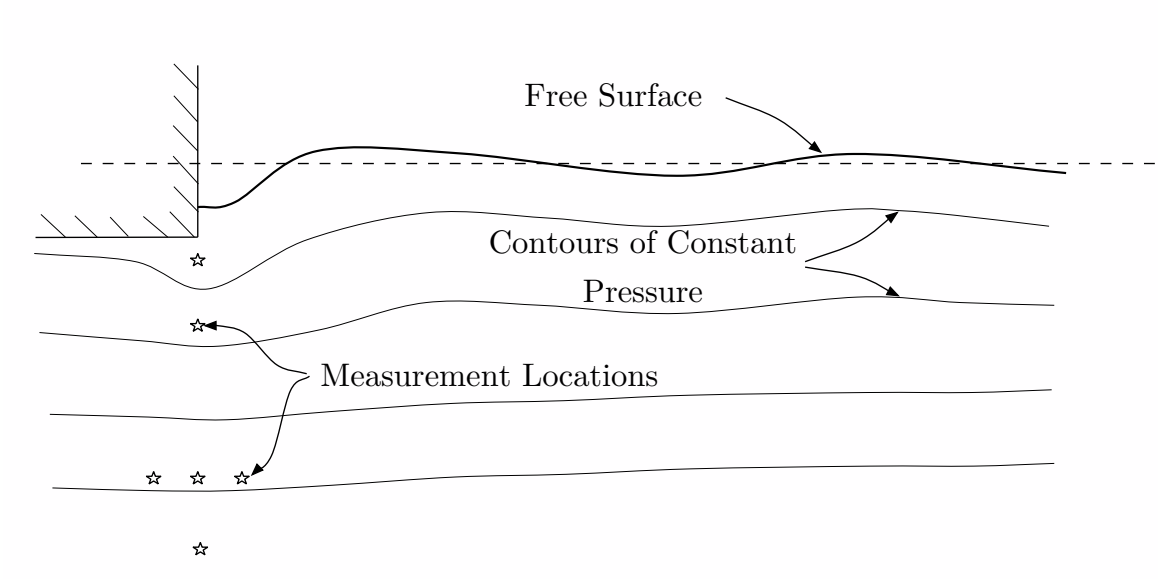

Figure 3.4: Contours of constant pressure along with locations of static pressure measurement.

the bottom of the body, and directly below the aft-most edge, a series of pressure measurements are made throughout the speed range. These data produce a curve shown in figure 3.5. The static probe (which is mounted on the traverse) is moved down to a location 5 cm below the body, and the measurements are repeated. As seen in the figure, the second curve is different, meaning there exists a pressure gradient vertically between the two locations. The probe was moved vertically downward until two successive locations showed the same change in static pressure with channel speed. After an acceptable vertical location was found, the stream wise dependence on static pressure was verified. The probe was moved 3 cm upstream and downstream, and the measurements were repeated. A second order regression equation (3.3), using the change in static pressure (in units of m H_2O) and the frequency counter (Fq : Hz) on the channel drive motor, was fitted using the four later sets of data.

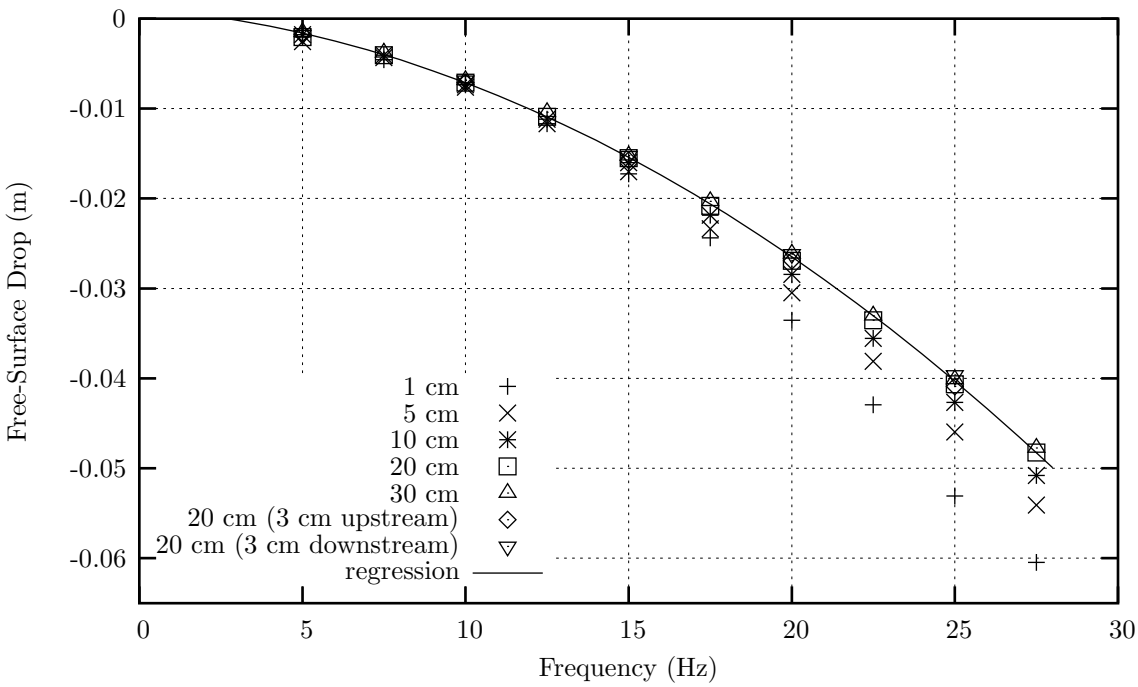

Figure 3.5: Calibration of free-surface drop in the test section as a function of frequency of the drive motor.

$$\delta h(\mathrm{m}) = -5.542 \times 10^{-5}(\mathrm{Fq})^2 - 2.723 \times 10^{-4}\mathrm{Fq} + 1.143 \times 10^{-3} \tag{3.3}$$

The equation to determine the dynamic transom draft T_d is now calculated as the calm-water depth T_o corrected with the change in height δh.

$$T_\mathrm{d} = T_\mathrm{o} + \delta h \tag{3.4}$$

3.2.2 Definition of Free-Stream Velocity

Using a pitot tube, stream wise-velocity surveys were conducted to quantify the uniformity of the flow. It was noted in Walker (1996) that due to the contraction, a velocity excess near the floor of the test section exists.

Figure 3.6 examines the behavior of the velocity profile at two speeds, and three different stream wise locations in the test section, namely $x = 0$ cm, 15 cm, and 30

cm. The edge of the step is located at $(x, z) = (0, 0)$ with the floor of the test section at $z = -50.2$ cm. The span wise position of the probe is at the half-width of the tank.

Next, the velocity profiles were measured at one downstream location but at seven other frequency settings on the drive motor. The goal of these profiles is to provide a calibration between the frequency counter and the free-stream velocity. Figure 3.7 shows the profiles measured in the middle of the channel for nine total speeds at a stream wise position of $x = 0$ cm.

By examining figure 3.7 the previously mentioned velocity excess is visible over the bottom half of the profile. To determine a velocity value to represent the free-stream, the profiles for each frequency are averaged vertically using a trapezoidal rule. Then the averaged velocities are fit using a linear regression yielding the following relation,

$$U(\mathrm{m/s}) = 0.0455\mathrm{Fq} - 0.0258 \tag{3.5}$$

The linear fit in equation 3.5 and the averaged velocities are shown in figure (3.8). The linear regression has a correlation coefficient $r = 0.9998$. Additionally, now the regression for the velocity can be used to evaluate the free-surface drop as a function of flow speed. The Bernoulli equation yields a difference in elevation between the highest and lowest points on the free-surface streamline as $15/32gu^2 \approx 0.47/gu^2$. The coefficient of the quadratic term from the regressions is approximately $0.26/g$, which is in accordance with the Bernoulli estimate of about half of the total difference, furthering the confidence in our procedure.

Finally, the cross-tank velocity uniformity of the test-section was assessed with a pitot tube at three speeds, seven span wise locations (20 cm - 80 cm, spaced 10 cm apart), and at the mid-tank depth of 25 cm. The root mean squares of the measurements at the three speeds was less than 0.28%.

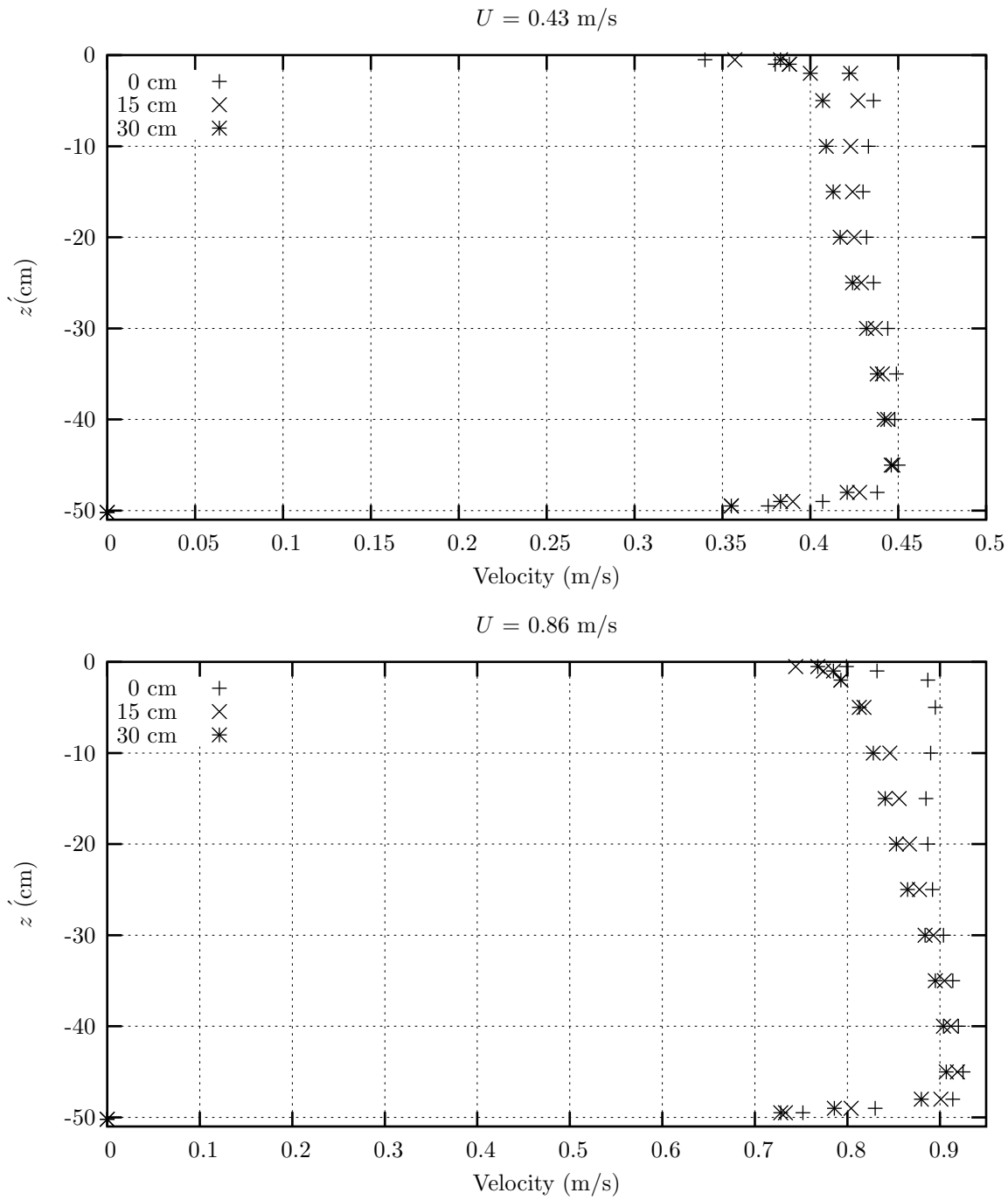

Figure 3.6: Stream wise-velocity profiles measured with a pitot tube in the center of the channel at locations $x = 0$ cm, 15 cm, and 30 cm. Top figure, $U = 0.43$ m/s; bottom figure, $U = 0.86$ m/s;.

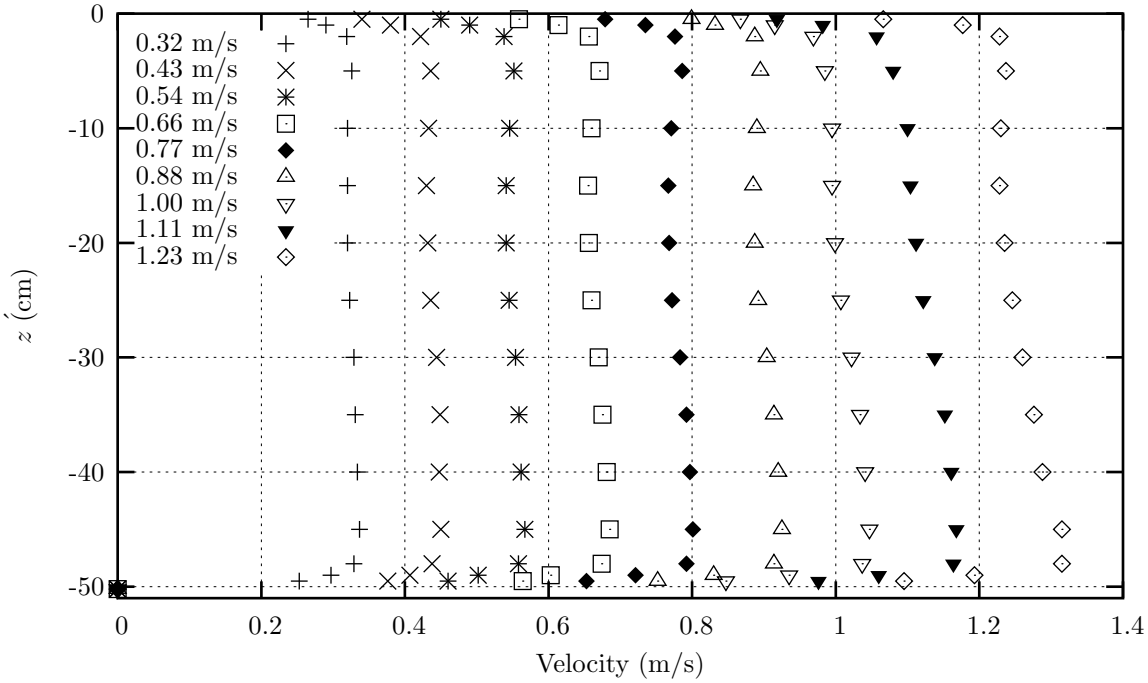

Figure 3.7: Stream wise-velocity profiles measured with a pitot tube in the center of the channel at nine different speeds. The probe is located at a stream wise coordinate of $x = 0$ directly beneath the body.

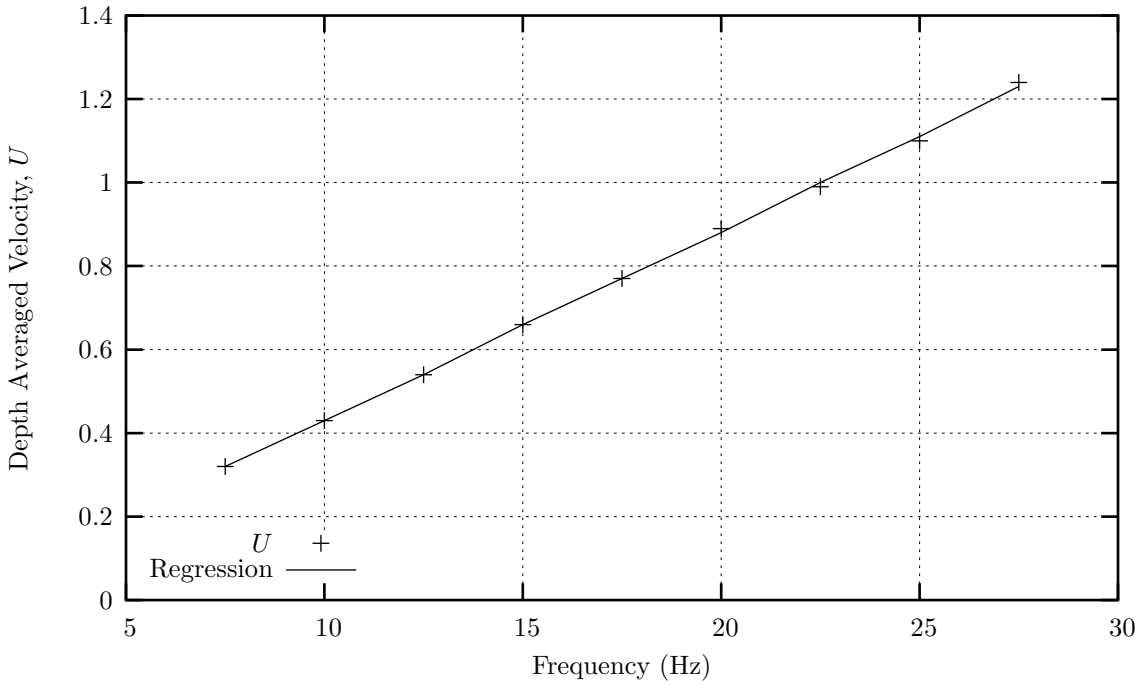

Figure 3.8: Regression of the depth-averaged stream wise-velocity versus the frequency counter on the drive motor.

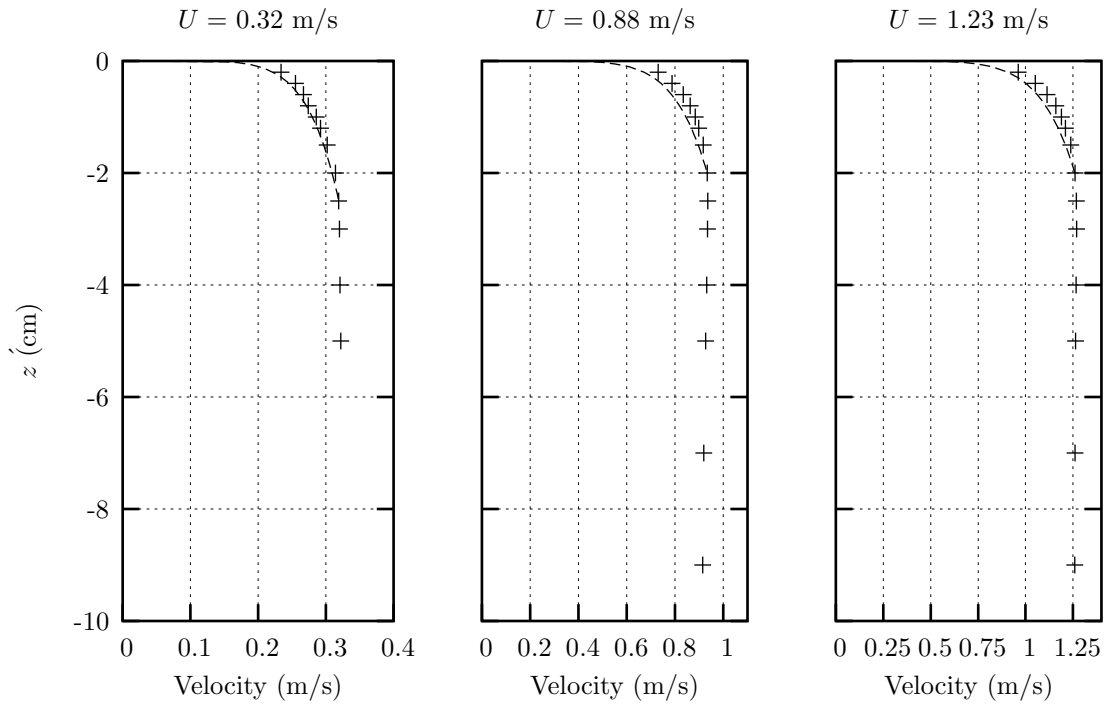

Figure 3.9: Boundary layer profiles at three speeds of $U = 0.32$, 0.88, and 1.23 m/s at a stream wise location of $x = -1$ cm. The green dashed line is the $1/7^{th}$ power law for turbulent wall flow.

3.2.3 Body Boundary Layer Profiles

A 3 mm head pitot tube was used to measure the boundary layer profiles on the body before the edge of the step. The tip of the pitot tube was positioned 1 cm forward of the trailing edge, and the pressure difference measured with the pressure measurement system as described in section (3.3.2).

The velocity measurements were made at three speeds spanning the operating range of the present experiments, namely, $U = 0.32$, 0.88, and 1.23 m/s. Figure 3.9 presents the measurements along with a representative $1/7^{th}$ power-law profile commonly associated with turbulent wall bounded flow (green dashed line).

3.3 Measurement Techniques

The present experiments investigate the instantaneous free-surface elevation behind the step, and the time-averaged velocity profiles in the wake of the body. To measure the free-surface elevation, a non-intrusive optical technique was used, as well as wire-capacitance and sonic probes. To measure the mean velocity profiles, a special pitot tube apparatus was constructed. This section will provide the details of the measurement tools implemented in the present experiments.

3.3.1 Free Surface Imaging Technique

To measure the surface elevation a non-intrusive laser-induced fluorescence system (LIF) is used similar to Walker, Lyzenga, Ericson, and Lund (1996). The water in the channel is dyed with Fluorescein disodium salt, and illuminated with a laser-light sheet from above. A filter was placed in front of the camera lens to block the laser light, allowing the CCD to capture the fluorescent light.

Equipment

The laser used in this set-up is a COHERENT Innova 70c Argon-ion 6W laser. The beam waist is approximately 0.5 mm and was focused into a sheet with a cylindrical lens. A series of mirrors passed the beam from the laser to above the model, and to a final stage of optics which were mounted on the transverse. The orientation of the sheet was stream-wise and can be seen in figure 3.10.

The camera used is a SONY XC-HR50 with a 495 x 640 pixel array. A personal computer using a Matrox Meteor II frame grabber, captured images at a rate of 60 Hz. The camera was affixed to the traverse as well, which allows the camera and optics to be moved in unison downstream. Depending on flow speed in the channel, the camera was positioned either to view the incidence plane of the laser at 12 degrees

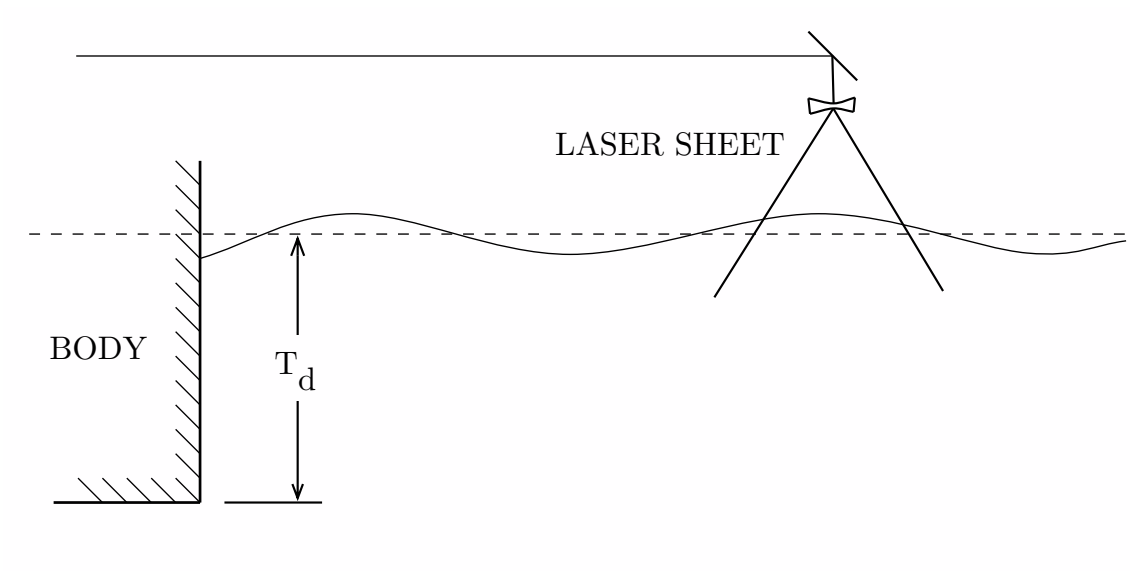

Figure 3.10: Schematic of laser-sheet.

relative to the calm-water plane, or at a 45 degree angle. The setting at a 45 degree angle was chosen to minimize the effects of a highly 3-dimensional free-surface which could obscure the laser sheet from the camera.

Data Analysis

The individual images were used to determine the free-surface elevation. The first step in the analysis is to convert the image file to a data array representing the pixel intensities. Then, in a column by column manner, the location of the free-surface was determined. The technique used finds the first pixel which exceeds a predefined threshold starting from the top (dark) portion of a specific column.

The threshold value used varies from the center of the image to the edges due to the quality of the laser sheet. Specifically, the threshold in the first and last column is set to 25% of the maximum intensity of 256. Then using a second order polynomial, the threshold reaches its maximum at the middle of the image, corresponding to column 320, of half the maximum intensity of 128, and then decreases symmetrically

to the 25% value for the last column.

After the elevation has been determined within the image, it must be mapped to the physical location in the coordinates of the body. When the camera is set at 12 degrees to the horizontal, a simple pixel/cm gain is applied in each the vertical and horizontal directions. An image of a calibration grid with 0.2 cm spacing is used in the image plane to determine the individual gains.

When the camera is set at the 45 degree viewing angle, the perspective on the image plane demands a more precise calibration. Using an image of the calibration grid, a multiple linear regression is performed to properly map the pixel location to physical space. This regression uses thirty-one points resulting in a root mean square error of 0.13 cm in the horizontal and 0.08 cm in the vertical directions respectively.

Finally the collection of instantaneous elevations represent a time series and are used to compute statistics of the mean and variance, as well as frequency spectrum information.

3.3.2 Pitot Tube Apparatus

In this experiment, flow velocities ranged from 0 - 1.3 m/s. In water these speeds result in dynamic pressures less than 5 cm of water. Ideally to measure these small pressure differences, a wet transducer is used. For these experiments, a wet-transducer was not available, so a technique following Preston (1972) was applied.

The resulting low pressures from small velocities in water are difficult to measure for several reasons. The accuracy of the measurement can be grossly affected due to the surface-tension forces on the air-water interface in the system. Also, when using a manometer to measure the pressure difference, the small head results in large time scales to reach equilibrium. For example, the pitot tube used in this experiment with

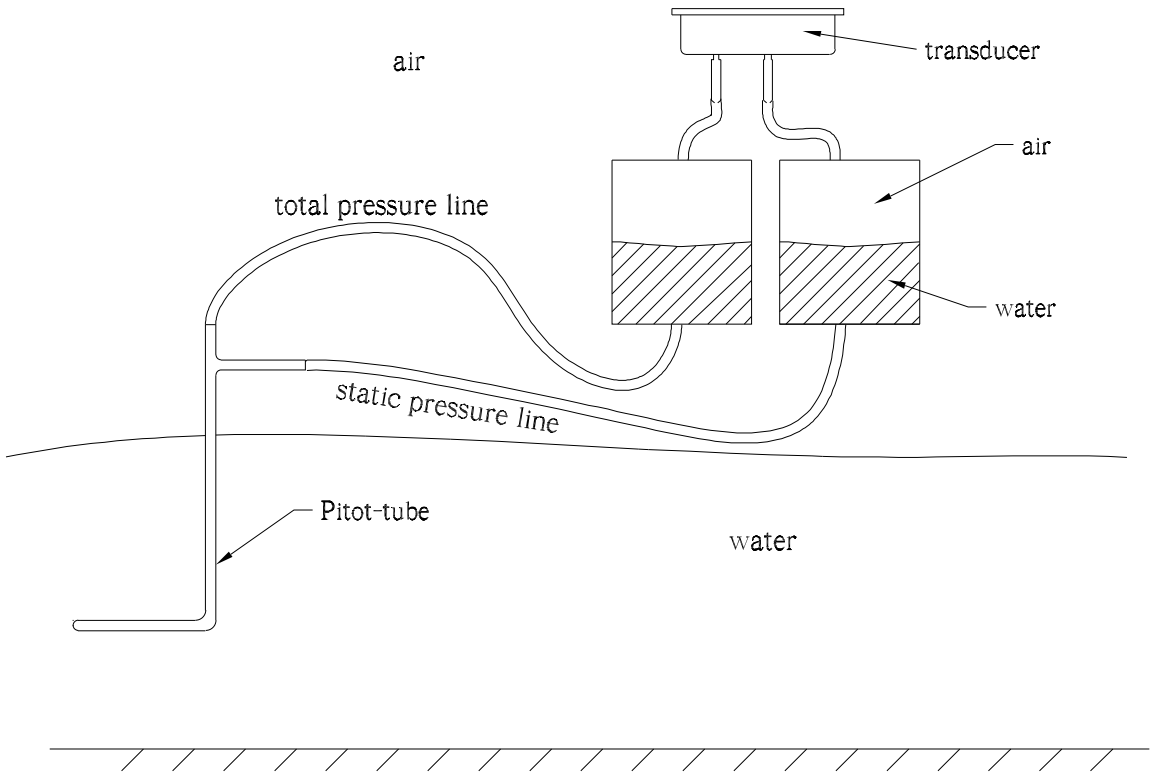

Figure 3.11: Schematic of Pitot-tube connected to twin reservoirs and pressure transducer.

a 1 mm diameter opening required waiting over one hour for the water level to reach equilibrium. Additionally, small temperature changes can also effect the pressure measurements.

The technique uses a dry diaphragm-type transducer and a reservoir to isolate the free-surface in the system. A schematic of the apparatus is shown in figure 3.11. The transducer, a SenSym SCXL004DN, reduces the long wait times associated with a manometer. This transducer is suitable for measuring gaseous media and was calibrated over a range of 8 cm of water.

The reservoir system consists of two canisters with an inside diameter of 5.08 cm. The pitot tube was connected to the bottom of these canisters, with the pressure transducer connected to the top. The system therefore has water from the pitot tube head until the canister, where in the large diameter reservoir the surface tension forces

are minimized. This results in a small volume of air subject to temperature change is in contact with the transducer. The system has a response time of approximately thirty seconds; this is determined from inspection of a time series in which the probe changes location in the flow measuring a different velocity.

For the experiments, the apparatus was affixed to the outside of the channel near the calm water level, and the pitot tube was attached to the traverse to allow precise movements in all three directions.

3.3.3 Capacitance and Sonic Wave Probes

In addition to the optical elevation measurement techniques, a wire-capacitance and sonic wave probe were used in the low and high speed tests. The drawback to the capacitance probe is its *intrusiveness* and its accuracy in a current. For the low speed tests, this instrument was used to make free-surface measurements behind the body. This probe consists of a 1 mm diameter glass tube encapsulating a copper wire.

In the high-speed tests, a sonic probe was used to measure the steady free-surface behind the model. The specific probe used is the Pulsonic Ultra 21. This sensor uses a sonic cone or 14 degrees and has a working distance range of 13-75 cm.

3.4 Summary

In this chapter, the properties and a description of the experimental facility has been presented. The method of determining the length scale for the BFSFS has been described using the cross-sectional area averaged stream-wise velocity, and the dynamic change to the reference free-surface height measured with the static port of a pitot tube. Finally the details of each experimental technique used have been described. Chapter 5 will contain the results and discussion of the BFSFS experi-

ments as compared to numerical simulation and the destroyer model experiments of chapter 2.

CHAPTER 4

NUMERICAL SIMULATIONS

The flow around a ship has received much attention in the past from numerical researchers. Methods to simulate a vessel moving through water can be divided into the categories of potential flow, Reynolds Averaged Navier Stokes (RANS), or a hybrid approach where a combination of the two are used together. The common objectives in computational simulation are the resistance of the vessel, the dynamic attitude of the body (i.e. sinkage and trim), and the wave field created by the ship. The presence of the transom stern introduces difficulties that are unique to each methodology. Potential flow methods must use contrived boundary conditions to attain a dry transom at full speed. Commonly the transom is assumed dry and a Kutta-condition is enforced on the trailing edge of the body, thus disabling the possibility to accurately predict resistance in the partially ventilated low Froude number regime.

A RANS formulation has difficulties due to the conflict between constructing a sufficiently refined grid and the time to conduct the simulation. A popular technique to simulate free-surface flows is to move the grid to adjust to the free-surface profile. When a moving grid method is used, breaking waves that naturally occur in the stern region must be avoided with damping techniques. Also, the surface of the transom

which is wet at zero speed becomes dry at full speed and necessitates the removal of computational cells on the body.

Another class of the RANS approach uses fixed grids and interface tracking or capturing methods to handle the free-surface. The two difficulties of breaking waves and reconstructing the grid which plague the moving mesh method are therefore eliminated. When simulating the flow around an entire ship, the performance of the computations in the transom region are rarely reported due to the lack of an experimental database with which to compare, or the low priority of predicting the flow in the transom region.

Recently, qualitative results using an unsteady RANS method that utilizes overlapping grids have been reported in Wilson and Stern (2005) for flow in the transom region. They discuss a periodic vortex shedding from the transom corner at a speed before full ventilation. The vortex shedding that they witness will be discussed both numerically and experimentally in this thesis.

To facilitate a study focused on the flow in the transom region, a two-dimensional unsteady Navier-Stokes solver is used to simulate the flow over a backward-facing step with a free-surface (BFSFS). The original version code authored by Alessandro Iafrati (Iafrati, Mascio, and Campana 2001) uses the Level Set method for interface capturing and the Spalart-Allmaras turbulence model is implemented to handle the turbulent nature of this flow.

In this chapter, an overview of the method will be presented, the boundary and the initial conditions will be described. The results from the simulations are presented in comparison to the experiments in chapter 5.

4.1 Governing Equations

The present method employed solves the Navier Stokes equations along with the incompressible form of the equation for the conservation of mass in a curvilinear coordinate system. The Cartesian form of the Reynolds averaged governing equations are,

$$\frac{\partial u_j}{\partial x_j} = 0 \tag{4.1}$$

$$\frac{\partial u_i}{\partial t} + \frac{\partial}{\partial x_j}\left(u_j u_i\right) = -\frac{1}{\rho}\frac{\partial p}{\partial x_i} + \frac{\partial}{\partial x_j}\left(\nu \frac{\partial u_i}{\partial x_j}\right) \tag{4.2}$$

In these equations, x_i and u_i are the Cartesian coordinates and averaged velocities respectively, p is the pressure, ρ is the fluid density, and the effective fluid kinematic viscosity is the sum of the molecular and eddy viscosities $\nu = \nu_m + \nu_t$.

In the practice of engineering, most problems exhibit complex geometries that are not well represented with Cartesian coordinates. To facilitate the simulation of realistic bodies, the governing equations are transformed from the Cartesian basis (x_i) to a curvilinear coordinate system (ξ_i) as seen in figure 4.1. The transformed momentum equations are,

$$\frac{\partial U_m}{\partial \xi_m} = 0 \tag{4.3}$$

$$\frac{\partial}{\partial t}\left(J^{-1}u_i\right) + \frac{\partial}{\partial \xi_m}\left(U_m u_i\right) = -\frac{1}{\rho}\frac{\partial}{\partial \xi_m}\left(J^{-1}\frac{\partial \xi_m}{\partial x_i}p\right) + \frac{\partial}{\partial \xi_m}\left(\nu G^{mn}\frac{\partial u_i}{\partial \xi_n}\right) \tag{4.4}$$

Here, volume flux normal to the ξ_m iso-surface is defined as

$$U_m = J^{-1}\frac{\partial \xi_m}{\partial x_j}u_j \tag{4.5}$$

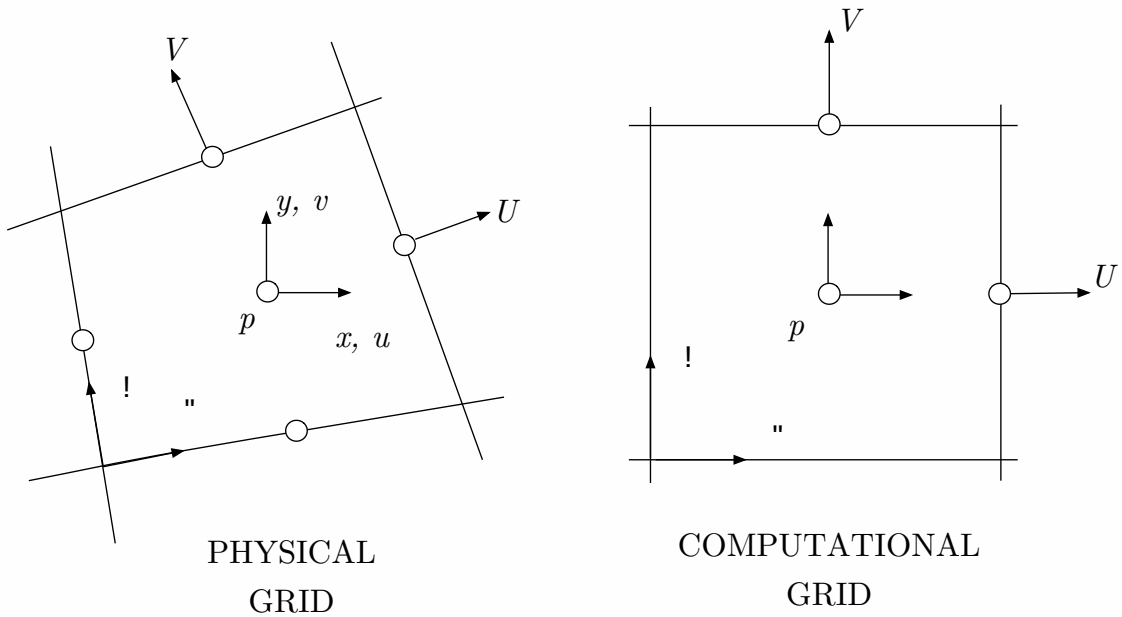

Figure 4.1: Physical and computational cells depicting the volume fluxes and non-staggered pressure and Cartesian velocity variables.

Other products of the transformation are the Jacobian J^{-1}, and mesh skewness tensor G^{mn} which are defined as,

$$J^{-1} = \det\left(\frac{\partial x_i}{\partial \xi_j}\right) \tag{4.6}$$

$$G^{mn} = J^{-1}\frac{\partial \xi_m}{\partial x_j}\frac{\partial \xi_n}{\partial x_j} \tag{4.7}$$

4.2 Flow Configuration

The model of a two-dimensional backward-facing step with a free-surface will be simulated numerically. A schematic of the computational domain is shown in figure 4.2. As defined in the previous chapter, the most important parameter that defines

a particular flow condition is the transom-draft Froude number, $F_T = U/\sqrt{gT_\mathrm{d}}$. The dimensions of the flow domain for all flow configurations are identical. The inlet velocity is uniform except for a turbulent body boundary layer on both the top and bottom of the body of thickness $\delta_{0.99}$.

For the simulations, the Froude number was altered by moving the bottom boundary of the body only. The uniform inlet velocity and the value of gravity were set to unity. The top and bottom of the domain use no-stress wall boundary conditions, and the outlet uses a convective outflow condition (section 4.6).

The length of the domain is chosen to span three wave-lengths behind the body. It is known from the experiments that the waves behind this particular body are significantly shorter than the associated linear wave-length ($\lambda_\mathrm{lin} = 2\pi U^2/g$), i.e. the actual wave-length can be 65% of the linear length. A numerical beach is used over the last wave-length to help minimize reflection of the finite length domain.

The vertical dimensions of the domain span from one half wave-length below the free surface to one-quarter the wave-length above. The lower dimension should be sufficient to minimize the effect of the boundary on the evolution of the free-surface. The definition of the solution domain is consistent with deep-water wave theory which states that the velocity induced by deep-water waves is one percent of the speed of the wave at a depth of one-half the wave-length. The upper location has been developed through experience running this type of simulation.

4.3 Discretization

To solve the governing equations numerically, they are integrated in time using a semi-implicit fractional step approach. The convective term and off-diagonal viscous terms are advanced explicitly with a third order Runge Kutta (Le and Moin 1991)

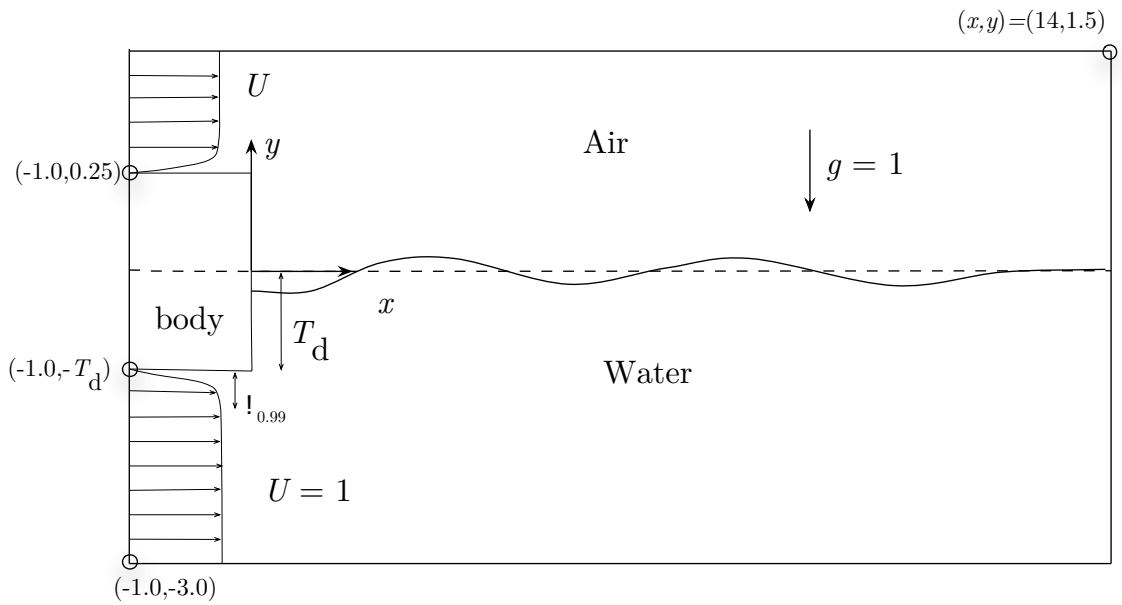

Figure 4.2: Backward-facing step with free-surface flow configuration. The dimensions of the domain appear as Cartesian coordinate pairs (x, y).

type method. The diagonal viscous terms are advanced with the unconditionally stable second order Crank-Nicholson scheme, which removes the restrictive viscous stability limit. The continuity equation is satisfied by solving a pressure Poisson equation for a pressure-like variable which enables the second half of the fractional step method to be completed. The discretized equations can be written as follows,

$$\frac{\partial U_m}{\partial \xi_m} = 0 \tag{4.8}$$

$$J^{-1}\frac{u_i^{n+1} - u_i^n}{\delta t} = C_i^n + D_E\left(u_i^n\right) + R_i\left(p^{n+1}\right) + \frac{1}{2}\left(D_I\left(u_i^{n+1} + u_i^n\right)\right) \tag{4.9}$$

In these equations, the convective, gradient, off-diagonal and diagonal diffusive operators are defined as follow,

$$C_i = -\frac{\delta}{\delta \xi_m}\left(U_m u_i\right) \tag{4.10}$$

$$R_i = -\frac{\delta}{\delta \xi_m}\left(J^{-1}\frac{\delta \xi_m}{\delta x_i}\right) \tag{4.11}$$

$$D_I = \frac{\delta}{\delta \xi_m}\left(\nu G^{mn}\frac{\delta}{\delta \xi_n}\right), \qquad m = n \tag{4.12}$$

$$D_E = \frac{\delta}{\delta \xi_m}\left(\nu G^{mn}\frac{\delta}{\delta \xi_n}\right), \qquad m \neq n \tag{4.13}$$

The Cartesian velocities and pressure are stored at the cell centers and the volume fluxes at the midpoint of the cell faces (Figure 4.1).

The viscous operator is separated into the diagonal and off-diagonal parts to simplify the structure of the left-hand-side of the momentum equation. In orthogonal grids, the off-diagonal matrix will be zero, and when a curvilinear grid is employed, the off-diagonal elements will remain small except in the cases of highly skewed meshes, which should always be avoided. To determine the volume fluxes, the Cartesian velocities are interpolated onto the cell faces using a κ-scheme (van Leer 1977).

The first step in the fractional step method predicts an intermediate velocity u^* using the convective and diffusive contributions,

$$\left(I - \frac{\Delta t}{2J^{-1}}D_I\right)\left(u^* - u_i^n\right) = \frac{\Delta t}{J^{-1}}\left[C_i^n + D_E\left(u_i^n\right) + D_I\left(u_i^n\right)\right] \tag{4.14}$$

Then, the corrector step updates the intermediate velocity such that the velocity at the new time step is divergenceless,

$$\left(I - \frac{\Delta t}{2J^{-1}}D_I\right)\left(u_i^{n+1} - u_i^*\right) = \frac{\Delta t}{\rho J^{-1}}\left[R_i\left(p^{n+1}\right)\right] \tag{4.15}$$

The left-hand-side of (4.14) is modified to ease the matrix inversion with the approximate factorization technique as follows,

$$\left(I - \frac{\Delta t}{2J^{-1}}\left(D_1 + D_2\right)\right)\left(u_i^* - u_i^n\right) \cong \left(I - \frac{\Delta t}{J^{-1}}D_1\right)\left(I - \frac{\Delta t}{J^{-1}}D_2\right)\left(u_i^* - u_i^n\right) + O\left(\Delta t^3\right) \tag{4.16}$$

Where

$$D_k = \frac{\delta}{\delta \xi_k}\left(\nu G^{kk}\frac{\delta}{\delta \xi_k}\right) \tag{4.17}$$

for $k = 1, 2$ and there is no summation over k. This factorization involves the inversion of two diagonal matrices for the predictor step, and yields the intermediate velocities at the cell centers. For the corrector step, the pressure must be determined such that the resulting velocity at the new time level is divergenceless. Using interpolation, the intermediate velocities are projected onto the cell faces enabling the calculation of the intermediate volume fluxes. Then using (4.15) with the definition of volume flux (4.8) the resulting equation is,

$$U_m^{n+1} = U_m^* - \Delta t\left(G^{mn}\frac{\delta \phi^{n+1}}{\delta \xi_n}\right) \tag{4.18}$$

Here, the pressure-like variable ϕ is related to the pressure with the following relation,

$$R_i\left(p^{n+1}\right) = \left(J^{-1} - \frac{\Delta t}{2}D_I\right)\left(\frac{R_i\left(\phi^{n+1}\right)}{J^{-1}}\right) \tag{4.19}$$

Note that it is shown in Rosendfeld, Kwak, and Vinokur (1991) that $p^{n+1} = \phi^{n+1} + O\left(\Delta t^2\right)$. Now with the equation for the volume flux at the new time step (4.19) and the equation for the continuity of mass (4.1), the following pressure Poisson equation for pressure is reached,

$$\frac{\delta}{\delta \xi_m}\left(G^{mn}\frac{\delta \phi^{n+1}}{\delta \xi_m}\right) = \frac{1}{\Delta t}\frac{\delta U_m^*}{\delta \xi_m} \tag{4.20}$$

This elliptic Poisson equation (4.20) is solved using a multigrid method to satisfy continuity exactly (machine zero).

For clarity, the previous derivation has neglected the details of the Runge-Kutta treatment of the convective and off-diagonal diffusive terms. The three-step low-storage method of Le and Moin (1991) is third order accurate but requires only two storage locations per variable per full time-step. The stability of this method has a CFL limit of $\sqrt{3}$, where the local CFL number is computed as,

$$CFL = \left(\frac{|u|}{\Delta x} + \frac{|v|}{\Delta y}\right)\Delta t = (|U| + |V|)\,\frac{\Delta t}{J^{-1}} \tag{4.21}$$

4.4 Free-Surface Treatment

To incorporate two fluids a distance function is defined as the signed minimum distance to the air-water interface as follows,

$$\begin{aligned} d &> 0 && \text{in water} \\ d &< 0 && \text{in air} \\ d &= 0 && \text{on the interface} \end{aligned}$$

The distance function represents a scalar field describing the free-surface (which is the zero-level-set) and obeys the generic advection equation,

$$d_t = -\overrightarrow{u} \cdot \nabla d \tag{4.22}$$

Due to the complexity of the flow field, the advection equation does not preserve the distance property of the distance function. This necessitates the operation of *re-distancing*. There are several methods to re-distance including a direct re-distance method employed here, and a partial-differential-equation method which involves solving the Eikonal equation ((Sussman, Smereka, and Osher 1994), (Sussman and Fatemi 1999), (Sussman and Puckett 2000)). While the Eikonal equation approach is more complicated, it requires less computational effort (the direct re-distance method is especially expensive in three dimensions). The direct method has better mass conservation properties and is used exclusively for the results reported herein.

Another consideration regarding the re-distancing is to determine how often the procedure should occur. Re-distancing is only needed when the distance variable strays from its original definition, and then again only near the interface is the definition important. In all simulations here, the re-distancing was completed at each full time-step. In the total computational budget, the iterative solution of the pressure Poisson equation requires the most effort, and the potential time savings made by re-distancing less often is minimal.

The simulation of air and water presents large discontinuities in the fluid properties of viscosity and density at the interface. To eliminate stability difficulties in the calculation of the derivatives in the governing equations, the interface is smeared over several cells as shown in equation 4.23.

$$f(d) = \begin{cases} f_w & \text{if} \quad d > \delta \\ f_a & \text{if} \quad d > \delta \\ (f_w + f_a)/2 + (f_w - f_a)/2\sin(\pi \mathrm{d}/(2\mathrm{d})) & \text{otherwise} \end{cases} \tag{4.23}$$

where δ is the half distance of region in which the jump is spread.

For the simulations herein, the grid is locally refined in regions of breaking near the transom, and gradually coarsened in the downstream direction. The interface thickness is chosen so that it covers multiple cells in the fine region, and near the downstream end of the domain covers less then a complete cell in the x direction. Due to the beach, the free surface in the region of large cells near the downstream end of the domain is parallel to the y faces of the cells. This allows the interface thickness to violate the restriction of being smeared over at least several cells in each direction.

4.5 Spalart-Allmaras Turbulence Model

4.5.1 Transport Equation

The process of Reynold's Averaging the Navier-Stokes equations introduces six new unknowns (in three dimensions) referred to as the Reynold's stresses ($\overline{u_i' u_j'}$). Using the Boussinesq approximation, the Reynold's Stresses are related to the fluid velocities as

$$-\frac{\partial \overline{u_i' u_j'}}{\partial x_j} = \nu_t \frac{\partial^2 u_i}{\partial x_j \partial x_j} \tag{4.24}$$

The six unknowns have been reduced to the single unknown of the eddy-viscosity (ν_t), which is not a physical fluid property but a position-dependent function of the local flow. The Spalart-Allmaras model (Spalart and Allmaras 1994) uses a single transport equation for the evolution of the eddy viscosity. The formulation is as follows:

$$\nu_t = \tilde{\nu} f_{v1} \tag{4.25}$$

$$\frac{\partial \tilde{\nu}}{\partial t} + u_j \frac{\partial \tilde{\nu}}{\partial x_j} = c_{b1}\tilde{S}\tilde{\nu} - c_{w1} f_w \left(\frac{\tilde{\nu}}{d}\right)^2 + \frac{1}{\sigma}\frac{\partial}{\partial x_k}\left[(\nu + \tilde{\nu})\frac{\partial \tilde{\nu}}{\partial x_k}\right] + \frac{c_{b2}}{\sigma}\frac{\partial \tilde{\nu}}{\partial x_k}\frac{\partial \tilde{\nu}}{\partial x_k} \quad (4.26)$$

$$c_{b1} = 0.1355, \quad c_{b2} = 0.622, \quad c_{v1} = 7.1 \quad \sigma = \frac{2}{3} \quad (4.27)$$

$$c_{w1} = \frac{c_{b1}}{\kappa^2} + \frac{(1 + c_{b2})}{\sigma}, \quad c_{w2} = 0.3, \quad c_{w3} = 2, \quad \kappa = 0.41 \quad (4.28)$$

$$f_{v1} = \frac{\chi^3}{\chi^3 + c_{v1}^3}, \quad f_{v2} = 1 - \frac{\chi}{(1 + \chi f_{v1})}, \quad f_w = g\left[\frac{1 + c_{w3}^6}{g^6 + c_{w3}^6}\right]^{1/6} \quad (4.29)$$

$$\chi = \frac{\tilde{\nu}}{\nu}, \quad g = r + c_{w2}(r^6 - r), \quad r = \frac{\tilde{\nu}}{\tilde{S}\kappa^2 d^2} \quad (4.30)$$

$$\tilde{S} = S + \frac{\tilde{\nu}}{\kappa^2 d^2} f_{v2}, \quad S = \sqrt{2\Omega_{ij}\Omega_{ij}}; \quad \Omega_{ij} = \frac{1}{2}\left(\frac{\partial u_i}{\partial x_j} - \frac{\partial u_j}{\partial x_i}\right) \quad (4.31)$$

where d is the distance to the closest surface. The transport equation 4.26 is discretized in the same manner as the momentum equations.

4.5.2 Validation and Accuracy

The model problem of a turbulent wake is simulated to verify the implementation of the turbulence model and to assess the spatial accuracy of the computational method. The computational domain ($L_x \times L_y = 5.0 \times 0.5$) uses the experimental exponential equation (4.32) of Wygnanski, Champagne, and Marasli (1986) for the inflow boundary condition. Equation (4.32) relates the non-dimensional defect velocity ($f(\eta) = (U - u)/(U - u_{\min})$) and the non-dimensional span-wise coordinate ($\eta = y/l$), where l is the y location corresponding to half the defect velocity and $u_{\min}$ is the u value at the location of maximum defect velocity. It is noted that Wygnanski

et al. (1986) find that the traditional analytic exponential function representing the turbulent wake, $f(\eta) = \exp\left[-0.693\eta^2\right]$, overestimates the velocity on the outer edges of the wake.

$$f(\eta) = \exp\left[-0.637\eta^2 - 0.056\eta^4\right] \tag{4.32}$$

The solution is unsteady therefore a temporal average is used in the comparisons. The simulations run for a time equal to twenty-four flow-through periods of the domain, and the average is taken over the last twelve periods. The stream-wise location used to compare the velocity profiles is 180 l downstream the inflow boundary.

Three uniform grids are constructed (coarse - 128 x 64, medium - 180 x 90, and fine - 256 x 128) and the velocity profiles are compared using the L_1, L_2, and L_∞ norms (defined in equation 4.33).

$$L_p(A, B) = \left[\frac{1}{n}\sum_{1}^{n}|a_i - b_i|^p\right]^{\frac{1}{p}} \tag{4.33}$$

The discretization error (DE) is defined and written as a series expansion,

$$\mathrm{DE} = f_\mathrm{k} - f_\mathrm{exact} = g_p h_k^p + \mathrm{HOT} \tag{4.34}$$

where f_k is the numerical solution on grid k, g_p is a coefficient of the leading order error term, and p is the observed order of accuracy. If the discretization error is dominated by the first term, the solution is said to be in the asymptotic range, and higher-order terms (HOT) are assumed negligible.

By writing equation (4.34) for each of the three grids and introducing the grid refinement parameter $r = \Delta x_2/\Delta x_1 = \Delta x_3/\Delta x_2 = \sqrt{2}$, the observed order of accuracy can be determined by

Table 4.1: Observed order of accuracy for a turbulent wake.

Norm	L_1	L_2	L_∞
medium - coarse error	1.67e - 02	2.36e - 02	5.31e - 02
fine - medium error	7.80e - 03	1.09e - 02	2.55e - 02
Order p	2.20	2.23	2.12

$$p = \frac{\ln\left(\frac{f_3 - f_2}{f_2 - f_1}\right)}{\ln(r)} \tag{4.35}$$

The observed order of accuracy is reported with the corresponding errors in table 4.1. To calculate the norms, the data from the coarser grids are interpolated onto the fine grid using cubic splines. The theoretical (formal) discretization error is second order for each term in the governing equations and the observed order of accuracy exceeds this slightly in all three norms.

The convergence is seen graphically in figure 4.3 where the velocity profiles used in the order of accuracy calculations are plotted non-dimensionally with the exponential distribution, equation (4.32).

4.6 Initial and Boundary Conditions

4.6.1 Boundary Conditions

The inflow boundary condition uses a uniform velocity with a turbulent boundary layer profile along the top and bottom of the body.

$$\frac{u(y)}{U} = \left(\frac{y}{\delta_{0.99}}\right)^{\frac{1}{7}} \tag{4.36}$$

The boundary layer thickness was determined from the experiments presented in this thesis as a value of half the transom draft.

The outflow uses a convective boundary condition. This condition has been shown to be effective in time-accurate simulations to remove large flow structures from the

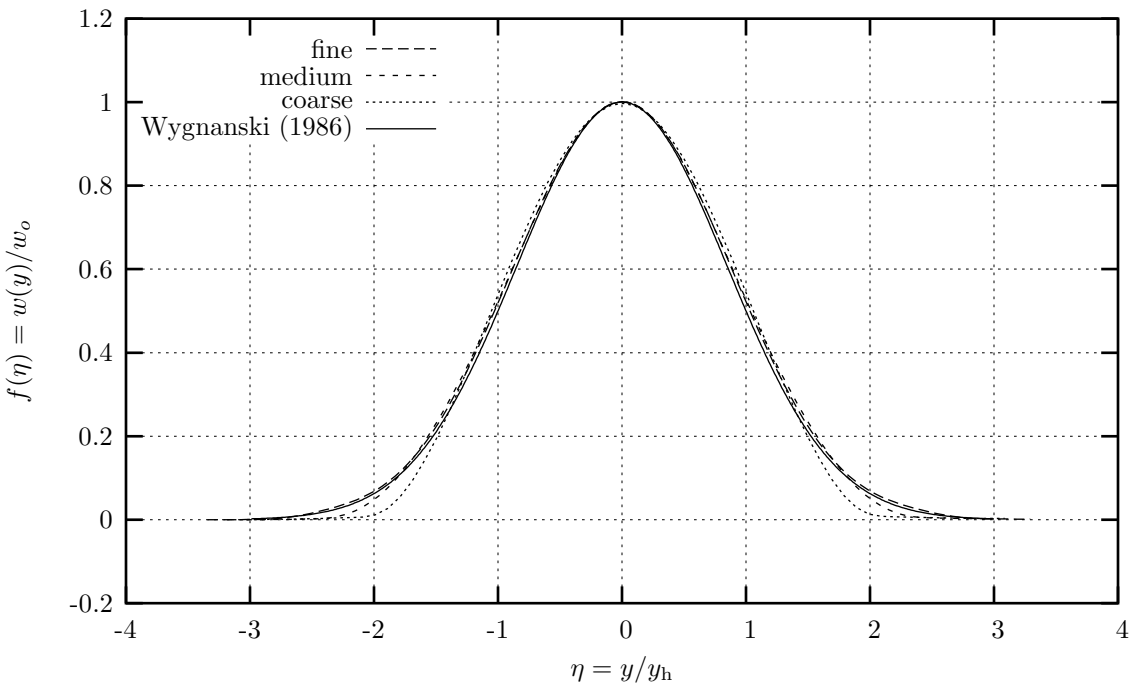

Figure 4.3: Horizontal velocity profile of the turbulent wake compared to exponential distribution from the experiments of Wygnanski, et al. (1986).

interior of the domain with minimal reflection. The condition found in Le and Moin (1994) uses the convective velocity, U_c, which is the average velocity at any vertical plane for a given stream-wise coordinate. The condition appears as follows,

$$\frac{\partial u_i}{\partial t} + U_c \frac{\partial u_i}{\partial x} = 0 \tag{4.37}$$

The no-stress walls on the top and bottom of the domain impose zero vertical velocity, and a mirrored stream-wise velocity in the ghost cells to effect a gradient equal to zero.

4.6.2 Initial Conditions

To initialize the flow domain, the inlet conditions are used for all x. In other words, directly behind the body there is no-flow, and above and below this region exists the regions of uniform flow with the velocity profile of the body boundary layer

forming the transitions. After the simulation begins, the two shear layers become unsteady and interact with each other which causes the flow to develop.

4.6.3 Body Boundary Condition

To incorporate a body in the domain, the body force approach was used. For any grid point inside the body boundary, an additional body force is added to the Navier-Stokes equations in the form,

$$q_i = -C_f u_i \tag{4.38}$$

where C_f is a coefficient representing the magnitude of the body force, and then u_i is the respective Cartesian velocity. This condition *effects* the body by stopping any fluid in a cell where the body force term is applied.

A drawback to this approach in the specific context of a surface piercing body is that the interface becomes *frozen* with the fluid inside the body. In the case when the contact line on the body is unsteady, the interface will stretch many cells vertically over a few cells horizontally. A properly selected interface thickness will allow the interface to exist in any orientation possible, but this effect puts unwanted material in cells near the body when the contact point strays far from the interface position inside the body.

A simple procedure was developed to eliminate any problems caused by the frozen interface. After each completion of the re-initialization process, the location of the interface along the body was determined. The y coordinate of this point was used as the signed amplitude of a half sine wave which represents the interface inside the body. This sine wave reconstructs the interface inside the body returning to a value of zero at the left boundary of the domain. This treatment effectively creates

a contact angle of 90 deg between the body and the interface.

After the reconstruction of the zero-level-set inside the body, each column of cells for $x < 0$ is re-distanced one-dimensionally in the vertical direction.

4.6.4 Numerical Beach

To aid in minimizing the reflection of outgoing waves on the finite domain, a beach is used. The numerical beach is implemented in the advection equation for the distance function as follows,

$$d_t = -\overrightarrow{u} \cdot \nabla d - \gamma(y + d) \tag{4.39}$$

where γ is a coefficient that is equal to zero in the interior of the domain, and at the start location of the beach grows to a given value at the end of the domain.

4.7 Grid Convergence

To evaluate the quality of the finest grid constructed, a convergence study was conducted for the most challenging (most unsteady) Froude number, $F_T = 2.5$. Three grids, 64 x 128, 96 x 192, and 128 x 256 where constructed. To compare the different meshes, the mean and r.m.s. of the free-surface are shown in figure 4.4. Additionally, the mean stream-wise velocity profiles are shown for two downstream locations of $x/\lambda_{\text{lin}} = 0.28$ and 0.70 corresponding to the x locations of the first wave crest and trough respectively. For each grid the compared quantity is averaged from $100 < t < 250$ seconds, with a sampling period of 0.25 seconds. Due to practical limitations of computing power, grids were limited to approximately 33,000 cells, which corresponds to a run time of four days on a 2 GHz Athlon processor machine to simulate 250 seconds.

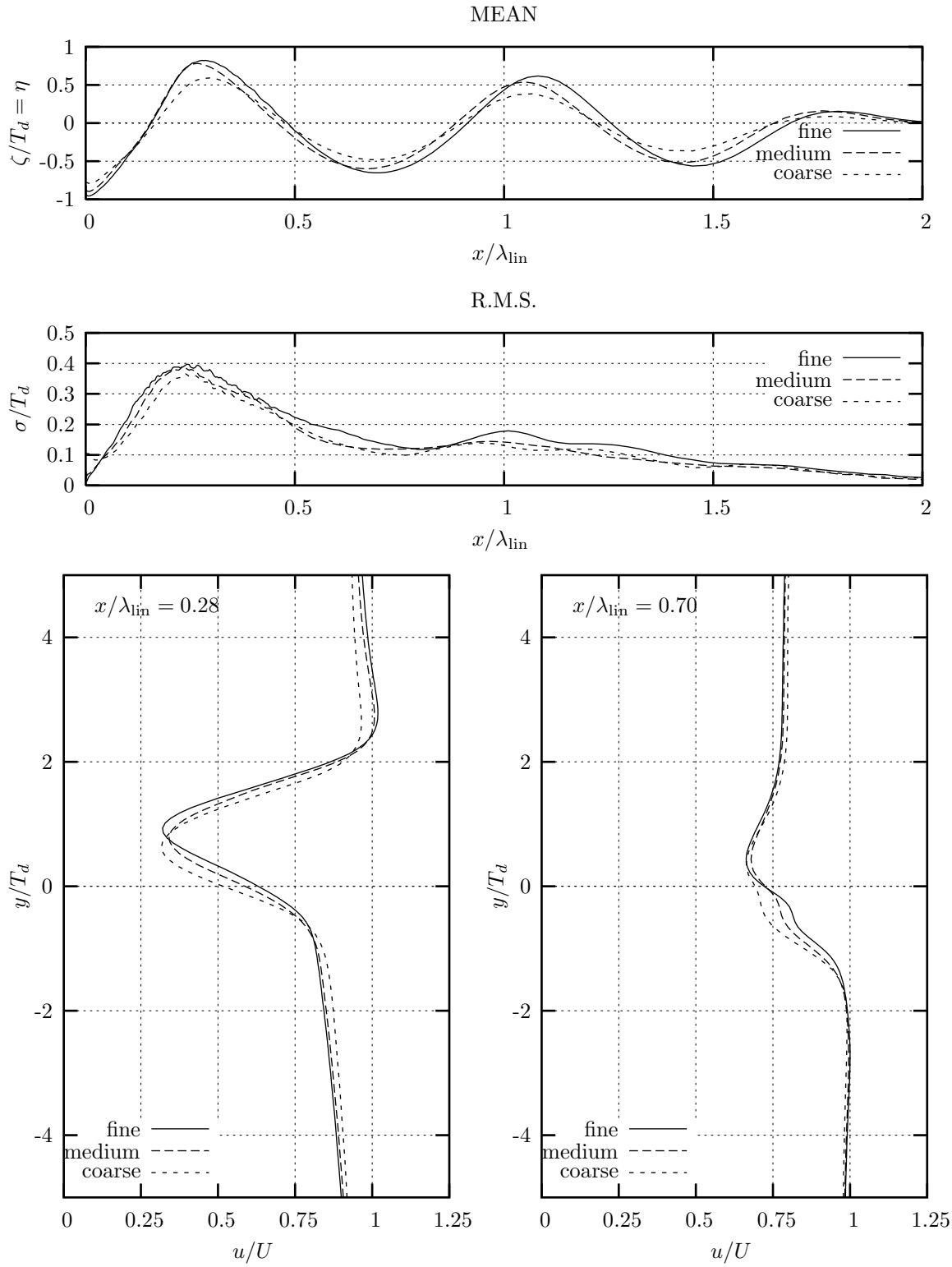

Figure 4.4: Comparison of the three different grids. The top two figures show the mean and r.m.s. of the free-surface. The bottom left shows the stream-wise velocity at a location $x/\lambda_{\text{lin}} = 0.28$ (first wave crest), the bottom right shows the stream-wise velocity at a location $x/\lambda_{\text{lin}} = 0.70$ (first wave trough).

Unfortunately, the formal order of accuracy analysis used for the turbulent wake in section 4.5.2 is limited to uniform mesh spacing, which is not the case in the grids for the BFSFS. Instead, the relative error in each of the three norms is reported in table 4.2 for the mean, r.m.s., and two velocity profiles seen in figure 4.4. The *average* grid refinement ratio (the total number of points in a coordinate direction) is 1.33 for the fine-medium grids, and 1.5 for the medium-coarse grids.

By examining table 4.2, the errors in all three norms decrease with grid refinement, with the exception of the r.m.s. The magnitude of the L_∞ errors for the mean and r.m.s. are approximately 20% and 5% of the transom draft respectively. An alternative length in which to normalize the error which is perhaps more appropriate considering conservation of mass, would be to use the length of the interface. Doing so decreases the errors by a factor of 90, driving even the most stringent assessor of error, the L_∞ norm, to less than 0.3%.

The L_∞ errors in the velocity profiles are near 8% the free-stream for both locations. By inspecting the velocity profiles in accordance with the mean free-surface, it is apparent that there is a shift of the velocities between different grids due to the different vertical locations of the free-surface on the respective grids. This amplifies the error values.

The same reasoning applies in explaining the divergence in the L_∞ error for the free-surface r.m.s. The location of the second wave crest in the fine grid is shifted downstream and consequently the r.m.s. profile is shifted, accounting for the larger L_∞ errors in the medium-fine grid comparison.

Therefore the fine grid is used for the simulations conducted in this thesis. The test cases are summarized in table 4.3.

Table 4.2: Relative errors for the backward facing step with free-surface.

	Mean			r.m.s.		
Norm	L_1	L_2	L_∞	L_1	L_2	L_∞
medium - coarse	7.81e - 2	9.75e - 2	25.5e - 2	1.06e - 2	1.49e - 2	8.00e - 2
fine - medium	7.19e - 2	9.15e - 2	20.1e - 2	1.79e - 2	2.24e - 2	4.80e -2
	$x/\lambda_{\text{lin}} = 0.28$			$x/\lambda_{\text{lin}} = 0.70$		
medium - coarse	1.45e - 2	2.13e - 2	8.02e - 2	1.25e - 2	1.77e - 2	7.71e - 2
fine - medium	0.97e - 2	1.42e - 2	5.76e - 2	0.82e - 2	1.11e - 2	4.89e - 2

Table 4.3: Simulation Test Case Parameters.

Case	Grid	F_T	Re_T	$\Delta y_{min}/T_{\text{d}}$	$\Delta x_{min}/T_{\text{d}}$
1	256×128	1.5	4e - 4	0.034	0.050
2	256×128	2.0	4e - 4	0.053	0.088
3	256×128	2.5	4e - 4	0.075	0.138
4	256×128	3.0	4e - 4	0.109	0.198
5	256×128	3.5	4e - 4	0.109	0.198
			Grid Convergence		
6	192×96	2.5	4e - 4	0.091	0.181
7	128×64	2.5	4e - 4	0.138	0.284

4.8 Summary

In this chapter the details of the numerical method and its implementation to simulate the BFSFS were discussed. The Level Set method was chosen for its capabilities to capture unsteady, highly non-linear breaking waves. The grid convergence study on a single-phase turbulent wake validates the Spalart-Allmaras turbulence model and shows that the discretization error is second-order. The grid convergence study on the BFSFS configuration reports errors of a tolerable magnitude using the mean and r.m.s. of the free-surface and the stream-wise velocity.

In chapter 5 the results for five simulated test cases ($F_T = 1.5$, 2.0, 2.5, 3.0, 3.5) will be presented in comparison to the experiments.

CHAPTER 5

RESULTS AND DISCUSSION

The focus of this chapter is to present the experimental results and numerical simulations of a backward facing step with a free-surface, the problem that was introduced and discussed in chapters 3 and 4. This canonical problem is posed as a model of a transom stern (chapter 2).

In section 5.1 the free-surface behavior is described by its mean and root mean square properties. Four flow regimes are introduced and used to categorize the free-surface profiles based on their unique characteristics as a function of Froude number.

In section 5.2 the present experiments and numerical results are compared to analytic inviscid theories. It is shown that the inviscid theories that lack vorticity fail to accurately predict the residual wave-length. A wake thickness model is introduced to estimate the vorticity and the stream-function theory of Dalrymple (1974) is used to predict the wave-length.

Section 5.4 a frequency domain analysis is used to describe the vortex shedding in the wake and the influence of the vortex street on the r.m.s. of the free-surface fluctuations.

In section 5.3 the process of transom un-wetting is documented and comparisons are made with the backward-facing step with a free-surface (BFSFS), the destroyer

model tests, and a regression equation as presented in Doctors (2003).

The experimental results in this chapter are organized into two series. The first contains the free-surface elevation measurements taken using LIF, wire-wave, and sonic probe techniques and describe the wave profiles behind the step. This series is broken into two sub-series, 1.1 and 1.2, which each represent a different model set-up with the zero-speed transom draft of 4.2 and 6.35 cm respectively. The results are used in sections 5.1, 5.2, and 5.4.

The second series is comprised of free-surface elevations taken with the LIF technique and pressure measurements near the body to explore the process of un-wetting. The results from this series numbered 2.1-2.5 are shown in section 5.3.

The complete set of results for the free-surface mean profile and r.m.s. can be found in appendix B.

5.1 Wave Profile General Behavior

The BFS two-dimensional canonical problem is posed as a model of a transom stern. To bridge the BFS to the full-scale ship application, nomenclature in the following discussion will reference both ship geometry, and geometry from the canonical problem simultaneously.

For a transom stern ship, as the vessel increases in speed from rest the free-surface location on the transom gradually drops and a viscous wake becomes evident by observation of unsteadiness on the free-surface. At an intermediate speed where the transom is partially wetted, the free surface becomes very irregular and unsteady. There are many scales of turbulence present at this stage, from small eddies to large vortices that are on the order of magnitude of the transom draft. Also in this regime there may be breaking waves and spray at model and full scales. Finally when the

vessel attains sufficient speed, the transom becomes dry, and the only unsteadiness evident in the free-surface is due to the turbulence shed from the body boundary layer or unsteadiness due to the motion of the body or incoming waves.

In accordance with this description, a particular flow condition (a specific Froude number) can be placed into one of four regimes based on the free-surface characteristics for a given Froude number. The first stage ranges from a Froude number of zero until the free-surface begins to exhibit significant unsteadiness. Figure 5.1 shows the maximum r.m.s. of free-surface elevation behind the body as a function of Froude number (the x location of the maximum r.m.s. varied slightly with Froude number). In this figure, there are data from three different measurement techniques and numerical simulations. The increase in unsteadiness is seen at a Froude number of approximately one. As will be shown later in the thesis, the average location of the free-surface on the body will be shown to deviate from its calm water position concurrently with the increase in free-surface fluctuation. Additionally the large over-prediction by the numerical simulations is attributed to surface tension effects as well as inaccuracies due to the turbulence modeling, more discussion on this topic is found in section 5.2.

The second regime extends in Froude number until the transom becomes ventilated at a speed defined as the critical Froude number (F_c). The speed of ventilation is highly sought and will be addressed specifically in section 5.3. The third stage contains a small speed range where the first wave crest behind the body is breaking. Upon the onset of ventilation, the layer of water on the transom manifests into a breaking roller residing on the front face of the first wave crest. As the speed increases, the location of the roller moves up the face of the wave, eventually being shed. The fourth and final regime contains all speeds after which the breaking toe

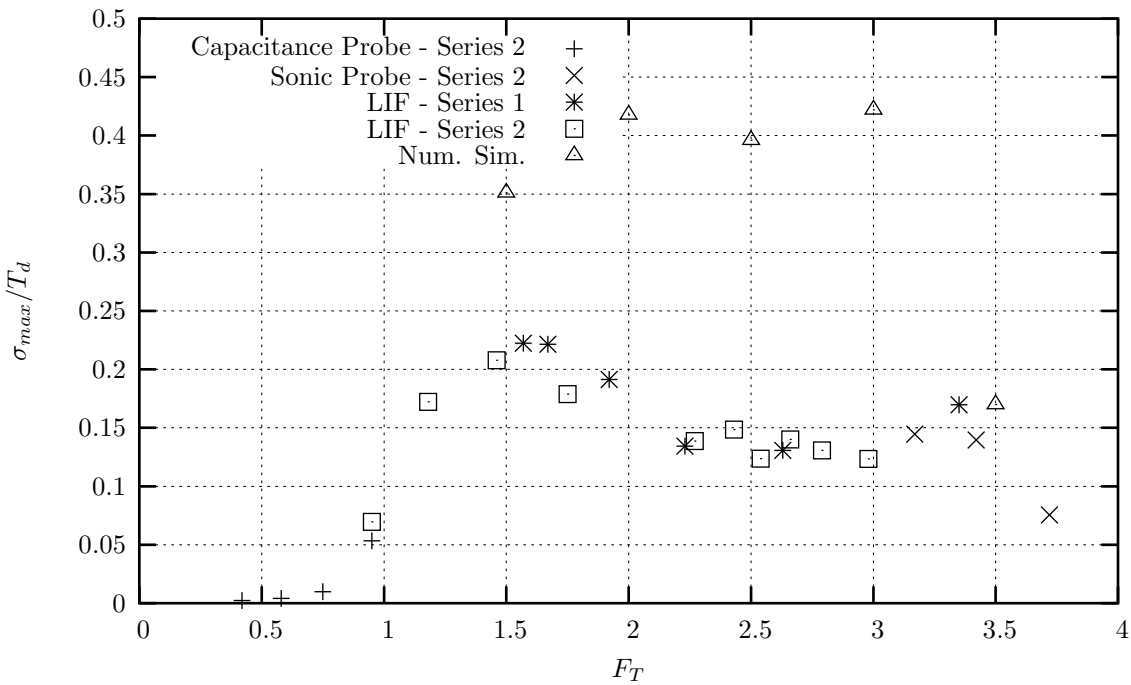

Figure 5.1: Maximum r.m.s. of the free-surface as determined from three different measurement techniques and numerical simulation. The transition from regimes 1 and 2 is marked by the increase of r.m.s. near $F_T \approx 1$.

is shed. Pictorially, the four regimes are depicted in figure 5.2. These diagrams can be compared to LIF images shown in figures 5.3-5.6. To capture these images, the camera was located outside the tank to view the experiment looking up at the free-surface.

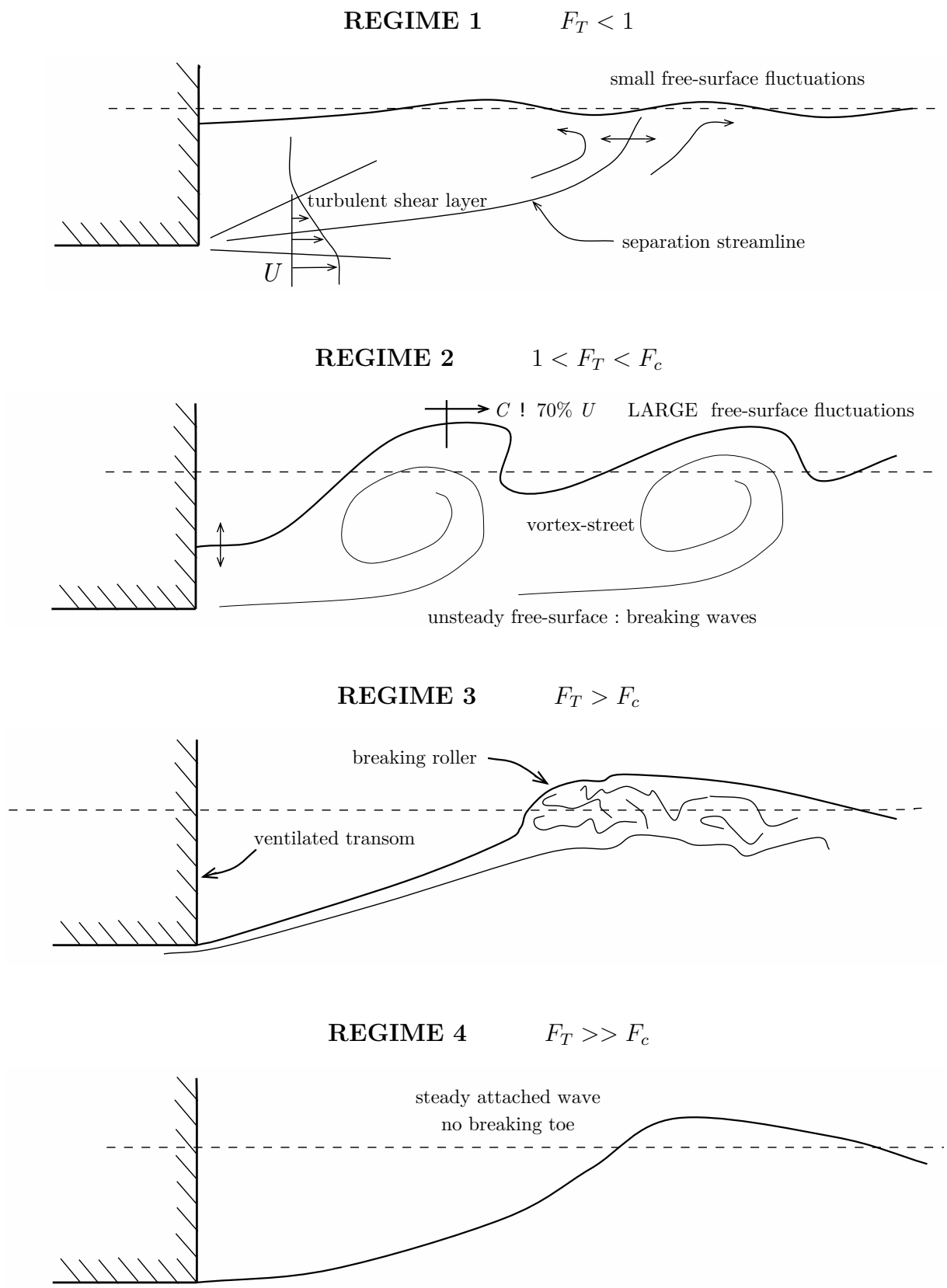

Figure 5.2: Diagrams of the four flow regimes for the backward facing step with free-surface.

Whenever a body moves in a fluid on or near a free surface, energy is exchanged between the body and the fluid. This energy is radiated from the body in the form of waves and it is also diffused by means of viscosity. For full-scale vessels, both mechanisms are important in accounting for the drag on the body.

In the first Froude number regime, the free surface exhibits a gentle depression behind the body. This is considered to be a result of entrainment due to the shear layer at the keel, which is relatively far from the free-surface. Figure 5.7 describes the free-surface as measured with the wire-capacitance probe and the LIF technique at a Froude number of 0.95.

It should be noted that there exists a significant bias in the mean free-surface location measured with the wire capacitance probe, as is seen in figure 5.7. which is due to the water current in which the probe is operating. Because the fluid velocity behind the body is that of a wake, the situation is complicated by the fact that the velocity in the wake increases as the probe is moved in the downstream direction. It would then seem that if the bias is proportional to the magnitude of the fluid velocity, then the free-surface profiles reported for the wire probe are perhaps only reflecting this effect of wire probe *self-disturbance*, i.e. in the near wake where the defect velocity is large, the bias would be small and then farther downstream where the defect velocity approaches zero the bias would approach a maximum. The comparison between the two methods shows that the bias error is approximately 0.5 cm. This provides confidence that the additional profiles measured with the wire probe at lower Froude numbers represent the free-surface, and not a wire-probe in a spatially varying current.

At a Froude number of approximately one, the unsteady shear layer begins to interact directly with the free-surface and the second Froude number regime is real-

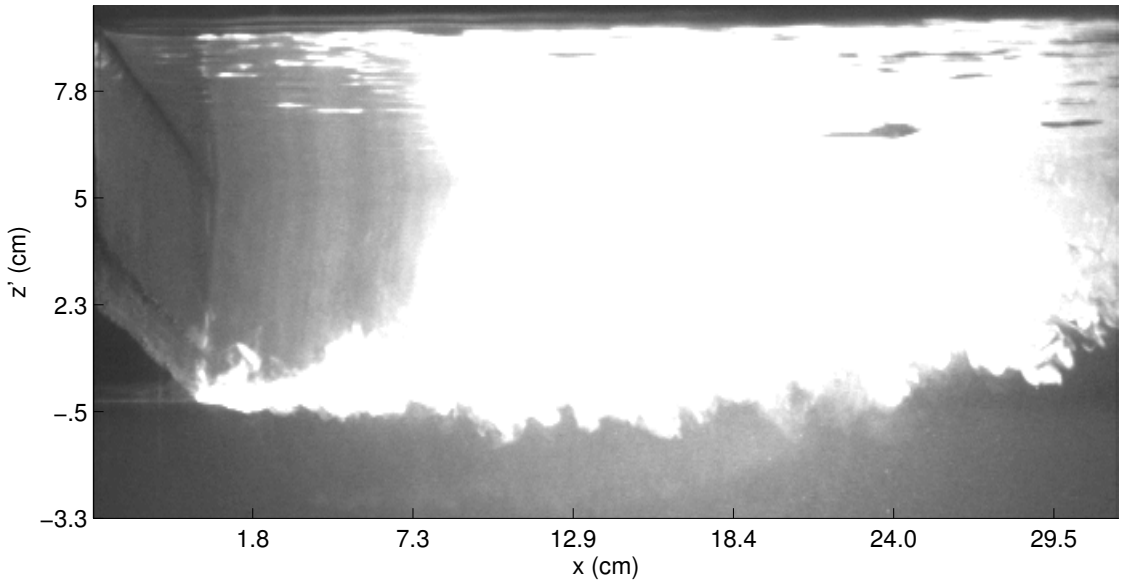

(a)

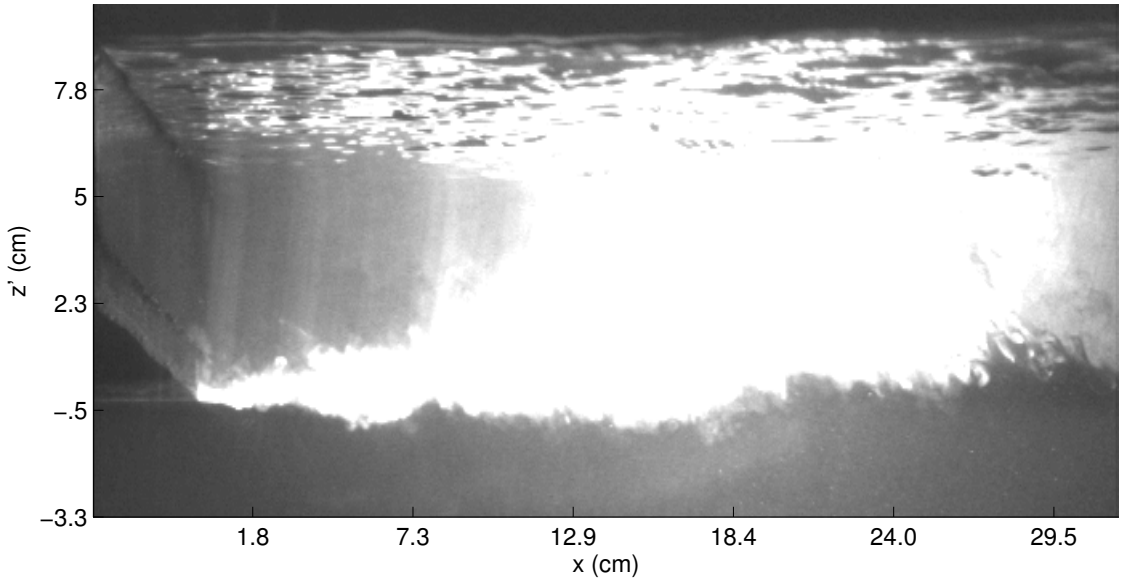

(b)

Figure 5.3: Images using a LIF technique with dye injected into the recirculation region. Images represent $F_T = 0.58$, and 0.75 for the top and bottom images respectively.

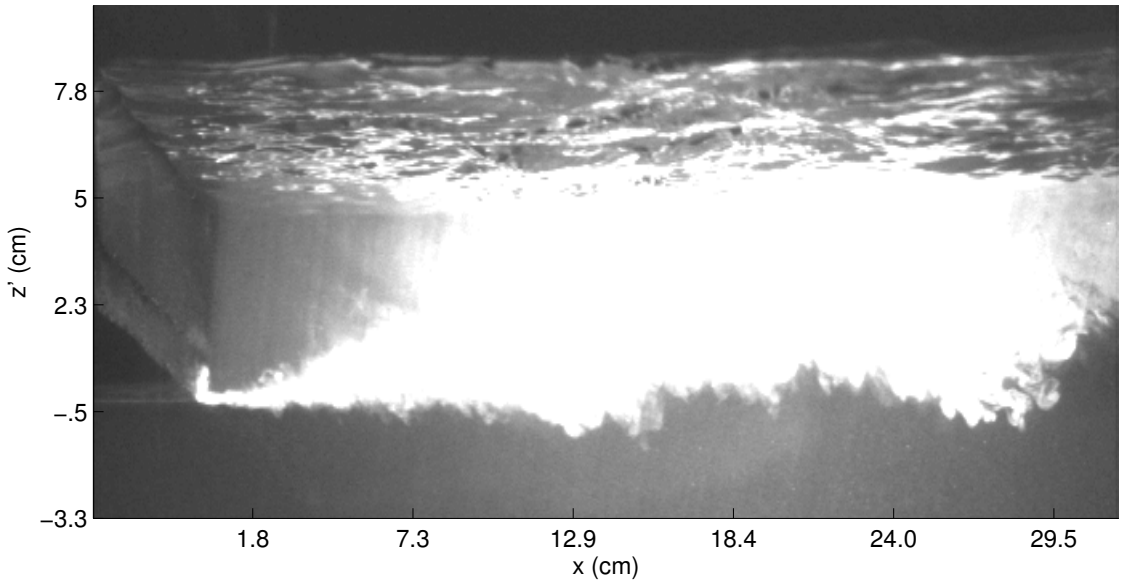

(a)

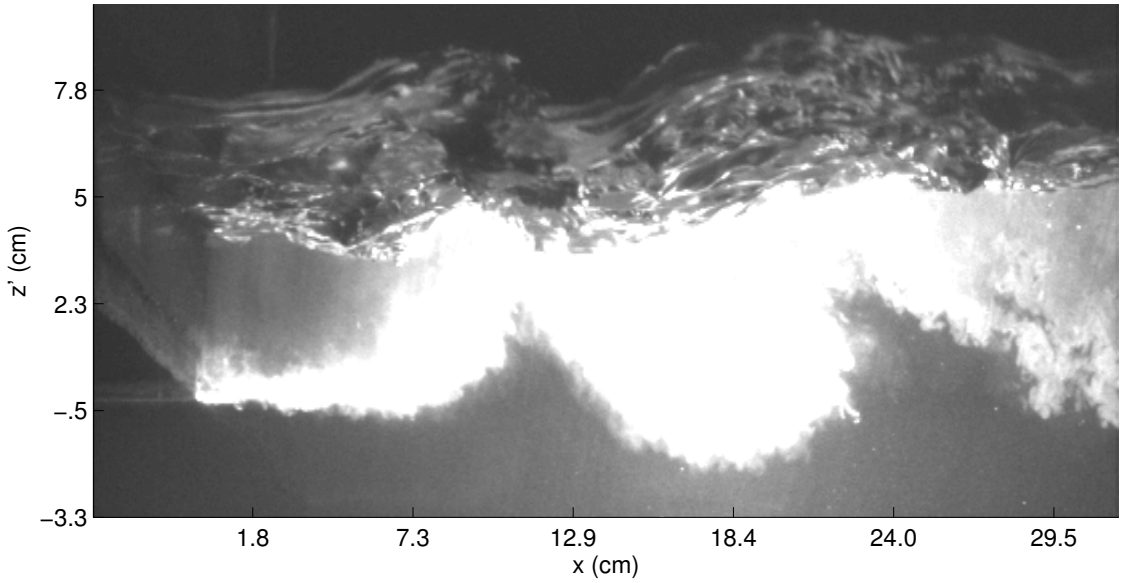

(b)

Figure 5.4: Images using a LIF technique with dye injected into the recirculation region. Images represent $F_T = 0.95$, and 1.18 for the top and bottom images respectively. The vortex-street is clearly visible, and its impact on the free surface in image (*b*).

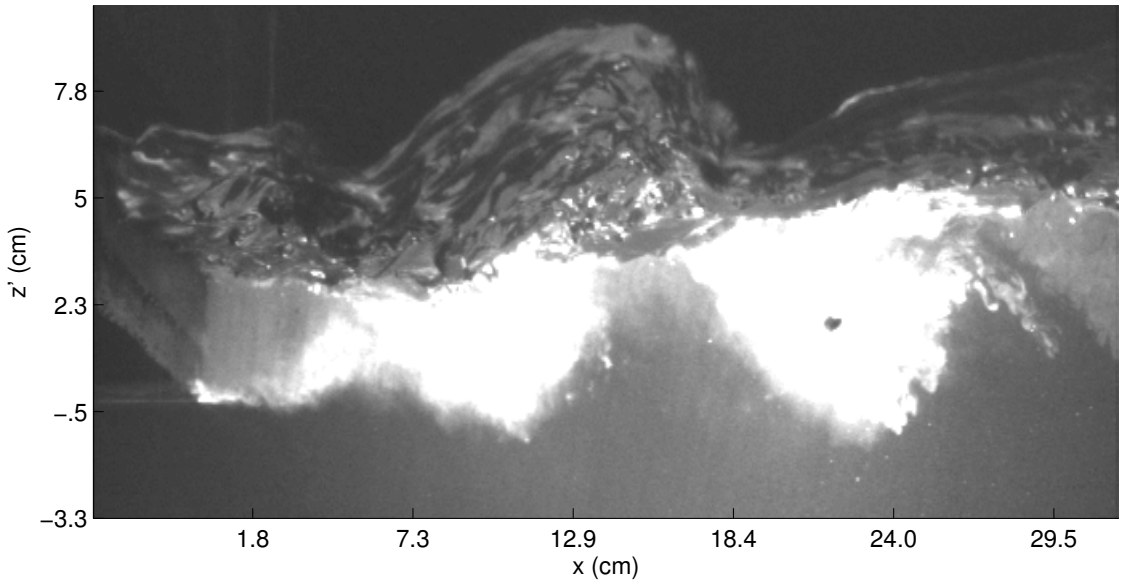

(a)

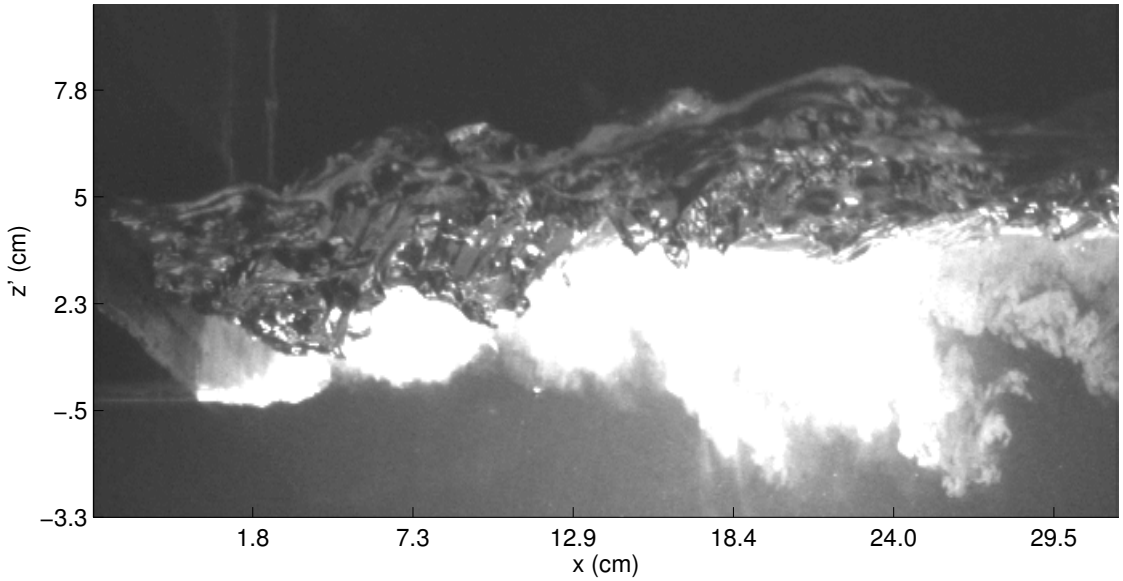

(b)

Figure 5.5: Images using a LIF technique with dye injected into the recirculation region. Images represent $F_T = 1.46$, and 1.75 for the top and bottom images respectively. The vortex-street is distinguishable in both images, as well as an air bubble in image (a) formed from a breaking wave.

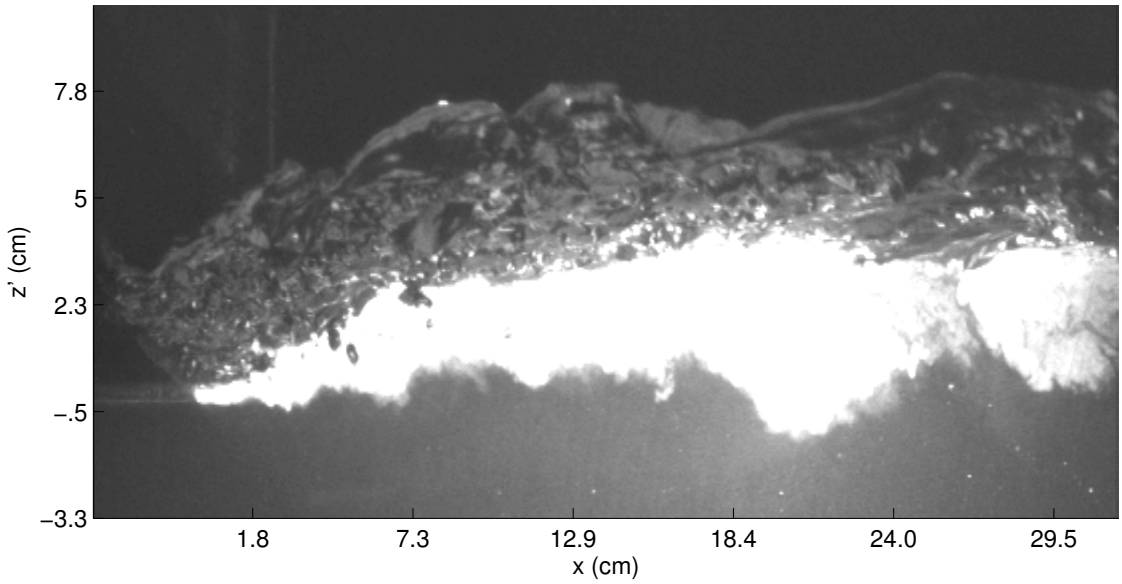

(a)

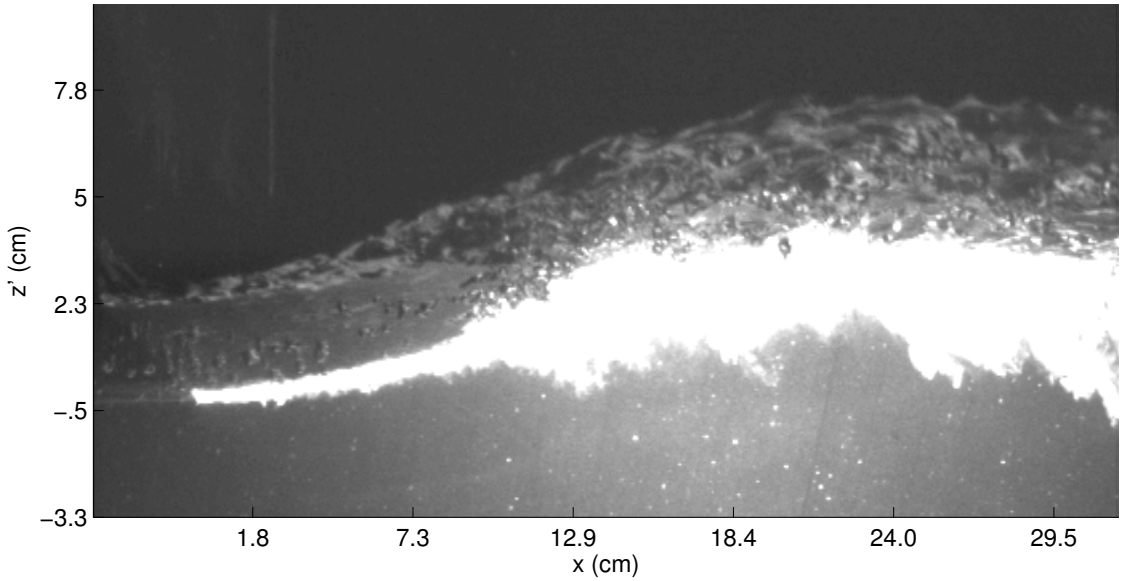

(b)

Figure 5.6: Images using a LIF technique with dye injected into the recirculation region. Images represent $F_T = 2.27$, and 2.98 for the top and bottom images respectively.The top image is at a Froude number near the onset of ventilation. The bottom image is post-ventilation, and displays the roller of the breaking wave, 10cm $< x_{toe} <$ 20 cm.

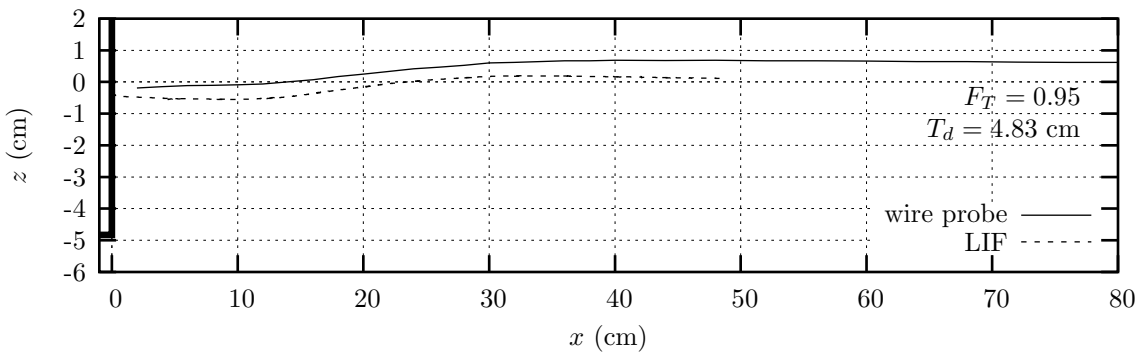

Figure 5.7: Mean free surface profile for Froude number of 0.95 as measured by the wire-capacitance probe and the LIF technique.

.

ized. By re-examining figure 5.1, the standard deviation of the free-surface elevation (recall σ is non-dimensionalized by the transom draft T_{d}) grows significantly between Froude numbers of 0.75 and 1.25. Near the Froude number of 1.25 the the standard deviation exceeds 20 percent of the transom draft which is a significant unsteadiness if one were to consider the wave in the wake of a ship.

The large fluctuation is an effect of the unsteady shear layer that originates along the keel, and evolves into a vortex-street. It *rolls-up* the free-surface, and then forms a propagating breaking wave. This vortex-street consists of vortices that are paired with one vortex existing in the water, and its counterpart in air. A frequency analysis of this is given later in section 5.4.

The transition between regimes 1 and 2 and the vortex-street can be seen in the images of figure 5.4. The flow in regime 1 (with its relatively flat free-surface) is similar to the canonical problem of a classical backward facing step with the exception that the downstream wall is a *slip* wall (figure 5.4 *a*). Figure 5.4 *b* shows the image for a Froude number after the vortex shedding phenomenon becomes present.

As the vortex-street emerges, a first wave crest appears in the mean profiles at a $F_T \approx 1$. The crest is located at a position that coincides with the location of

maximum unsteadiness. Experimentally a second wave does not appear until the Froude number reaches a value of approximately two. The delay in the appearance of the second wave is due to the intense energy diffusing mechanisms of wave breaking paired with the damping effects of surface tension.

After a Froude number of approximately two, the secondary residual wave appears. Several factors contribute to the birth of this wave. First, with increased flow speed more energy is transfered from the body to the fluid, thus challenging the mechanisms of viscosity and wave breaking to diffuse the energy before it can be radiated by gravity waves. Second, the Reynolds number based on body length is increasing (not the Re_T which is calculated with step height or transom draft and is relatively constant in these experiments, $Re_T \approx 2 \times 10^4$), as is the thickness of the boundary layer relative to the step height. The thicker inflow boundary layer degrades the coherency of the vortex-street which was the primary driver of the large free-surface perturbations that led to wave breaking. Concurrently, the volume of water above the separation streamline is decreasing with the falling free-surface location on the transom, thereby decreasing the thickness of the shear layer and ultimately reducing the magnitude of the turbulent diffusion.

Figure 5.5 shows the degradation of the vortex street. Also, the air entrained by the breaking waves can be seen as dark spots in the images.

In the speeds contained in the range $2.0 < F_T < 2.5$, the body of water above the separation streamline is *trapped* between the transom, and the first wave crest. Finally, at a Froude number of near 2.5, the transom fully ventilates. The precise value of ventilation is important for those who seek to accurately model the unwetting process, more details and discussion on the critical Froude number can be found in section 5.3.

At the speed of ventilation, this highly turbulent volume of water that previously resided above the separation streamline, becomes the roller of the breaking wave. As the Froude number is further increased, this toe of the roller moves up the face of the wave until it is eventually shed, thus leaving the attached, steady, gravity wave. Figure 5.8 shows the movement of the toe up the face of the breaking wave and figure 5.9 shows the location of the toe depicted in figures 5.8 b-d as well as the result from the numerical simulation of case 3 ($F_T = 3.0$). The location of the toe (x_{toe}) is determined by the x location of largest jump in r.m.s. and is shown with a linear fit to the six data points. The x intercept from the regression equation which represents the critical Froude number is $F_c = 2.46$ which is close to the value of 2.5 determined by the LIF measurements that are presented in section 5.3. Additionally, the breaking toe can be seen in the image of figure 5.6 *b* where the roller is located in the range 10cm $<$ x $<$ 20 cm for $F_T = 2.98$.

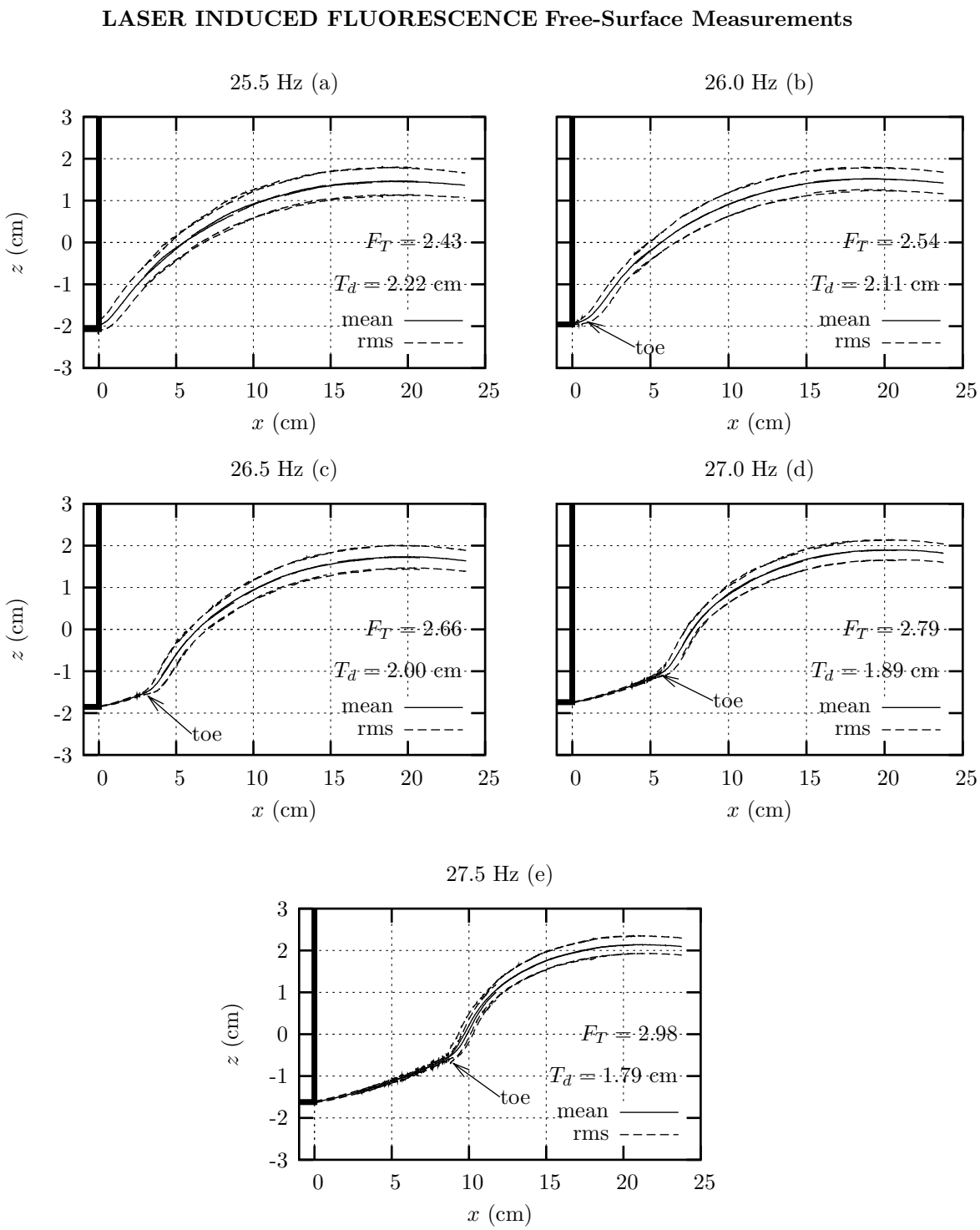

Figure 5.8: Mean free-surface elevation from series 1.2 measured with the LIF technique. The dashed line represents +/- 1 standard deviation.

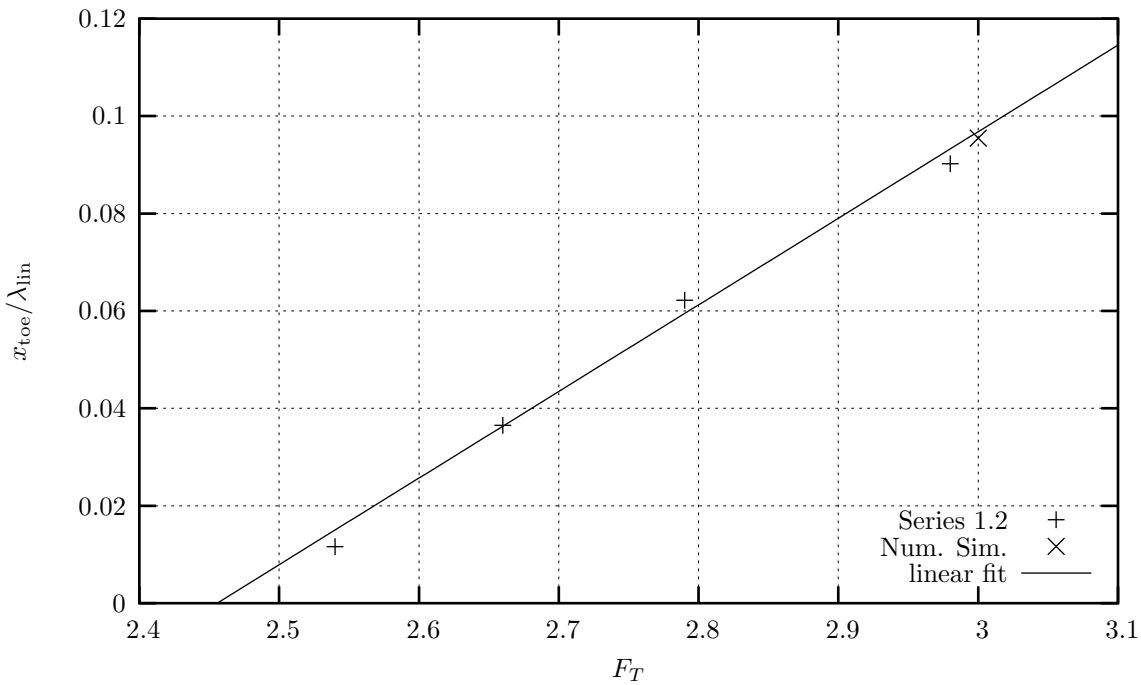

Figure 5.9: The location of the breaking toe as determined by the maximum r.m.s. plotted versus Froude number. The data is taken from the LIF measurements depicted in figure 5.8 b-e and the numerical simulation for $F_T = 3.0$.

Finally, the post-ventilation residual wave is shown in figure 5.10 as measured with the sonic wave probe. Here the word *residual* refers to the waves propagating downstream of the first breaking crest, and follows terminology of Duncan (1983a). The amplitude of the second wave approaches the magnitude of the first crest as the Froude number increases. Due to the spatial averaging of this device (see section 3.3.3 for sonic probe details), it is not possible to discern whether a breaking toe is present.

The precise speed at which the toe is shed was not experimentally measured. From general observations on the experimental set-up for series 1.2, the toe shed near a Froude number of 4.

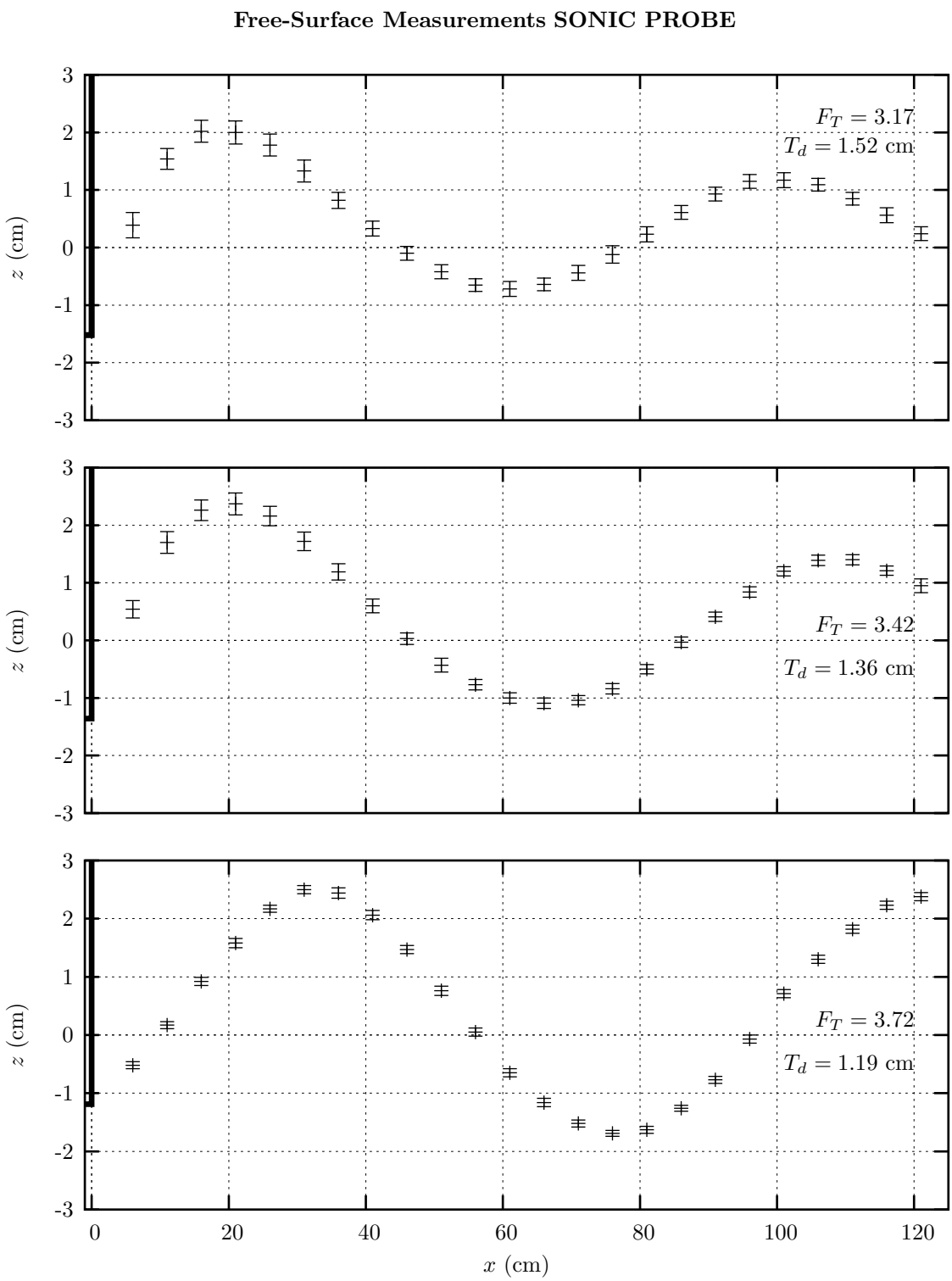

Figure 5.10: Mean free-surface elevation measured with a sonic wave probe. The error bars represent +/- 1 standard deviation in the elevation.

5.2 Wave Profile Statistics

The wave resistance of a two-dimensional body can be determined by the steepness of the waves generated by the body moving through the fluid (Duncan (1983b), Duncan (1983a), Walker, Lyzenga, Ericson, and Lund (1996)). The influence that a transom stern has on resistance is difficult to quantify accurately, but important information can be extracted from the parameters describing the wave profiles generated behind the body, namely the wave amplitude, steepness, and length.

Comparisons in this section are made with the previous numerical and analytical work of Vanden Broeck and Tuck (1977) and Vanden Broeck (1980). These references provide predictions from potential flow theory for the wave steepness and length for a two-dimensional semi-infinite body similar to the BFSFS. Vanden Broeck and Tuck (1977) presents a low-speed solution for wave steepness with the caveat that the flow near the body is unrealistic, while away from the body the solution is plausible. Specifically, the stagnation point where the free-surface meets the transom climbs vertically upward with increasing Froude number which is contrary to reality.

In Vanden Broeck (1980), a complementary high speed solution is presented for the wave steepness, as well as solutions for the wave amplitude and length. The high speed solution is valid for cases in which the transom is dry, and becomes singular near a Froude number of 2.23 (the steepness goes to infinity). The high speed problem is also studied by Scorpio (1997) where they simulate the specific Froude number of 6.3.

Table 5.1 contains the various parameters that describe the BFSFS wave profiles. The amplitude of the first crest a_1, is measured as the vertical distance from the mean free-surface to the highest point on the crest. The second crest a_2, is defined

Table 5.1: Parameters from Experimental Wave Measurements

	F_T	Re_T	T_d (cm)	a_1/T_d	a_3/T_d	λ (cm)	λ/T_d	s_1	s_3
	1.57	1.49×10^4	2.26	0.71	-	-	-	-	-
	1.67	1.44×10^4	2.13	0.17	-	-	-	-	-
Series 1.1	1.92	1.36×10^4	1.86	0.25	-	-	-	-	-
$T_\mathrm{o} = 4.2$ cm	2.23	1.23×10^4	1.57	0.33	0.062	38.96	35.80	0.0264	0.0048
	2.63	1.05×10^4	1.27	0.50	0.141	44.12	36.46	0.0295	0.0077
	3.35	0.79×10^4	0.89	1.28	0.507	53.15	54.23	0.0214	0.0187
	0.95	2.83×10^4	4.83	0.04	-	-	-	-	-
	1.18	2.69×10^4	4.32	0.07	-	-	-	-	-
	1.46	2.96×10^4	3.75	0.14	-	-	-	-	-
Series 1.2	1.75	2.94×10^4	3.30	0.26	0.013	43.23	14.17	0.0401	0.0019
$T_\mathrm{o} = 6.35$ cm	2.27	2.42×10^4	2.45	0.47	0.060	-	-	-	
	3.17	1.89×10^4	1.52	1.18	0.625	81.30	53.48	0.0509	0.0234
	3.42	1.51×10^4	1.36	1.36	0.909	88.54	64.16	0.0535	0.0283
	3.72	1.34×10^4	1.19	1.54	1.682	88.65	73.26	0.0568	0.0459
	1.5	4.00×10^4	-	0.099	0.058	-	7.92	0.0248	0.0147
Numerical	2.0	4.00×10^4	-	0.411	0.241	-	17.58	0.0467	0.0273
Simulations	2.5	4.00×10^4	-	0.819	0.634	-	31.52	0.0519	0.0400
	3.0	4.00×10^4	-	0.695	0.705	-	46.47	0.0299	0.0303
	3.5	4.00×10^4	-	0.777	0.647	-	66.72	0.0233	0.0194

as the distance between the lowest point between the two crests and the highest point in the second crest. The horizontal distance between the first and second crest is reported as the wave-length (λ). Using the amplitude for each wave, a_1 and a_2, the wave steepness is calculated as twice the amplitude divided by the wave-length ($s_i = 2a_i/\lambda$, for $i = 1, 2$).

To demonstrate the process of wave generation, figure 5.11 shows the amplitudes of the first and second crest from series 1.1 and 1.2 and the numerical simulations (non-dimensionalized with transom draft) compared to results from Vanden Broeck (1980). Also, the steepness solution from Vanden Broeck and Tuck (1977) is used with the linear gravity wave-length to *construct* the curve for the wave amplitude seen in this figure.

The real-fluid first wave crest begins to appear at a $F_T = 1$ and seems to grow linearly in Froude number over the measured speed range $F_T < 3.75$. The agreement

between the numerical simulations and the experiments is good for determining the first wave crest for $F_T < 2.5$. For $F_T > 2.5$, the numerical amplitudes plateau while the experimental amplitudes continue to grow.

The second wave emerges near $F_T = 2$ in the experiments, and earlier at $F_T = 1.5$ for the numerical simulations. The second wave grows quadratically in amplitude until it reaches the amplitude of the first crest. The amplitude of the second wave approaches that of the first crest as the breaking toe is finally shed experimentally, while the two amplitudes numerically are close in value throughout the range of speeds.

The disagreement between the numerical simulations and the experiments in determining the second wave amplitude is most likely attributed to the poor representation of the smaller scales of turbulence in the simulations, or due to the damping effect of surface tension present in the experiments. The surface tension coefficient of the water from the channel during the experiments was measured using the annular slide technique and apparatus as described in Lapham, Dowling, and Schultz (1999). The static surface tension coefficient was measured as 66.71 ± 0.6 dyne/cm (the $\pm$ represents the standard deviation of five measurements). Interestingly, this value is near that of which damping is the greatest (Lapham, Dowling, and Schultz 2001).

It is interesting to see that the potential flow solutions of Vanden Broeck (1980) actually have the opposite behavior of the real-fluid, i.e. the wave amplitude (which is equal for all downstream waves due to lack of energy dissipation) grows with *decreasing* Froude number. The real-fluid has significant influence from the presence of viscosity, so it is not surprising that the potential flow solution does not agree well.

The next quantity to consider is the wave steepness. The steepness, which is

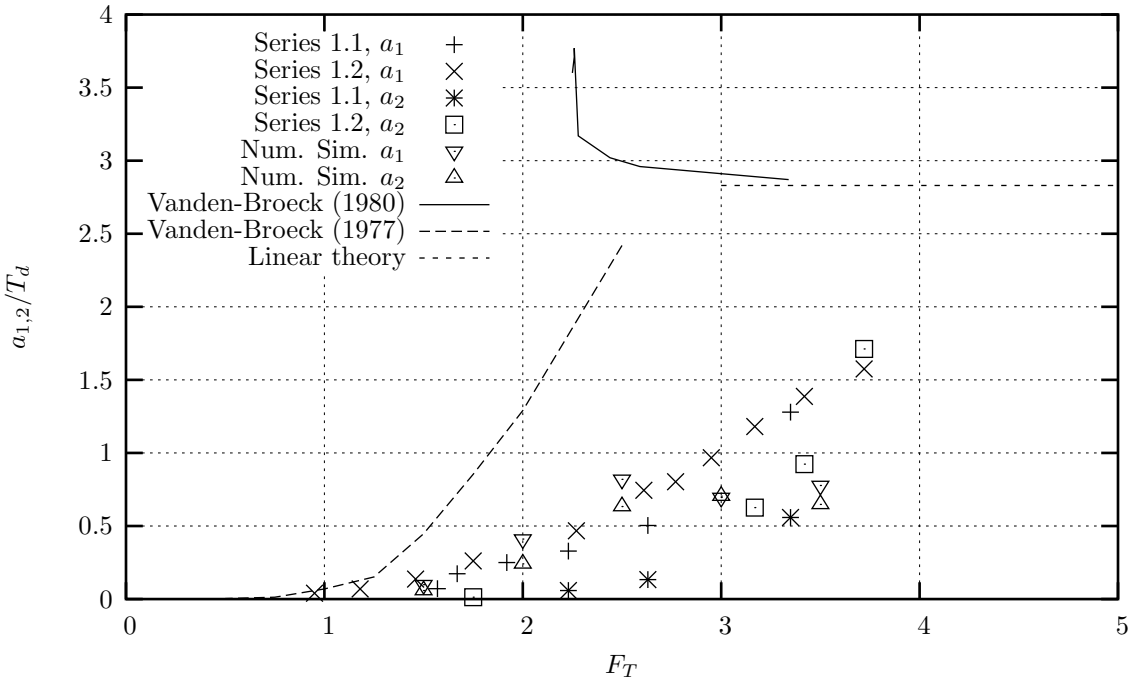

Figure 5.11: Wave amplitude normalized by transom draft for the first and second crests following the body. Data from both series 1.1 and 1.2 and the numerical simulations are shown. Solid line represents calculated results from Vanden Broeck (1980). Dashed line obtained by using sine waves of linear theory, $a/T_\mathrm{d} = 2^{3/2}$.

defined as twice the wave amplitude divided by the wave length, is the variable that determines resistance of a two-dimensional body as shown in Duncan (1983b). Figure 5.12 compares the experimentally measured and numerically predicted values of steepness with the reported predictions from Vanden Broeck and Tuck (1977) and Vanden Broeck (1980).

The numerical results for both the first and second waves follow the trends of the low and high speed solutions. The second crest has a smaller value for slope compared to the low-speed solution, explained by the presence of viscous diffusion present in the simulations which is absent in the potential flow theory. Viscosity also can account for the difference between the simulations and the high-speed solution.

Experimentally, the results for the first crest from series 1.2 exceed the the high-speed solution and continue to increase with increasing Froude number. Conversely the three data points for the first crest from series 1.1 behave more like the numerical solutions having a maximum near the critical Froude number. The experimental second wave crest is very small in magnitude, and grows to the value of the first crest with increasing Froude number. This is commensurate with the explanation that damping due to surface tension together with viscosity are significant when the transom is wet and when a breaking roller is present on the first wave.

Another perspective that examines the high-speed wave-slope experiments is to use the local slope of the face of the wave at a location upstream of the rolling breaker, instead of the amplitude to length ratio. The angle at which the flow leaves the body is measured from series 2.2, 2.3, and 2.4, and then plotted along with the wave steepness solutions from Vanden Broeck (1980) in figure 5.13 (note: the wave-steepness is defined as $2a/\lambda$ which is different from the local angle of the free-surface to the horizon). The angle of the pre-breaking wave slope shows the same Froude

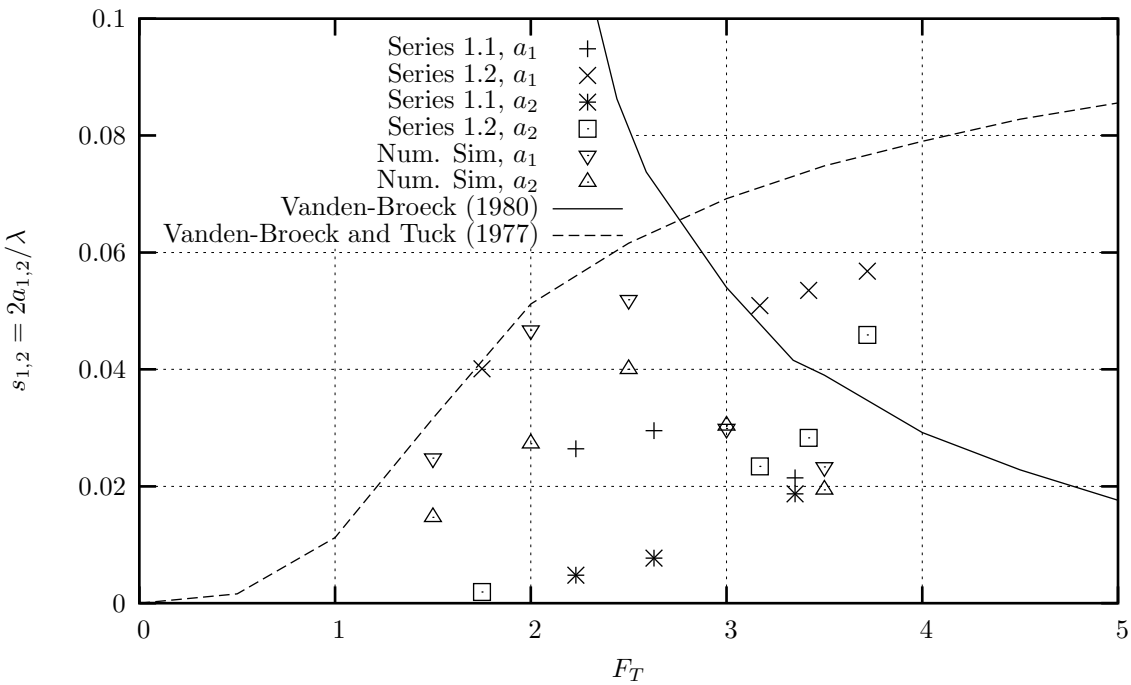

Figure 5.12: Wave steepness ($s = 2a/\lambda$) from experiments in both series 1.1 and 1.2 and the numerical simulations. Solid line represents calculated results from Vanden-Broeck (1980). The dashed line shows the solution from Vanden-Broeck and Tuck (1977).

number dependence as the high-speed potential flow wave steepness, signifying that the inviscid portion of the real fluid wave behaves as the inviscid theory would predict.

To examine the wave-length generated by a BFSFS, figure 5.14 shows the measured length plotted as a ratio to the linear theory length, $\lambda_{\text{lin}} = 2\pi U^2/g$, and compared to the predictions from Vanden Broeck (1980). Additionally, there are three curves from the bi-linear shear current stream function theory of Dalrymple (1974) that account for the vorticity of the wake.

Non-linear waves, or waves with appreciable steepness, are shorter than their linearly predicted values as noted by higher order Stokes wave theory. Accordingly, the results from Vanden Broeck (1980) reflect the slightly shorter wave-length for waves of significant steepness. When a real fluid is considered, there exists a wake behind

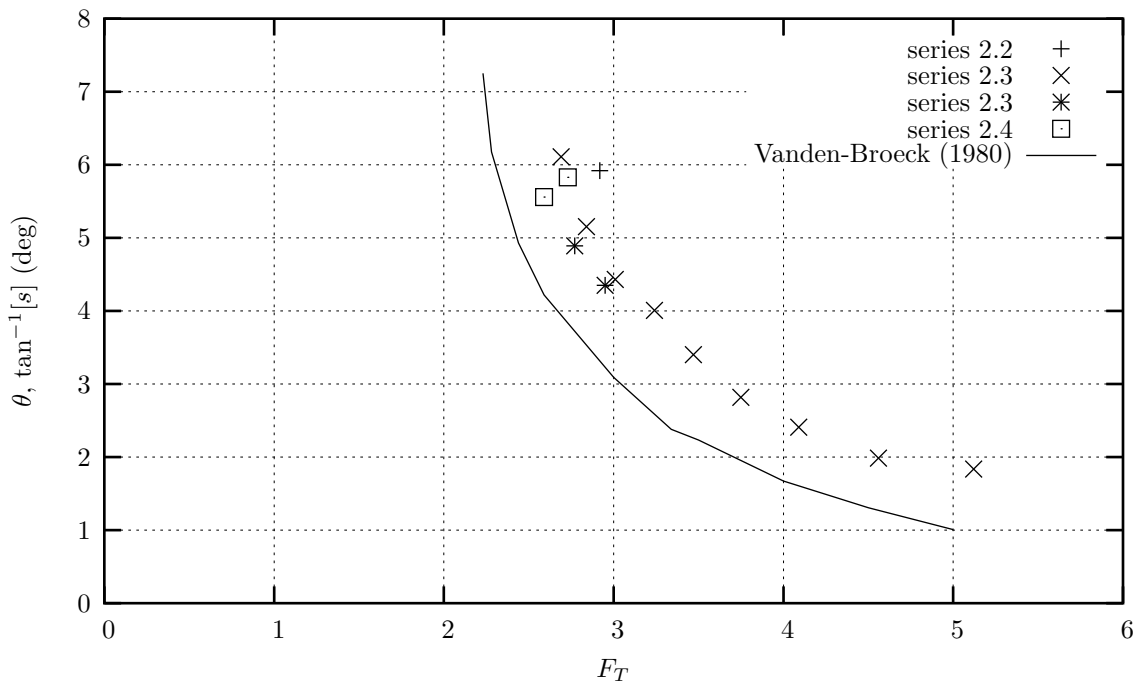

Figure 5.13: Angle of the free-surface for speeds after ventilation. θ is measured relative to the horizon, calculated using the elevations at x locations of 0.5 cm, and 1.0 cm. The solid line is the solution for wave steepness from Vanden Broeck (1980).

the body and its effect significantly reduces the wave-length, which is unaccounted in irrotational potential flow theory.

Subsequently, the theory of Dalrymple (1974) uses the stream function to describe a wave propagating over a bi-linear shear current. The deep-water small-amplitude dispersion relation is

$$\left[\frac{u_{fs}-U}{Ud}+k\right]\left[u_{fs}^2-\left\{g+\frac{u_{fs}\left(u_{fs}-U\right)}{d}\right\}\frac{\tanh(kd)}{k}\right]= g+\frac{u_{fs}(u_{fs}-U)}{d}-u_{fs}^2 k\tanh(kd) \tag{5.1}$$

where u_{fs} is the velocity on the free-surface, d is the thickness of the wake, and $k = 2\pi/\lambda$ is the wave number (see figure 5.15). The transcendental equation (5.1) can be solved for the wave number with a given set of values for u_{fs}, U, and d. Within

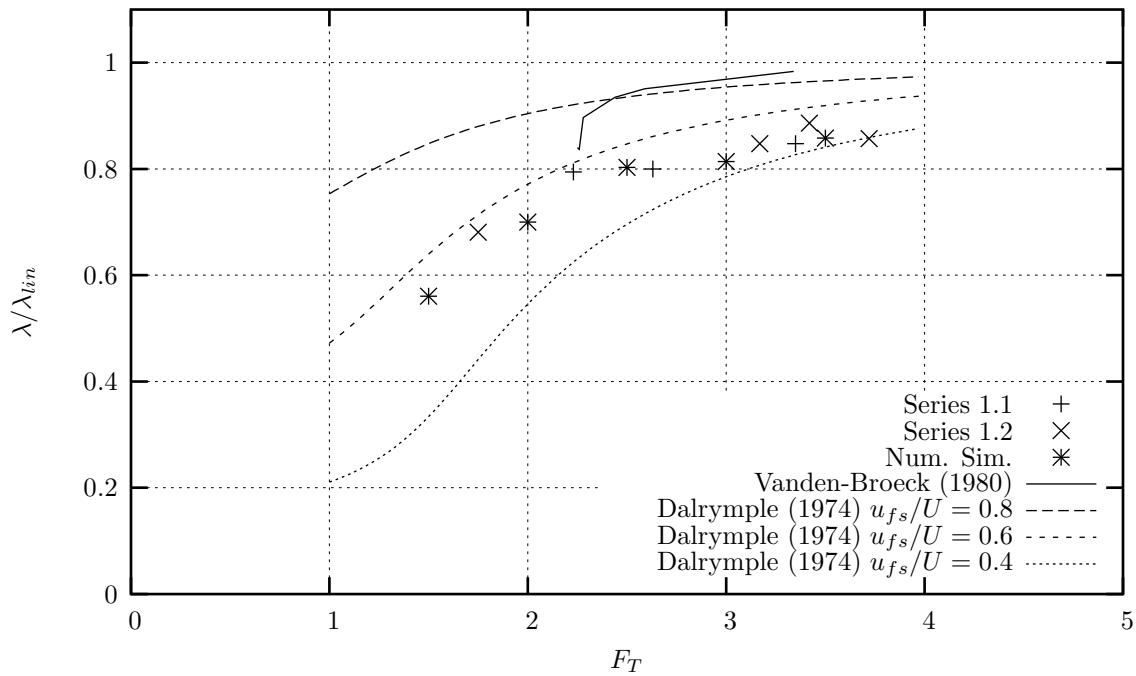

Figure 5.14: Experimentally measured wave-length (λ is the distance between the first and second crests) compared to the linear wave theory length calculated with free-stream velocity ($\lambda_{\text{lin}} = 2\pi U^2/g$). Results from both series 1.1 and 1.2 and the numerical simulations are shown. Solid line represents calculated results from Vanden Broeck (1980). The dashed lines are from the stream function theory of Dalrymple (1974).

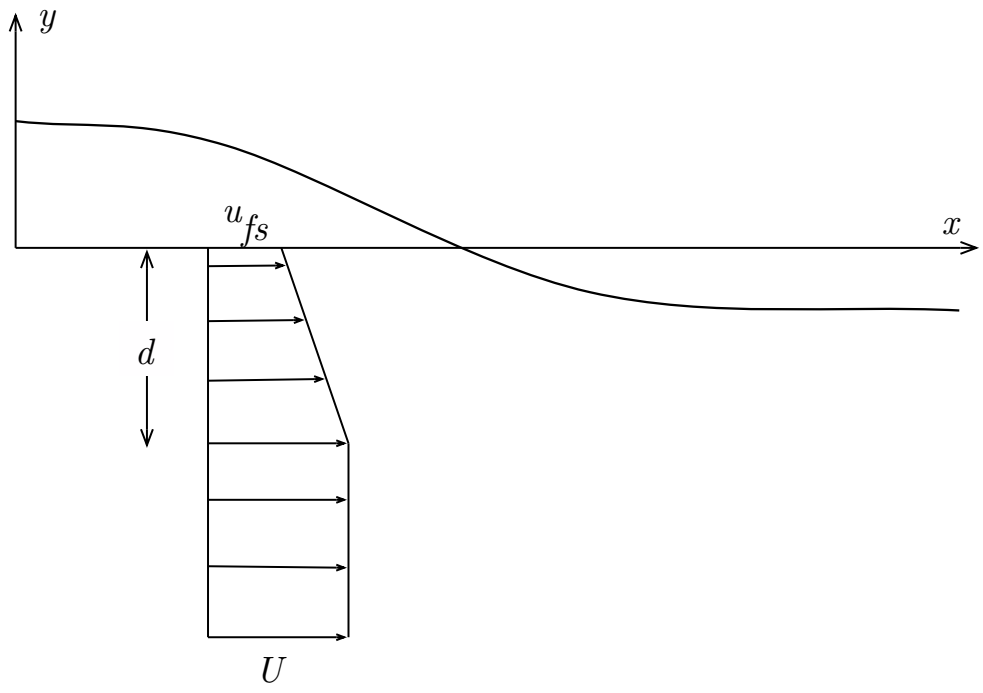

Figure 5.15: Wave propagating over a bi-linear shear current.

the data-set obtained in this thesis, information about the velocity profiles behind the body in the Froude number range of interest are available from the numerical simulations.

The determination of the free-surface velocity and thickness of the wake is complicated due to the nature of the BFSFS flow. The maximum defect velocity decays as $\sim x^{-1/2}$ in a single-phase turbulent plane wake, but oscillates due to the orbital velocity of the free-surface wave. The wake thickness suffers from the same complication. To demonstrate this point, the free-surface velocity from the numerical simulations is shown in figure 5.16.

To use the bi-linear shear-current theory, a model is sought to determine the wake thickness and defect velocity. Perhaps the simplest model for the thickness is that it would be proportional to the transom draft. Certainly the wake increases in

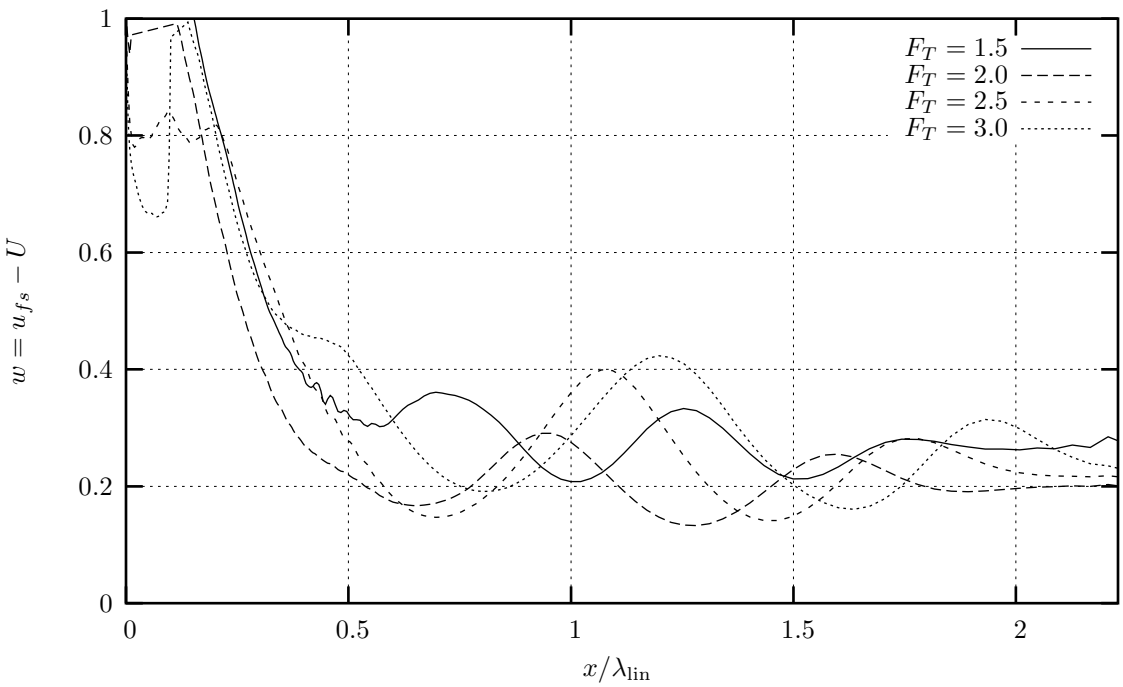

Figure 5.16: Free-surface velocity for F_T=1.5, 2.0, 2.5, 3.0, from numerical simulations.

thickness in the downstream direction, but for the range containing the first wave-length behind the body, a value of twice the transom draft is used.

In lieu of modeling the free-surface velocity, solutions for several values are used to construct curves of wave-length as a function of Froude number seen in figure 5.14. The numerical velocity profiles and those of the modeled bi-linear profile, are visualized in figure 5.17. The three values of the free-surface velocity shown for the bi-linear profiles are $u_{fs}/U = 0.4$, 0.6, and 0.8. The three stream-wise locations correspond to the first and second wave crests, and the first wave trough.

By comparing the bi-linear and numerical profiles in figure 5.17 the wake-thickness model of twice the transom draft appears to be plausible. Also, by interpolating the bi-linear theory curves in figure 5.14, the experimental and numerical data would follow a curve for a non-dimensional free-surface velocity value of approximately 0.55. The averages of the free-surface velocity from the numerical profiles at the

three chosen locations are 0.5, 0.59, 0.51, and 0.56 (F_T = 1.5, 2.0, 2.5, 3.0). This confirms that the wake thickness model implemented with the stream function theory properly explains the short waves behind the body.

5.3 Transom Un-wetting

Full-scale ship wave resistance is predicted efficiently by state-of-the-art potential flow methods. When simulating ship hulls with transom sterns, these methods need additional information to model the flow in the transom wake.

A model by Couser, Wellicome, and Molland (1998) extends the length of the ship by adding an appendage to model the free-surface hollow. In this application, the length of the hollow is deduced by considering the canonical problem of a single-phase turbulent backward facing step. They use the guidance that for this problem, the flow re-attaches at a downstream distance of approximately six step heights. Using a model based on this rule-of-thumb , a significant improvement to the prediction of resistance is realized.

Another technique to model the transom stern for a potential flow application was developed and documented in Doctors and Day (1997), Doctors and Day (2000), and Doctors (2003). This approach attempts to describe the hollow behind the ship by predicting the free-surface location on the body, and the length of the hollow behind the transom. Suggested in the research report by Oving (1985), the location of the free-surface on the transom moves downwards in a dynamic pressure sense, or more specifically, as the square of the velocity. It is shown in Doctors (2003) that the treatment of the un-wetting process is essential for resistance predictions of this type, i.e. ignoring a partially wetted transom grossly over predicts resistance due to the neglect of the thrust provided by the stagnant water on the transom. It is

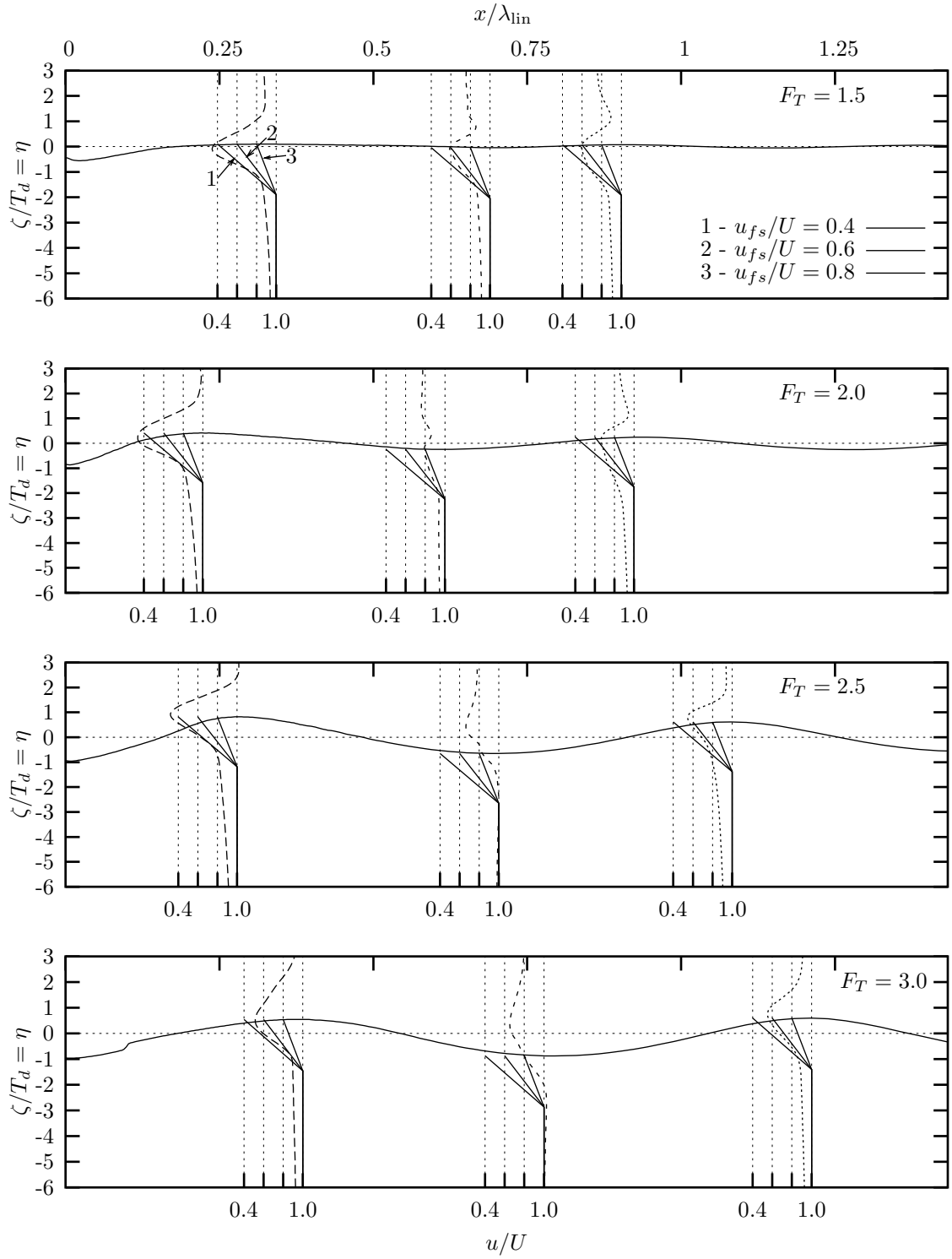

Figure 5.17: Velocity profiles from numerical simulation and modeled bi-linear profiles for Froude numbers 1.5, 2.0, 2.5, 3.0 (top-bottom). The profiles are shown from three stream-wise locations representing the first crest, first trough, and second crest.

noted that also in Cheng (1989), where a higher order potential flow implementation is used, the exclusion of a transom wetting model may explain the over-prediction in wave resistance reported for lower speeds.

For comparison in this section, the novel model for transom un-wetting as introduced by Doctors (2003) will be used. He describes un-wetting based on Bernoulli equation reasoning, and then uses experimental measurements to refine the pressure coefficient. Also, Maki et al. (2005) supplements Doctors original work with portions of the results that are documented in this thesis.

To describe the vertical location of the free-surface on the transom, a non-dimensional parameter is introduced

$$\eta_{\mathrm{dry}} = \frac{-\zeta(x=0)}{T_{\mathrm{d}}} \tag{5.2}$$

This parameter η_{dry} represents the fraction of the transom that is wetted. When the transom is completely immersed, $\eta_{\mathrm{dry}} = 0$, and when the transom is dry, $\eta_{\mathrm{dry}} = 1$.

The free-surface on a partially ventilated transom is highly unsteady, and therefore difficult to measure. It is hypothesized that the pressure in the separated flow is hydrostatic, in which case the pressure on the transom at the keel would reflect the position of the free-surface on the body. Subsequently, another parameter is defined in a similar manner to η_{dry}, that is

$$\psi_{\mathrm{dry}} = \frac{-p}{\rho g T_{\mathrm{d}}} \tag{5.3}$$

In the present experiments, a pressure tap was located at the point where the transom meets the keel. Using LIF and pressure measurements, data were collected for a range of Froude numbers. A summary of the test conditions is presented in table 5.2.

Table 5.2: Test matrix and parameters for transom un-wetting experiments. T_o is calm water transom draft.

Series	Technique	T_o (cm)	F_T min-max	$Re_T \times 10^{-4}$ min-max	$Re_L \times 10^{-6}$ min-max
2.1	Pressure	3.43	0.8-4.1	1.0-0.4	0.7-1.4
2.2	Pressure	5.03	0.6-3.0	1.5-1.2	0.6-1.7
2.3	Pressure	6.35	0.6-2.8	2.2-2.0	0.7-1.9
2.4	Pressure	7.66	1.1-3.3	3.9-2.2	1.3-2.2
2.5	Pressure	8.92	1.1-3.1	4.9-2.9	1.4-2.3
2.1	LIF	3.82	0.8-3.1	1.2-0.8	0.7-1.5
2.2	LIF	5.10	1.1-2.9	2.0-1.3	1.1-1.7
2.3	LIF	6.35	0.4-4.6	1.5-0.8	0.5-2.1
2.4	LIF	7.61	1.2-2.7	3.7-2.6	1.3-2.1
2.5	LIF	8.93	1.1-2.5	4.9-3.7	1.4-2.2

In figures 5.18 and 5.19, the results for η_{dry} from the LIF and numerical simulations as well as results for ψ_{dry} from the pressure measurements are compared to an un-wetting model regression equation. The equation was first presented in Doctors (2003) and it appears here with the revised coefficients from Maki et al. (2005).

$$\eta_{\text{dry}} = C_1 F_T^{C_2}, \qquad C_1 = 0.1578, C_2 = 1.966 \tag{5.4}$$

The regression coefficients in equation 5.4 are from an experimental dataset of free-surface elevations measured with a wire wave probe which were conducted and reported in Doctors (2003). When this regression is used in the following figures, it will be labeled UNSW. The experiments represent a series of geosimilar models with parallel mid-body and Reynolds numbers centered around 2.0×10^6, which is the same magnitude of the BFSFS results.

In examining figure 5.18, the regression equation 5.4 is further validated by the present non-intrusive technique. Also, the present model is two-dimensional, or represents infinite beam-to-draft ratio (B/T), extending the experimental results from Doctors conducted on finite B/T. The agreement within the five series from the

BFSFS model is particularly good in the Froude number range, $1 < F_T < 2$. As the Froude number approaches that of ventilation, the scatter in the data increases for the series from the smaller calm water transom draft, namely series 2.1-2.3. At the smaller length scales, the presence of surface tension which creates a meniscus on the body, complicates the procedure in measuring the actual location of the free-surface on the body. It is desired to neglect the meniscus, therefore the location of minimum elevation is chosen to define the free-surface position. In the cases were the meniscus is relatively large, this location is a distance from the body which is of the order of magnitude of the meniscus. The free-surface height at these speeds increases monotonically from the body, and therefore, a measurement position some distance off of the body will record a value that is higher than what it would be without the effects of surface tension. This effect of measuring a higher value for the elevation decreases the value of η_{dry} and explains the scatter near ventilation in figure 5.18.

Figure 5.19 displays the data from the pressure measurements as compared to the regression equation. The trend of these data follows the regression equation, and therefore the LIF measurements, while showing a slight dependence on scale factor (the series numbers represent an increase in scale factor).

Figure 5.20 shows the value of ψ_{dry} as calculated from the pressure measurements in chapter 2 along with the UNSW regression. The destroyer model experiments were conducted at $Re \approx 10^7$, which is one decade greater than the Re of the BFSFS experiments. The pressure measurements show the ventilation, and the process of un-wetting to occur at greater Froude numbers than the regression. The data shown are for the scenario in which the model is free to sink and trim. When the model is fixed in all degrees of freedom, the difference in the results is indiscernible (Maki et al. 2005).

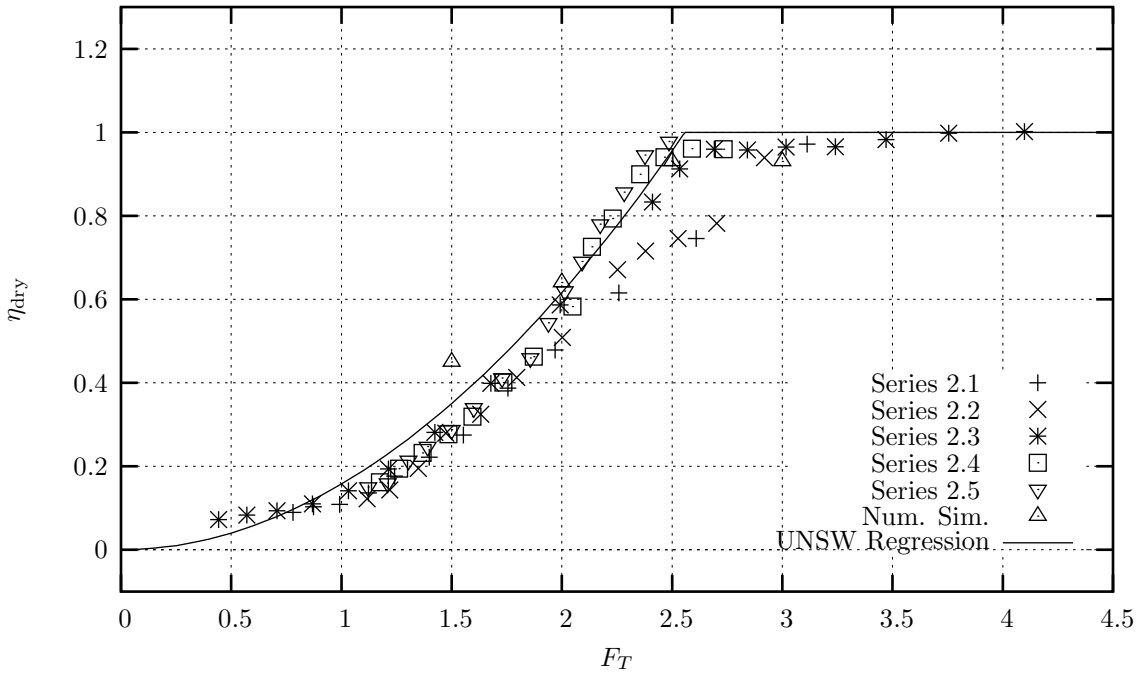

Figure 5.18: η_{dry} from present experiments compared to the regression equation 5.4.

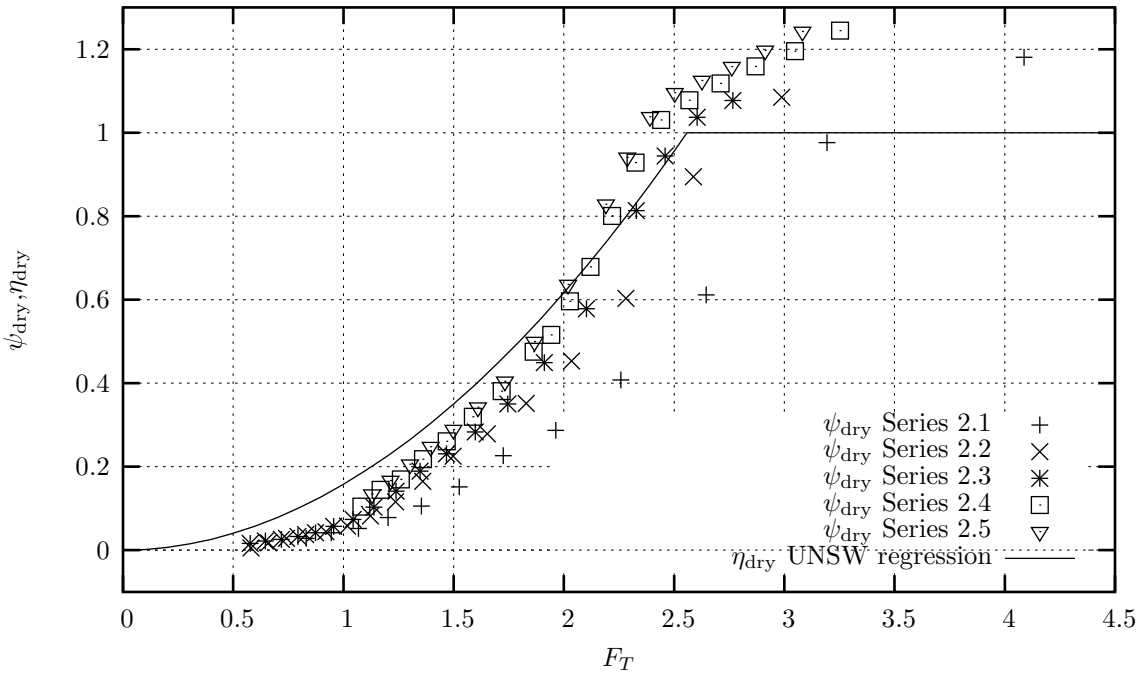

Figure 5.19: ψ_{dry} from present experiments compared to the η_{dry} regression equation 5.4.

In accordance with the general description of the four flow regimes, the transition between the first and second can be seen in figures 5.18 and 5.19 at a Froude number of one. The data are in excellent agreement in both figures for the first docile regime ($F_T < 1$). Then in the second regime, there is a slight offset from the regression, though its quadratic nature is followed closely.

In the smallest Reynolds number (based on length) series 2.1, the measured pressure is larger than the hydrostatic ally computed component. The surplus of pressure diminishes as the Reynolds number increases, and becomes negative in sign between series 2.3 and 2.4. Additionally, after ventilation, the measured pressure on the bottom of the transom continues to decrease. This is also evident in the pressures measured on the naval combatant model tested in the towing tank (figure 5.20) thus negating the possibility that this excessive pressure is due to unaccounted pressure gradients in the recirculating channel.

Unfortunately, a precise value for un-wetting is not accurately determined from this data set. It can be stated that the regression based on the work of Doctors (2003) is validated both in the quadratic nature of the equation, and its leading coefficient.

Additionally, by examining figure 5.19 along with the figure 5.20 which show ψ_{dry} measured on a ship hull in the model basin, it is seen that the pressure on the transom is dominated by hydrostatics. Considering the Reynolds number dependency, qualitative statements are difficult to deduce from the present study, but the advice that care should be taken as Reynolds number decreases can be offered, when assuming the pressure is wholly hydrostatic on the transom.

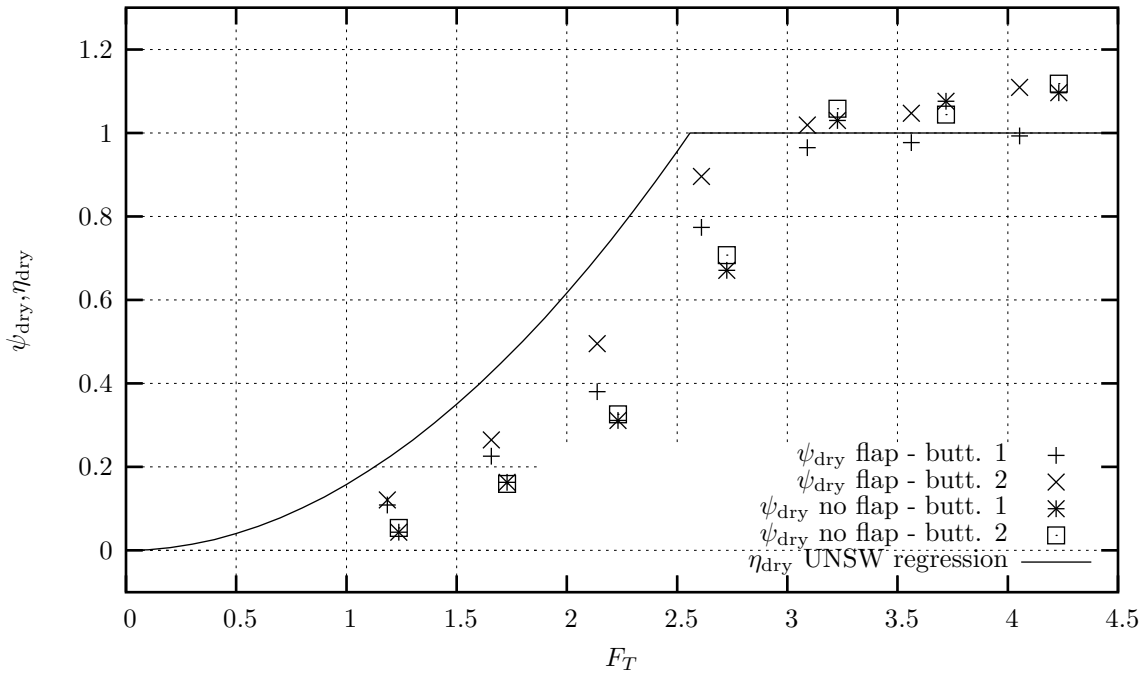

Figure 5.20: ψ_{dry} from Destroyer model experiments, with the model free to sink and trim, compared to the η_{dry} regression equation 5.4 .

5.4 Frequency Analysis

When experimentally observing this flow at certain speeds, the vortex shedding becomes obvious to the observer by the periodic unsteady wave seen in the first crest after the body. In this section, a spectral analysis is used to describe the frequency content of the free-surface.

The figures in this section are organized as follows: figures 5.21 and 5.22 show the magnitude of the largest Fourier coefficient compared to the statistical r.m.s. for series 1.1 and 1.2 respectively. Figures 5.23-5.28 contain contour plots of the discrete Fourier transform in increasing Froude number for series 1.1. Then, figure 5.29 shows the frequency spectra from each contour plot at the downstream location $x = 8$ cm.

The Fourier transform is taken at discrete downstream locations for each dataset from the LIF measurements in both series 1.1 and 1.2. The spacing was chosen

as 20 pixels which corresponds to 2.0 mm for series 1.1 and 2.6 mm for series 1.2. The Fourier coefficients represent the magnitudes of the complex amplitudes of each discrete frequency in the finite series. If a time series is monochromatic and infinite in length, the variance of the signal can be shown to be

$$\sigma^2 = \frac{1}{2}a^2 \tag{5.5}$$

where a is the amplitude of the signal frequency. In figures 5.21 and 5.22, the magnitude of the largest coefficient is plotted for each downstream location(non-dimensionalized by transom draft). If the free-surface times series was monochromatic representing a perfect vortex street, the largest coefficient would be related to the r.m.s. by equation 5.5 (this is ignoring any smearing due to the finite representation). Therefore, in figures 5.21 and 5.22, the statistically calculated r.m.s. is plotted scaled with the $\sqrt{2}$ for comparison to the Fourier Analysis.

At lower Froude numbers, the two approaches agree well, signifying the spectra are narrow-banded. As the Froude number increases, the largest coefficient deceases relative to the r.m.s. because the energy is spread over a wider band of frequencies.

A great amount of effort was spent on calibrating any deflection of the camera and optics as the traverse travels downstream. The results of the calibration are satisfactory in the mean profile figures in section 5.1. In the r.m.s. plots and Fourier analysis, there are discontinuities on the order of magnitude of 0.3 mm or approximately 3 pixels. The cause of the discontinuities must be attributed to the horizontal and vertical movement of the camera and laser optics.

An useful technique to describe the *broadness* of a spectrum consists of calculating the first three spectral moments m_0, m_2, and m_4, where the moment m_i is defined as

$$m_i = \int_0^\infty \omega^i S(\omega)\,\mathrm{d}\omega \tag{5.6}$$

The spectral broadness parameter is then defined as

$$\epsilon = \sqrt{1 - \frac{m_2^2}{m_0 m_4}} \tag{5.7}$$

For a narrow-banded process, the broadness parameter approaches zero. When there are multiple maxima the broadness parameter tends to unity, signifying a *broad* spectrum. This analysis was attempted, but due to the finite width of the spectra, the value of the broadness parameter was highly sensitive to the upper limit of integration in the moment integral approximations. Due to this sensitivity a high confidence estimate of the broadness parameter was unattainable.

Contour plots of the magnitude of the Fourier coefficient are shown in figures 5.23-5.28. A sub-set of the contour plots is shown in Figure 5.29 where the spectrum for the downstream location $x = 8$ cm is shown for each Froude number. The vertical bands in the contour plots depict the tiling of the different camera locations. Near the edges of the camera field of view, the laser-light sheet intensity is less. Therefore the quality of the edge detection is poorer resulting in a noisy Fourier representation.

At the Froude numbers of 1.46, and 1.67, the dominant frequency is easy to distinguish and persists far downstream. Also, in these plots, energy is also present at twice the dominant frequency, perhaps due to the breaking wave fluctuations propagating upstream.

As the contour plots are examined in the order of increasing Froude number, the dominant frequency increases in value as the spectra spread (the spreading is more easily seen in the figure 5.29). Also, in the area in front of the first crest ($x < 10$ cm), there is frequency content present between the dominant frequency and zero,

representing the 'trapped' body of water in front of the first wave crest.

In the figures of fully ventilated flow, the toe becomes evident in figure 5.27, (4cm < x < 10cm and $f < 1$ Hz) and pronounced in figure 5.28 (4cm < x < 6cm and $f < 4$ Hz). The frequencies in the toe region are much lower than the vortex street modes, and centered around zero. Experimentally the toe was observed to oscillate slowly forwards and backwards. Upon further examination of the contour plots, low frequency energy is present far downstream of the breaking wave. This is most likely an effect of partial reflection at the end of the channel test section.

The spectra for the first two speeds in figure 5.29 are narrow-banded making the choice of a dominant frequency obvious. As the Froude number increases in the remaining four speeds, the peak in the spectra loses its identity. To facilitate a Strouhal number analysis, the frequency of the largest Fourier coefficient at each downstream location is used to compute an average for all stream-wise locations representing the dominant frequency. The Strouhal number, $S_t = fT_{\mathrm{d}}/U$ is then calculated.

While vortex shedding commonly occurs behind bluff bodies, this is a particularly interesting case due to the free-surface that separates the vortex pairs. Figure 5.30 shows the Strouhal number for series 1.1 and 1.2, and from the numerical simulations plotted for each Froude number. It is noted that the Strouhal number for a circular cylinder is near 0.2 for the Reynolds number range of $100 - 10^5$ (White 1991).

The data from the present experiments and simulations are clearly centered around a Strouhal number of 0.2 except at higher Froude numbers and the post-ventilation regime 3 $F_T > 2.5$. At ventilation, the vortex street does not exist in the sense of a wake behind a bluff body (i.e. there is no trapped water when there is a dry transom). For post-ventilation, the content in the frequency range corresponding

to a S_t near 0.15 is attributed to the breaking wave crest. While reflection was mentioned earlier and probably present for these specific cases, reflection does not explain this behavior, as the Strouhal number is at a much higher frequency than the slow upstream-traveling reflected waves.

Upon inspection of the velocity fields and free-surface evolution figures from the numerical simulations, the breaking wave is causing the free-surface fluctuations at the dominant Strouhal frequency.

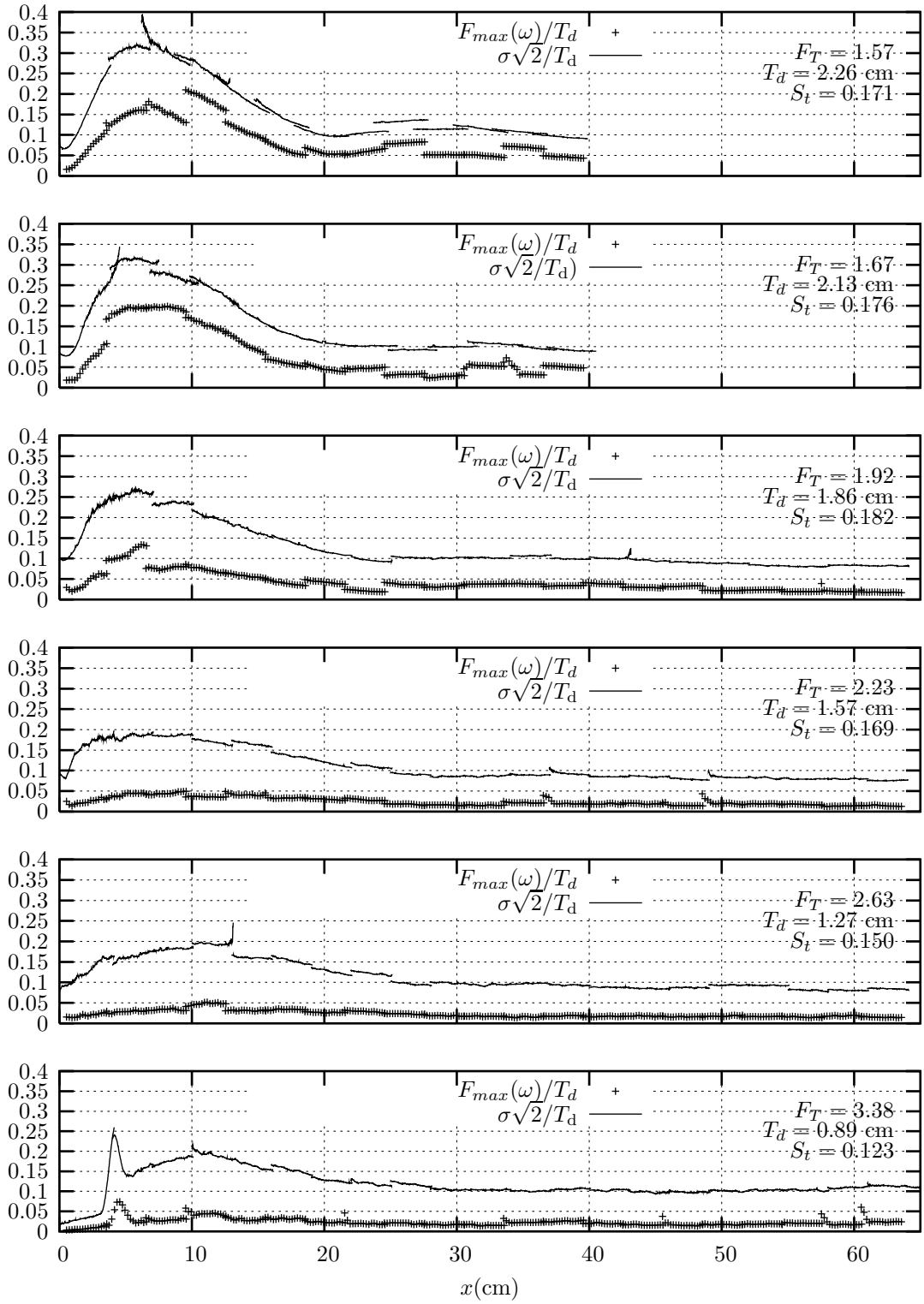

Figure 5.21: Amplitude of largest Fourier component, series 1.1.

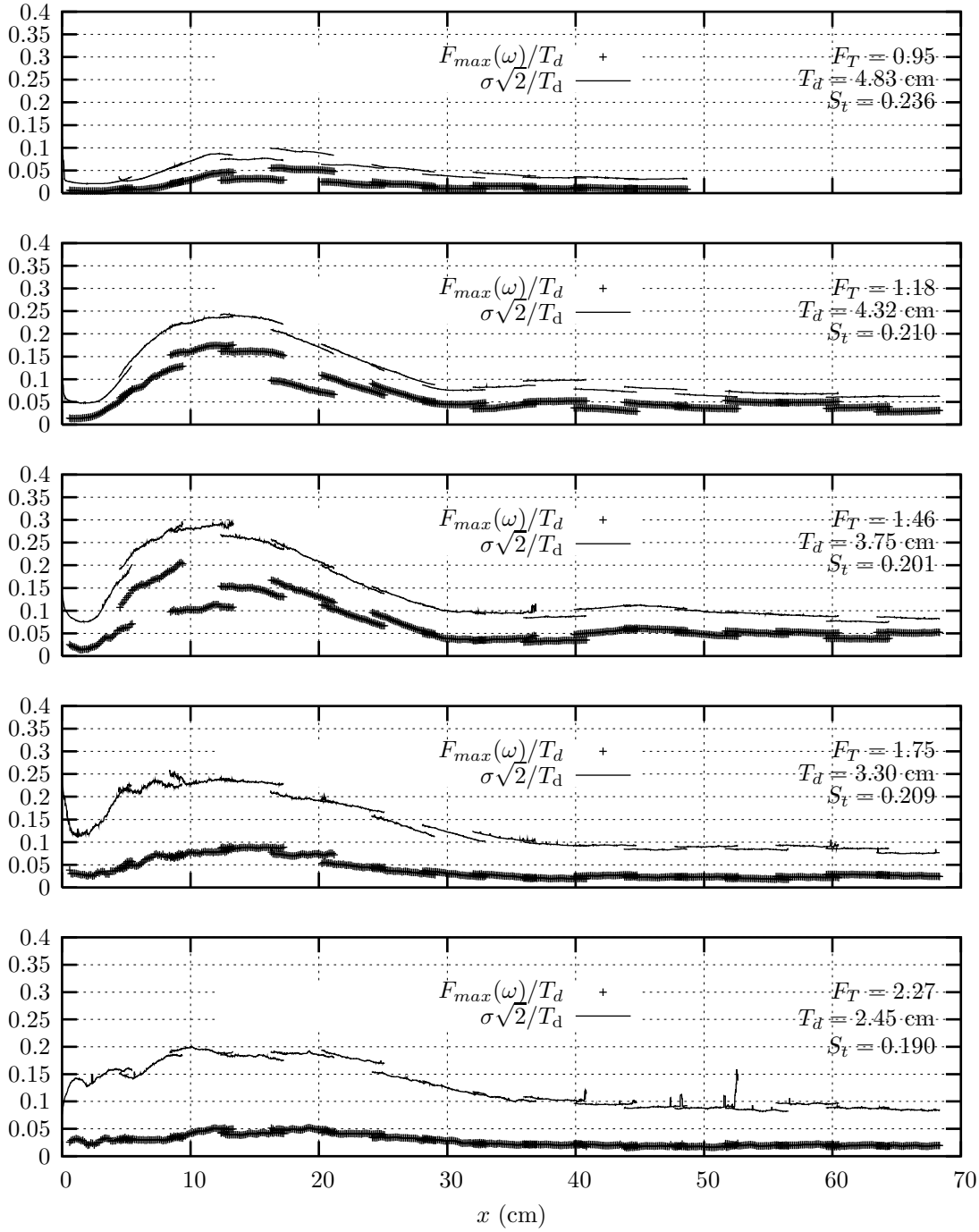

Figure 5.22: Amplitude of largest Fourier component, series 1.2.

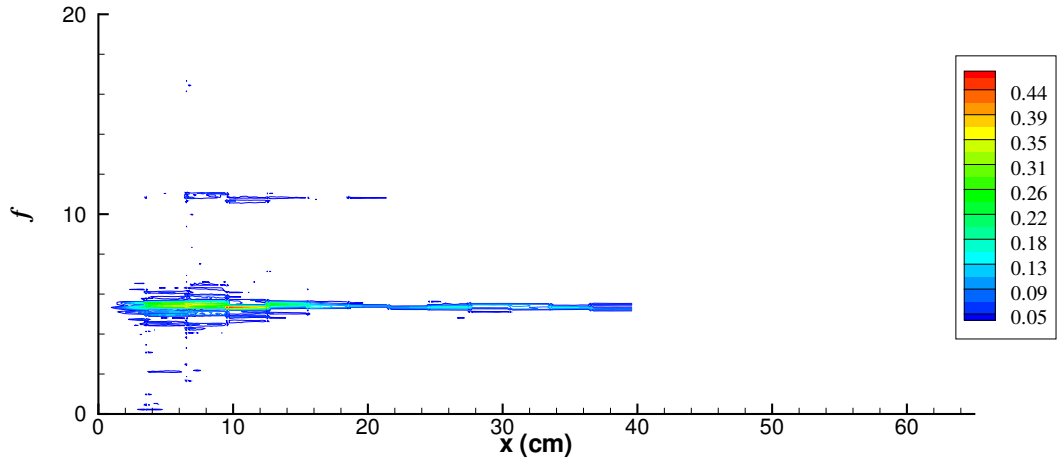

Figure 5.23: Frequency spectrum for the LIF measurements using series 1.1. f is in Hz. $F_T = 1.46$. and $T_\mathrm{d} = 2.42$ cm.

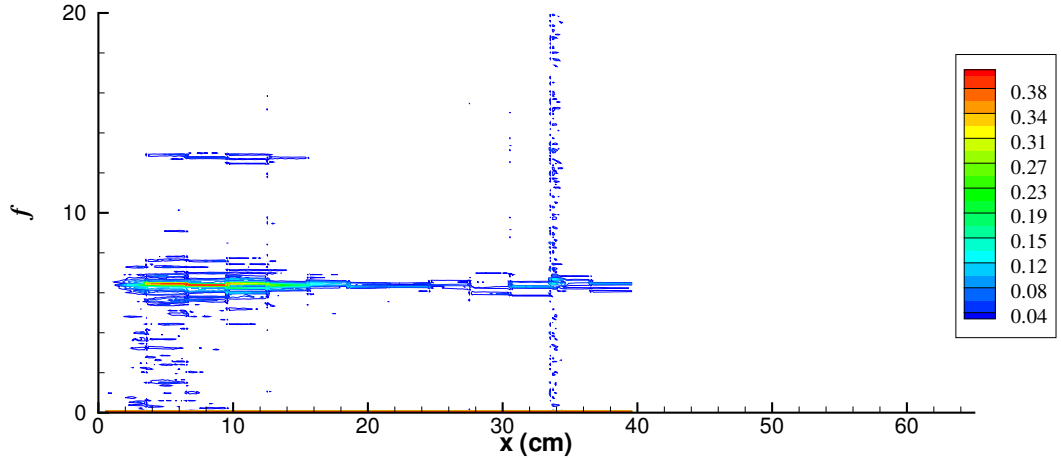

Figure 5.24: Frequency spectrum for the LIF measurements using series 1.1. f is in Hz. $F_T = 1.66$. and $T_\mathrm{d} = 2.16$ cm.

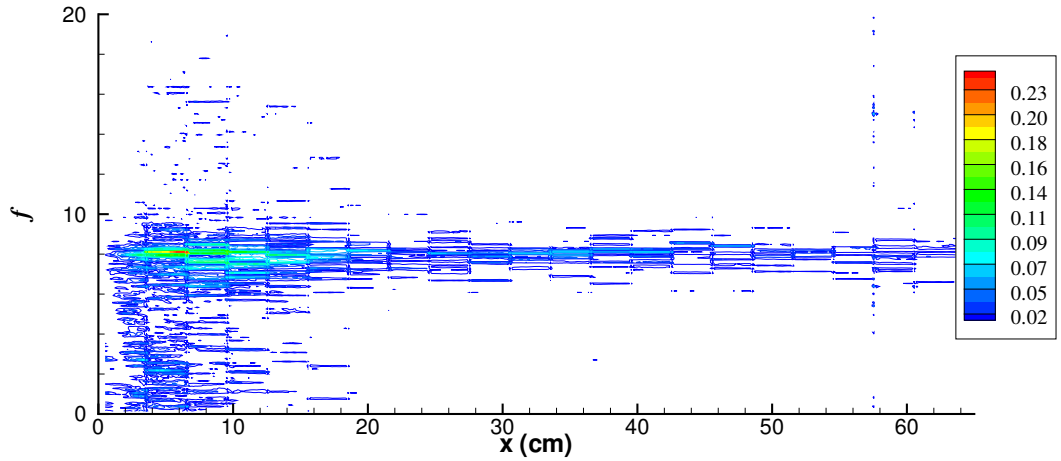

Figure 5.25: Frequency spectrum for the LIF measurements using series 1.1. f is in Hz. $F_T = 1.91$. and $T_{\mathrm{d}} = 1.89$ cm.

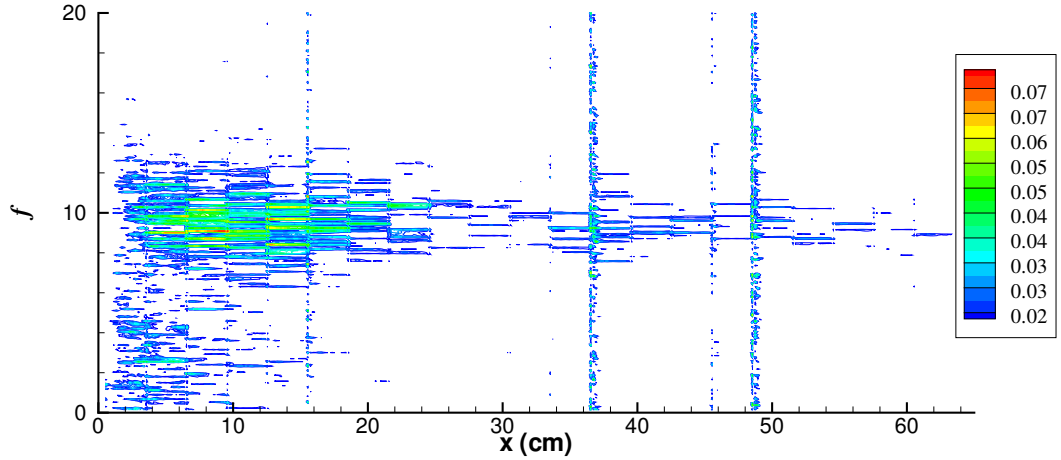

Figure 5.26: Frequency spectrum for the LIF measurements using series 1.1. f is in Hz. $F_T = 2.21$. and $T_{\mathrm{d}} = 1.60$ cm.

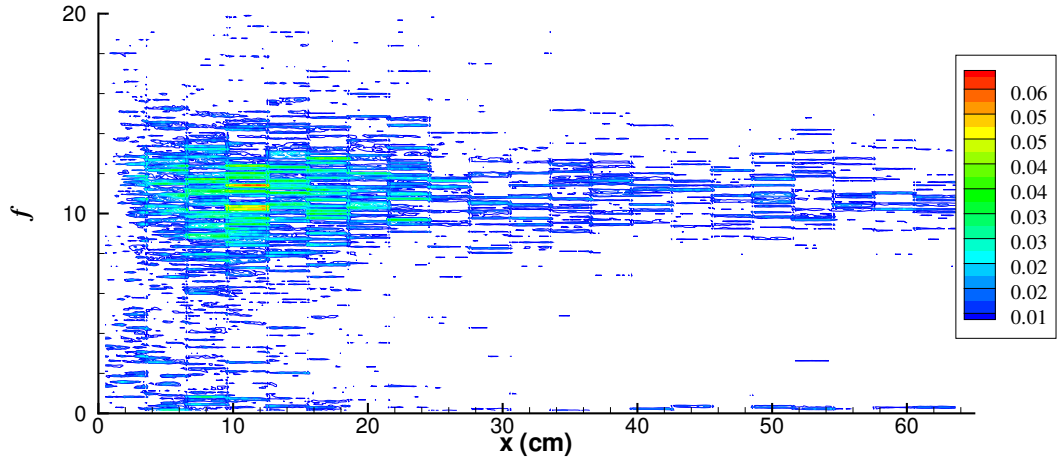

Figure 5.27: Frequency spectrum for the LIF measurements using series 1.1. f is in Hz. $F_T = 2.60$. and $T_\mathrm{d} = 1.30$ cm. Note the toe located 2cm < x < 10cm and $f < 1$ Hz.

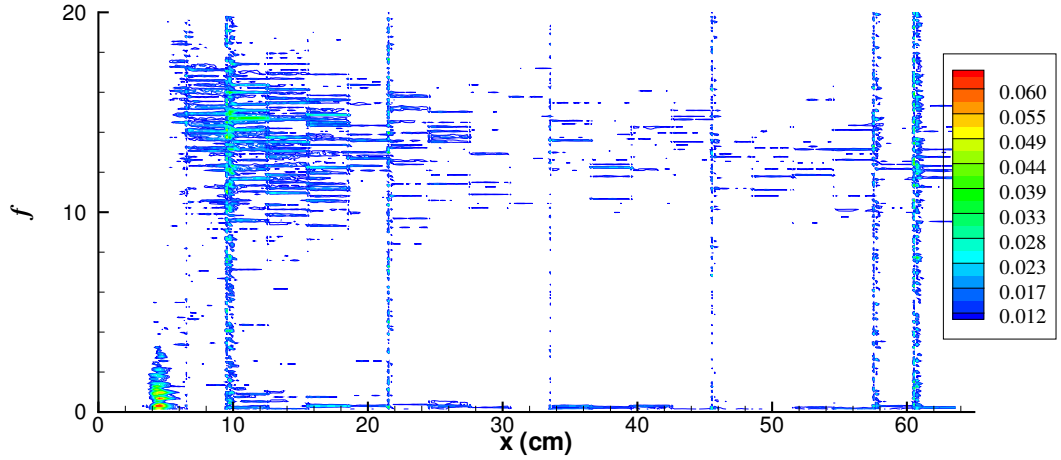

Figure 5.28: Frequency spectrum for the LIF measurements using series 1.1. f is in Hz. $F_T = 3.18$. and $T_\mathrm{d} = 0.98$ cm. Note the toe located 4cm < x < 6cm and $f < 4$ Hz.

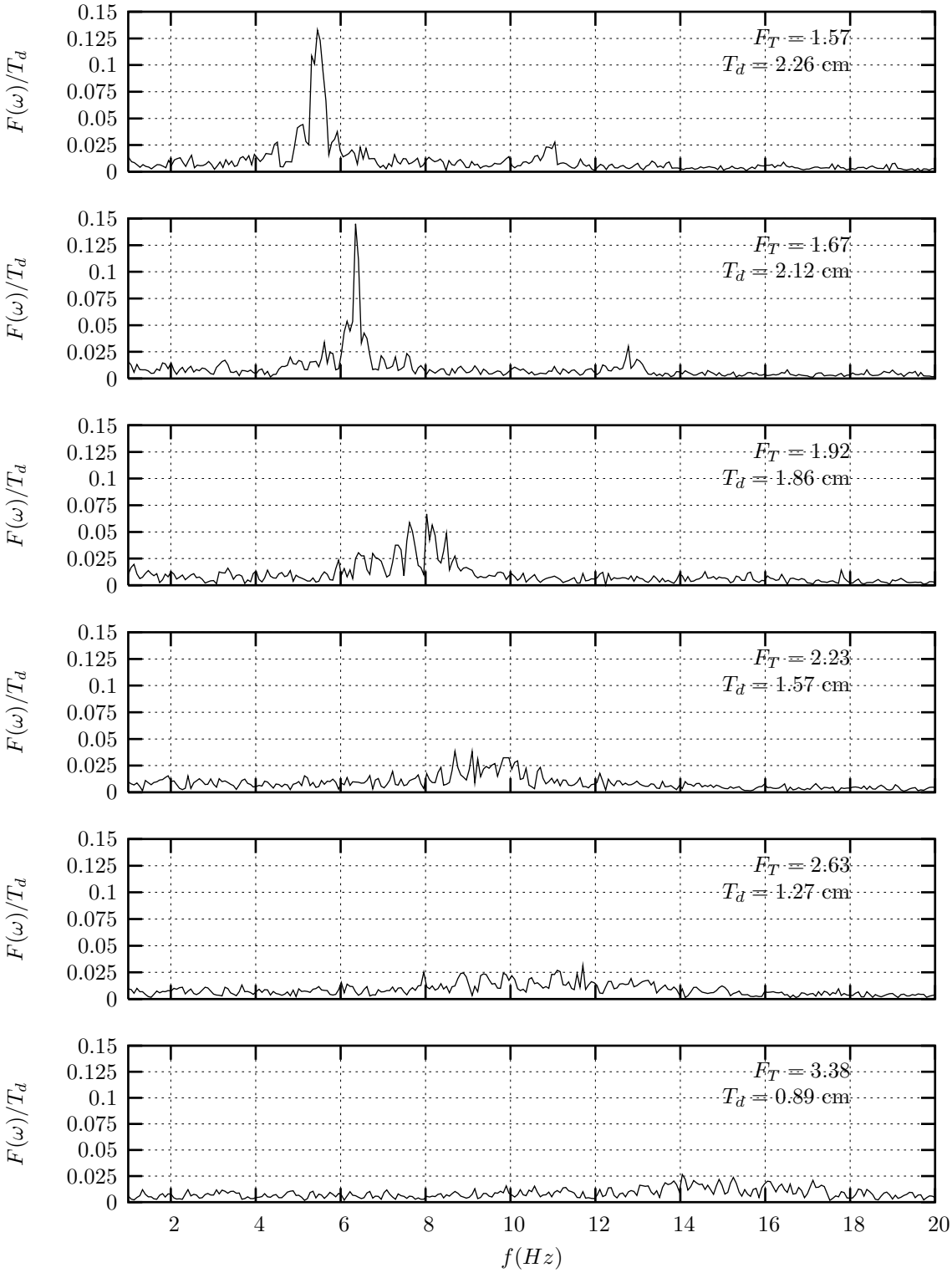

Figure 5.29: Frequency spectra at a position $x = 8$ cm, series 1.1.

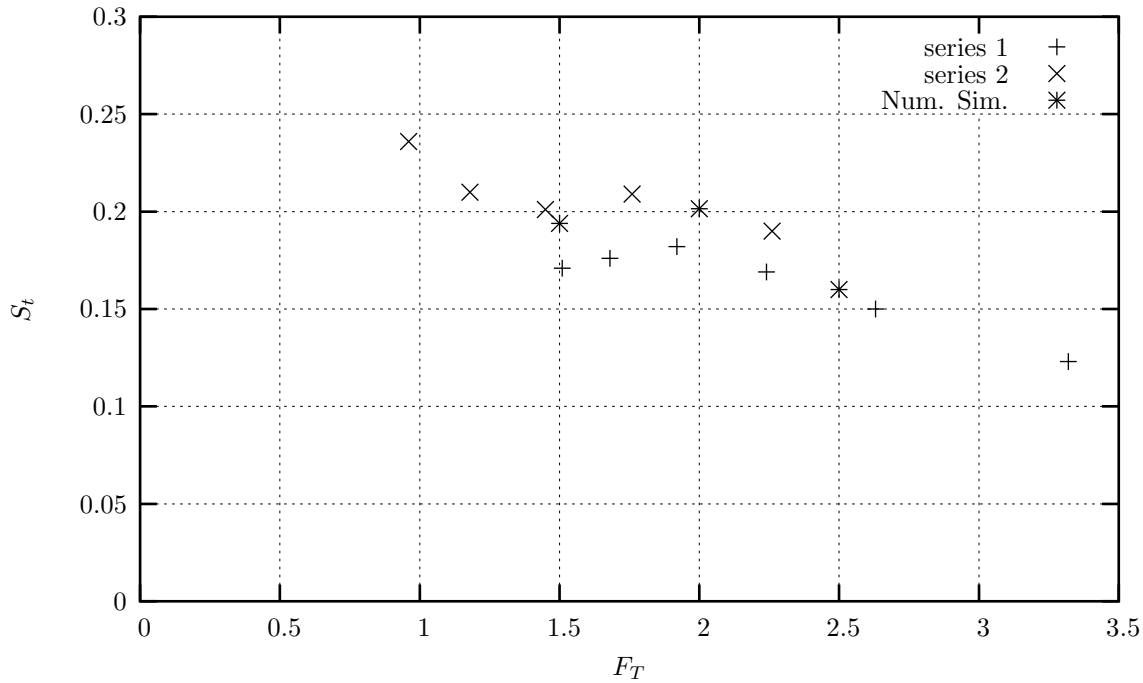

Figure 5.30: Strouhal number for each test condition in series 1.1, and 1.2 and from numerical simulations.

CHAPTER 6

CONCLUSIONS AND CONTRIBUTIONS

This thesis brings ship model experiments together with high-fidelity experimental and numerical simulation of a canonical problem to study one of the most difficult problems remaining in ship hydrodynamics, the flow behind a transom stern.

6.1 Qualitative Description

6.1.1 Four Flow Regimes

The experimental and numerical data-sets describe the backward-facing step with a free-surface in terms of four different flow regimes representing different characteristics of the free-surface behind the body. Non-intrusive free-surface measurements were used to determine the statistical and frequency properties for all four different flow regimes, which are described as follows:

1. Regime 1 is characterized by negligible free-surface fluctuations. In this regime there is a viscous shear layer at the keel-transom location that interacts minimally with the free-surface (r.m.s. of the free-surface is less than 10% of the transom draft).

2. Regime 2 spans a transom-draft Froude number range that begins when the turbulent shear layer originating at the keel creates free-surface fluctuations at

a Froude number of approximately 1. A coherent vortex street forms and the resulting large free-surface fluctuations (r.m.s. greater than 25 % of the transom draft) convect downstream and overturn (break) near the location of the first wave crest of the mean profile. As the Froude number increases, the coherency of the vortex street degrades as the mean free-surface moves downward on the body. The span of the regime ends when the transom becomes dry at the critical Froude number $F_c \approx 2.5$.

The frequency analysis in this regime identifies a dominant Strouhal number at a value of approximately 0.2. This is the shedding frequency of a blunt body in a homogeneous fluid and is confirmed by both experiment and numerical simulation.

3. Regime 3 exists after ventilation and is characterized by the rolling breaker on the first mean wave crest behind the body. The profile of the breaking wave is measured and the location of the toe with increasing Froude number documented.

   The Fourier analysis in the regime shows that the toe has low frequency oscillations as well as a wider band of energy that is centered at a Strouhal number of 0.15. Within the Froude number range measured in the present experiments, the Strouhal number of the dominant frequency decreases with increasing Froude number.

4. Regime 4 contains all Froude numbers after which the breaking roller is shed. This regime is not studied in detail in this thesis, however it is observed experimentally that the toe sheds at a Froude number of approximately 4.

6.1.2 Free-Surface Unsteadiness

The r.m.s. of the free-surface is used to quantify its unsteadiness and the maximum r.m.s. serves to identify the transition between flow regimes 1 and 2. Also, the maximum r.m.s. is useful to compare the numeric simulations with the experimental data. For Froude numbers in the range of 1.5 to 3.0, the two-dimensional simulations over predict the experimental values of maximum r.m.s. by a factor of two. Reasons contributing to the discrepancy may be several and are listed in order of decreasing importance.

1. The vortex street, which is visible in both numerical simulation and experiments, breaks down more rapidly in the three-dimensional experimental domain thus decreasing the r.m.s. in the experiments.

2. The numerical simulations may compare poorly due to inaccuracies in the turbulence modeling. The Spalart-Allmaras model treats the turbulence isotropically, but near the free-surface the turbulence is anisotropic. Future work is to investigate improvements to the transport equation of eddy-viscosity that would more accurately treat the turbulence near the free-surface.

3. A third reason that could contribute to the difference may be due to the omission of surface tension forces in the numerical simulations. It is interesting to note that the measured surface tension coefficient in the experimental facility corresponds to a value of maximum damping of free-surface waves.

6.2 Wave Profile Statistics

The mean free-surface profile characteristics from experiments and RANS simulations are compared to analytic and numeric inviscid theories. The most interesting

finding is the wave-length between the first and second wave-crests behind the body is greatly reduced when compared to the linear gravity wave-length. At low Froude numbers the length is 60% the linear length, and at higher Froude numbers the length approaches 90% the linear length. The agreement between the experimental and numerical data is excellent.

The reason for the reduced wave-length is the velocities in the wake are less than the free-stream velocity, so the free-surface wave is effectively propagating with a reduced speed and therefore reduced wavelength. A stream-function theory of Dalrymple (1974) that derives the dispersion relation for a water-wave traveling over a bi-linear shear current is used to examine the wave-length reduction due to vorticity in the layer of water near the free-surface. This theory is adapted to the backward-facing step with a free-surface by modeling the thickness of the vortical layer as twice the transom draft. Solutions for different values of non-dimensional free-surface velocity are plotted along with the present data, and a free-surface velocity that is 55% of the free-stream follows the experimental and numerical measurements well. The inviscid irrotational theory poorly predicts the wave-length near the body.

The present data for the wave steepness, which is a quantity calculated using the amplitude and length, follow the trends of the inviscid low and high-speed solutions. The experiments suffer from large relative uncertainty and are therefore somewhat scattered, but the numerical solutions precisely follow the low and high-speed inviscid behavior. The real fluid results differ from the ideal fluid predictions in that the second wave-crest has an amplitude that is less than that of the first crest. The reasons for this are that unsteady wave-breaking, viscosity and turbulence, and surface tension act on the real fluid consuming energy that would be radiated away from the body in the gravity wave. The smaller second wave amplitude is pronounced in the

numerical solutions for speeds when the transom is partial wetted. Experimentally, the second wave crest does not exist for pre-ventilation speeds.

6.3 Transom Un-wetting

The destroyer model experiments describe the pressure on a transom stern as well as show how a stern flap acts to decrease pressure drag. In examining the simultaneous pressure and free-surface measurements from the backward-facing step with a free-surface, it is shown that the pressure where the keel meets the transom is due to the height of water on the transom. Using this conclusion, the un-wetting process as determined by hull pressure on the destroyer model is described in comparison with the BFSFS and a regression equation from Doctors (2003). The value for the critical Froude number from the BFSFS is $F_c = 2.5$ which is close to the value from the regression equation of $F_c = 2.55$. Both the model experiments on a ship-body used in the regression analysis and the two-dimensional BFSFS where conducted at a length Reynolds number of $Re_L \approx 10^6$. The pressure measurements on the destroyer model conclude a critical Froude number of $F_c \approx 3.0$ and where conducted at a Reynolds number $Re_L \approx 10^7$. The larger Reynolds number of the destroyer tests may explain the difference in the critical Froude number, but it is impossible to determine conclusively from the present data. The agreement in the behavior of un-wetting between the BFSFS experimental and numerical simulations with the regression equation of Doctors (2003) show that the infinite beam canonical problem represents the hydrodynamics of a transom stern.

6.4 Relevance to the Naval Architect

This thesis contains a benchmarking data-set for Naval Architects performing numerical simulations on transom stern vessels, and provides advice for those who

are designing a stern flap for resistance reduction.

Presently, state of the art unsteady RANS simulations are being performed on model-scale marine vessels with a transom stern. The data presented in this thesis documents the process of transom un-wetting with a non-intrusive free-surface measurement technique. Also the information on the unsteadiness, both statistical and spectral, is useful for unsteady code validation.

The Naval Architect using potential flow techniques now has a new data point in the debate on the value of the critical Froude number. The result from this work is in close agreement with other model tests on ship type bodies (Doctors 2003) yielding a value of approximately $F_c \approx 2.5$. Additionally the present study is conducted on a body of infinite beam-to-draft ratio, and agree with the data of Doctors (2003) where the beam-to-draft ratio was as small as 1.0. This demonstrates that beam-to-draft ratio has little effect on the critical Froude number in the range $1.0 < B/T < \infty$.

Stern flaps are a commonly used appendage in the modern day marine world. Pressure measurements on the destroyer hull with and without a stern flap show that resistance is altered because the flap increases the pressure near end of the body. Vessels that have a buttock angle such that the local draft of the body decreases moving in the aft direction are suited to benefit from a stern flap because the increase in pressure provides a thrust on the body.

Conversely, vessels with a stern geometry where the local draft increases moving in the aft direction will receive a resistance increase from a flap. It is noted that often vessels with this geometry could benefit from an alteration in the running trim due to the flap, which alters the global pressure on the hull therefore reducing resistance.

APPENDICIES

APPENDIX A

ERROR ANALYSIS

Experimental error assessment follows the methodolgy described in Coleman and Steele Jr. (1989). In this appendix, the sources of error will be identified, and then their influence propogated through the final results. The uncertainty will be represented as E_x, where the subscript x is the measured variable. Table A.1 contains a summary of the uncertainties for the different measurements reported in this thesis.

A.1 Destroyer Hull Pressure Measurements

In chapter 2, transducers are used to measure the pressure on the hull of a ship model. These transducers are designed to measure gaseous media, and when implemented for experiments in this thesis, an interface was always present somewhere in the set-up. From experience of using these sensors, the unpredictibility of the interface was the most dominant source of uncertainty. A great amount of time was spent bench calibrating the sensors. The calibration aimed at determining the frequency response of the transducer as it is used in the present set-up. The results of the bench calibration dictate that processes occurring the at frequencies less than 10 Hz can be measured to within one-tenth of an inch of water, or $E_p = 2.54$ mm H_2O. In hindsight, a more careful precision index could be sought by repeating a single measurement many times, but at the time of the experiments this methodolgy was

not followed.

A.2 Backward-Facing-Step with a Free-Surface Experiments

In chapter 5, the experiments in the recirculating water channel use the same transducers to measure pressure, and then to calculate velocity. For these measurements, a special apparatus was built (ref. section 3.3.2). The new apparatus reduces the influence of the air-water interface in the system, and repeatibility yields measurements with confidence of $E_p = 0.355$ mm H_2O.

All linear dimensions reported that are associated with position controlled by the tranverse on the recirculating water-channel have an error due to the resolution of the stepper motors, $E_{x,z} = 2 \times 10^{-}5$ m. The frequency controller for the impeller drive motor has a resolution of 0.1 Hz.

The calm water depth was measured using a hook-gauge placed near the transom of the model. The gauge had a dial indicator with graduations of 0.0254 mm. Repeatibility tests were performed and the precision of the measurement was 0.254 mm. The limiting source of error in the calm-water depth were the leaks in the tank. A great deal of effort was spent to control the leaks, and the final system which compensated for the leaks was able to control the change in water depth over the time interval of any given test to 1 mm.

Three different techniques were used to measure the unsteady free-surface. The LIF technique resolves the free-surface to within three pixels. This distance represents the width of the transition in intensity in the imaged interface. The wire-capacitance probe was calibrated to within an uncertainty of 0.33 mm, but its self-disturbance was witnessed at a value of approximately 2 mm. The sonic probe was calibrated on a quiescent free-surface to a value of 0.813 mm.

A.2.1 Regression Uncertainty

Two regression fits were used in the BFSFS experiments. The free-surface drop in the test section and the mean vertically averaged velocity were regressed against the frequency of the impeller motor. The standard error of estimate is defined as in Coleman and Steele Jr. (1989) as,

$$\mathrm{SEE} = \left\{ \frac{\sum_{\mathrm{i}=1}^{\mathrm{N}} \left[\mathrm{Y_i} - (\mathrm{aX_i} + \mathrm{b})\right]^2}{\mathrm{N} - 2} \right\}^{\frac{1}{2}} \tag{A.1}$$

In the case of the second order regression for the free-surface drop, the above formula is modified by including the quadratic term in the numerator and the denominator becomes $N - 3$. The two equations and their respective SEE values are reported below,

$$h_1(m) = -5.542 \times 10^{-5}(\mathrm{Fq})^2 - 2.723 \times 10^{-4}\mathrm{Fq} + 1.143 \times 10^{-3} \pm 3.37 \times 10^{-4} \tag{A.2}$$

$$U(m/s) = 0.0455\mathrm{Fq} - 0.0258 \pm 0.00713 \tag{A.3}$$

A.3 Propagation of Error into the Experimental Result

To propagate uncertainty into an calculated result, the following equation was used,

$$\left(\frac{E_r}{r}\right)^2 = \left(\frac{1}{r}\frac{\partial r}{\partial X_1}E_{X_1}\right)^2 + \left(\frac{1}{r}\frac{\partial r}{\partial X_2}E_{X_2}\right)^2 + ... \tag{A.4}$$

where X_i are the various measured quantities used to calculate the final result r.

Table A.1: Measurement Variable Uncertainties.

Variable		Value	Description	Source
E_p	=	2.54 mm H_20	pressure-chap. 2	air-water interface
E_p	=	0.355 mm H_2O	pressure-special apparatus	calibration
$E_{x,z}$	=	$2{\times}10^{-5}$ m	position of the traverse	resolution of the stepper motors
E_{Fq}	=	0.1 Hz.	frequency of the impeller	resolution of the display
E_{T_o}	=	1 mm	calm-water depth	tank leak
$E_{\delta h}$	=	3.37×10^{-4}m	reference free-surface position	regression
E_U	=	0.00713 m/s	free-stream velocity	regression
$E_{\zeta,\mathrm{LIF}}$	=	3 pixels	free-surface LIF technique	width of the interface in each image
$E_{\zeta,\mathrm{cap}}$	=	2 mm	free-surface capacitance probe	self-disturbance of the wire
$E_{\zeta,\mathrm{sonic}}$	=	0.813 mm	free-surface sonic probe	calibration on a calm free-surface

APPENDIX B

EXPERIMENTAL AND NUMERICAL RESULTS

This appendix catalogs the experimental and numerical results for the backward-facing step with a free-surface. The experimental results are organized into two series. The first contains the free-surface elevation measurements taken using LIF, wire-wave, andsonic probe techniques and describe the wave profiles behind the step. This series is broken into two sub-series, 1.1 and 1.2, which each represent a different model set-up with the zero-speed transom draft of 4.2 and 6.35 cm respectively.

The second series is comprised of free-surface elevations taken with the LIF technique and pressure measurements near the body to explore the process of un-wetting. The results from this series are numbered 2.1-2.5.

Numerical simulations are conducted for Froude numbers of 1.5, 2.0, 2.5, 3.0, and 3.5 at a transom draft Reynolds number of 4.0×10^4.

The free-surface profiles are measured with the wire capacitance probe for low speeds ($F_T < 1$), the LIF technique for speeds corresponding to intermediate Froude numbers ($1 < F_T < 3$), and the sonic wave probe is used for the speeds after ventilation ($F_T > 2.5$). The model calm-water zero-speed draft was set to the predetermined value for each sub-series (4.2 or 6.35 cm), and then the tests were conducted at a succession of increasing speeds. Table B.1 summarizes the test conditions. As

previously defined, the transom draft is denoted as T_{d}, the transom draft Froude number is $F_T = U/\sqrt{gT_{\mathrm{d}}}$, and then the Reynolds number based on transom draft is $Re_T = UT_{\mathrm{d}}/\nu$.

The LIF measurements were conducted with the camera focused on a small portion of the free-surface of interest. To facilitate the measurement of a full free-surface profile, the camera and final stage of laser optics were moved in unison and positioned at a sequence of downstream locations. For series 1.1, this corresponds to moving in 3 cm streamwise increments, using a zoom on the camera lens yielding a scale factor of 99 pixels/cm in the image plane. The camera and optics were moved in increments of 3.93 cm for series 1.2, with a camera lens zoom corresponding to 78 pixels/cm. The number of positions varied based on the model draft, and Froude number. For the low speeds that were rather mundane, the number of downstream positions were reduced. For the larger-draft-model series 1.2, the number of positions was limited to the length of the traversing system ($\sim$ 0.8m).

At each location a set of 800 images was collected at a frequency of 60 Hz. The statistics of the instantaneous free-surface profileswere used to calculate the mean $\bar{\eta}(x)$, and standard deviation $\sigma(x)$ at each downstream pixel column. The standard deviation here is defined as

$$\mathrm{r.m.s.(x)} = \sigma(\mathrm{x}) = \left[\frac{1}{\mathrm{N}}\sum_{\mathrm{i-1}}^{\mathrm{N}}\left(\zeta_{\mathrm{i}} - \bar{\zeta}\right)^2\right]^{\frac{1}{2}} \tag{B.1}$$

The means and standard deviations converge after approximately 200 images; for the results presented herein, all 800 images were used.

Table B.1: Test matrix. Re_L is the Reynolds number calculated with the model length of 1.79 m. λ_{lin} is the linear theory gravity wavelength calculated as $\lambda_{\text{lin}} = 2\pi U^2/g$.

	Freq (Hz)	Tech.	T_{d} (cm)	U (m/s)	F_T	Re_T	Re_L	λ_{lin} (cm)
	16.2	LIF	2.26	0.71	1.57	1.49×10^4	1.18×10^6	32.4
	17.4	LIF	2.13	0.77	1.67	1.44×10^4	1.22×10^6	37.6
Series 1.1	18.6	LIF	1.86	0.82	1.92	1.36×10^4	1.31×10^6	43.1
$T_{\text{o}} = 4.2$ cm	19.8	LIF	1.57	0.88	2.23	1.23×10^4	1.40×10^6	49.0
	21.0	LIF	1.27	0.93	2.63	1.05×10^4	1.49×10^6	55.4
	22.4	LIF	0.89	0.99	3.35	0.79×10^4	1.59×10^6	63.2
	7.5	wire	5.72	0.32	0.42	1.68×10^3	5.63×10^5	6.37
	10.0	wire	5.61	0.43	0.58	2.17×10^3	7.66×10^5	11.8
	12.5	wire	5.28	0.54	0.75	2.56×10^3	9.70×10^5	18.9
	15.0	wire	4.83	0.66	0.95	2.83×10^3	1.17×10^6	27.6
	15.0	LIF	4.83	0.66	0.95	2.83×10^4	1.05×10^6	27.6
	17.5	LIF	4.32	0.77	1.18	2.69×10^4	1.23×10^6	38.0
	20.0	LIF	3.75	0.88	1.46	2.96×10^4	1.41×10^6	50.1
	22.5	LIF	3.30	1.00	1.75	2.94×10^4	1.59×10^6	63.8
Series 1.2	25.0	LIF	2.45	1.11	2.27	2.42×10^4	1.78×10^6	79.2
$T_{\text{o}} = 6.35$ cm	25.5	LIF	2.22	1.13	2.43	2.24×10^4	1.81×10^6	82.4
	26.0	LIF	2.11	1.16	2.54	2.18×10^4	1.85×10^6	85.8
	26.5	LIF	2.00	1.18	2.66	2.11×10^4	1.89×10^6	89.2
	27.0	LIF	1.89	1.20	2.79	2.03×10^4	1.92×10^6	92.6
	27.5	LIF	1.79	1.23	2.98	1.89×10^4	1.96×10^6	96.2
	27.5	sonic	1.52	1.23	3.17	1.67×10^4	1.96×10^6	96.2
	28.0	sonic	1.36	1.25	3.42	1.51×10^4	1.99×10^6	99.8
	28.5	sonic	1.19	1.27	3.72	1.34×10^4	2.03×10^6	103.5
			T_{d}	U	F_T	Re_T		
			0.444	1.0	1.5	4.0×10^4		
Numerical			0.250	1.0	2.0	4.0×10^4		
Simulations			0.160	1.0	2.5	4.0×10^4		
			0.111	1.0	3.0	4.0×10^4		
			0.111	1.0	3.5	4.0×10^4		

Free-Surface Measurements LASER INDUCED FLUORESCENCE

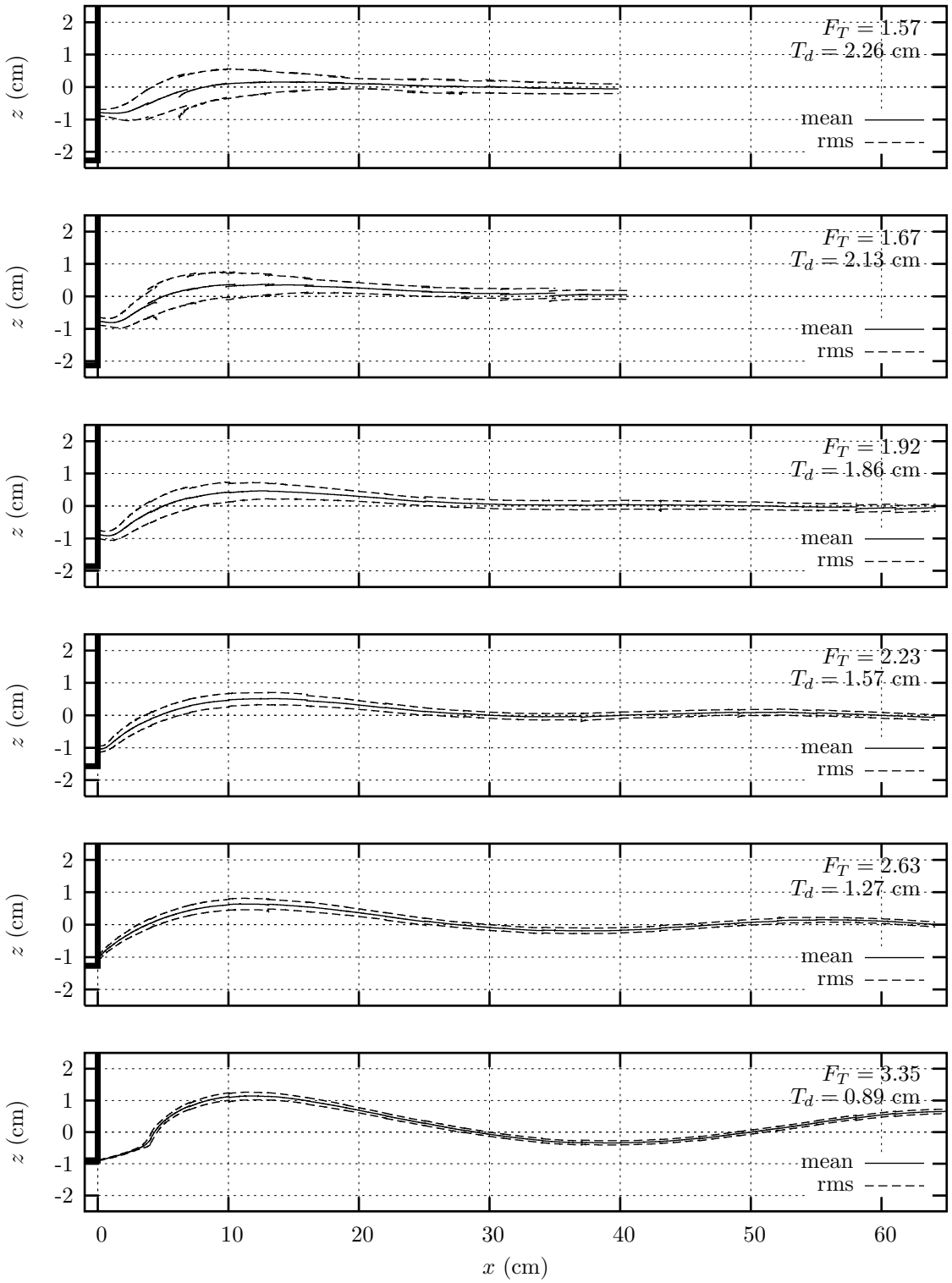

Figure B.1: Mean free-surface elevation from series 1.1 measured with the LIF technique. The dashed line represents +/- 1 standard deviation. The body is visible on the left of each diagram.

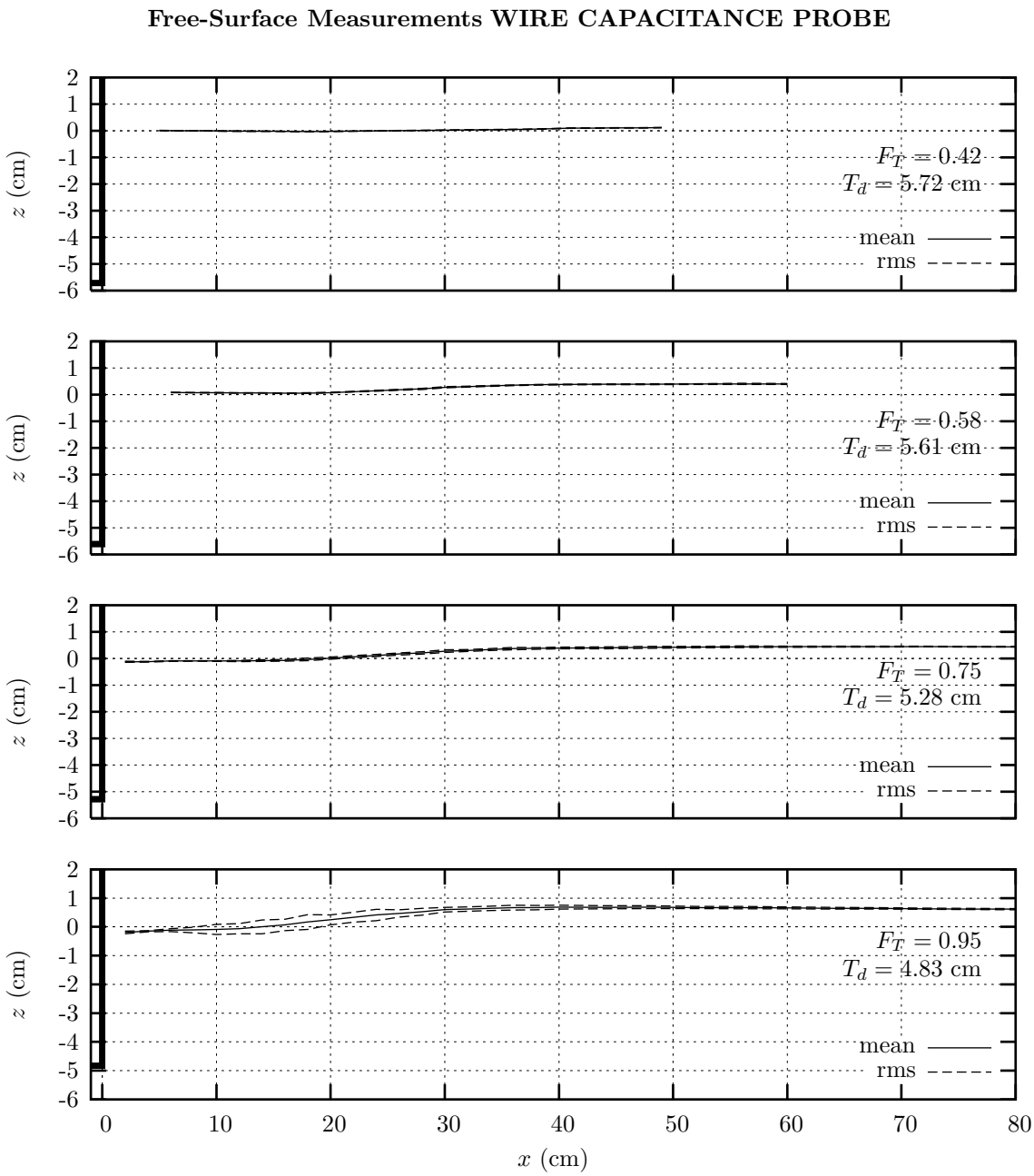

Figure B.2: Mean free-surface elevation from series 1.2, free-surface elevation is measured with a wire-capacitance wave probe. The dashed line represent +/- 1 standard deviation in the elevation.

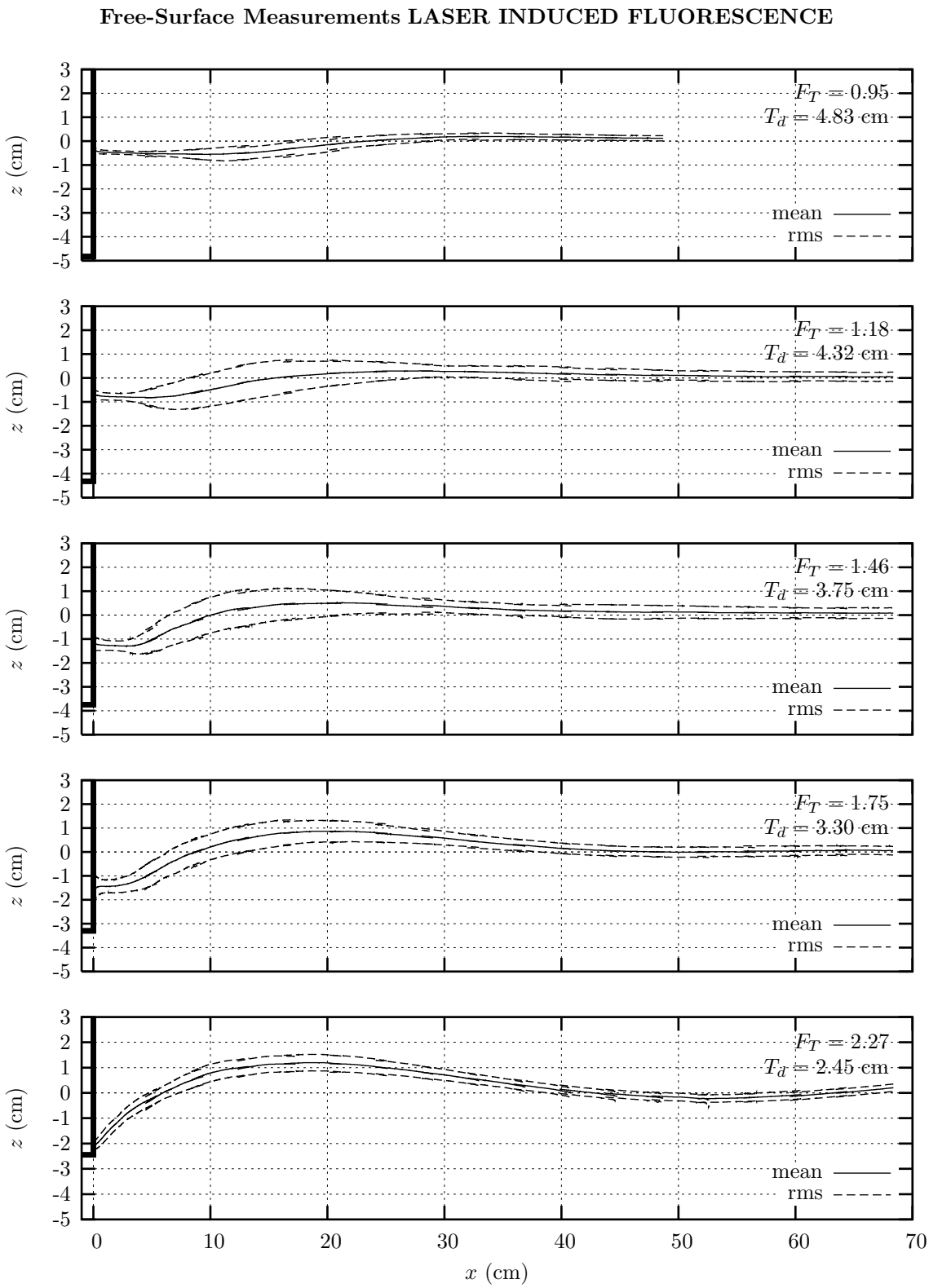

Figure B.3: Mean free-surface elevation from series 1.2 measured with the LIF technique. The dashed line represents +/- 1 standard deviation.

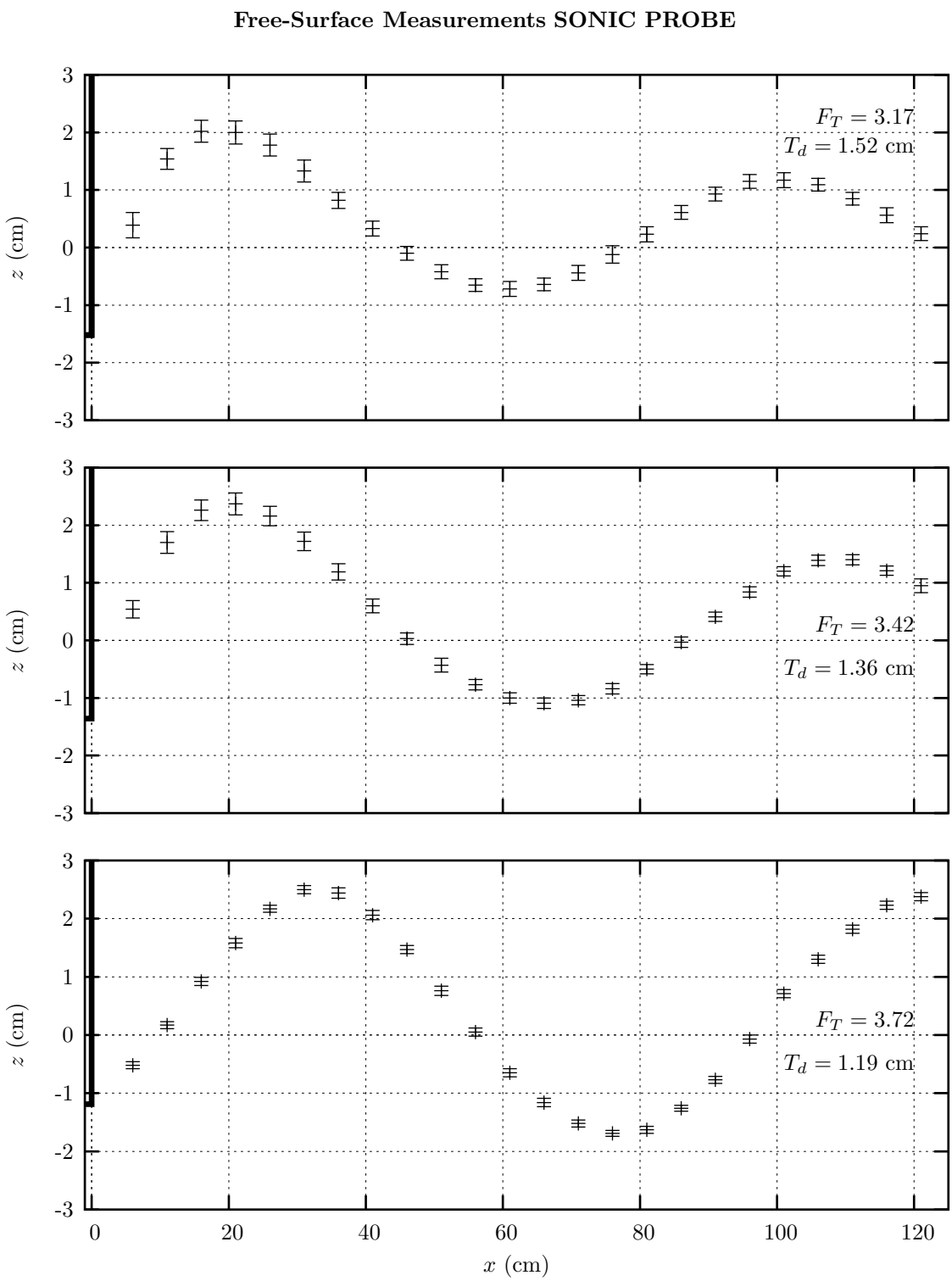

Figure B.4: Mean free-surface elevation from series 1.2, free-surface elevation is measured with a sonic wave probe. The error bars represent +/- 1 standard deviation in the elevation.

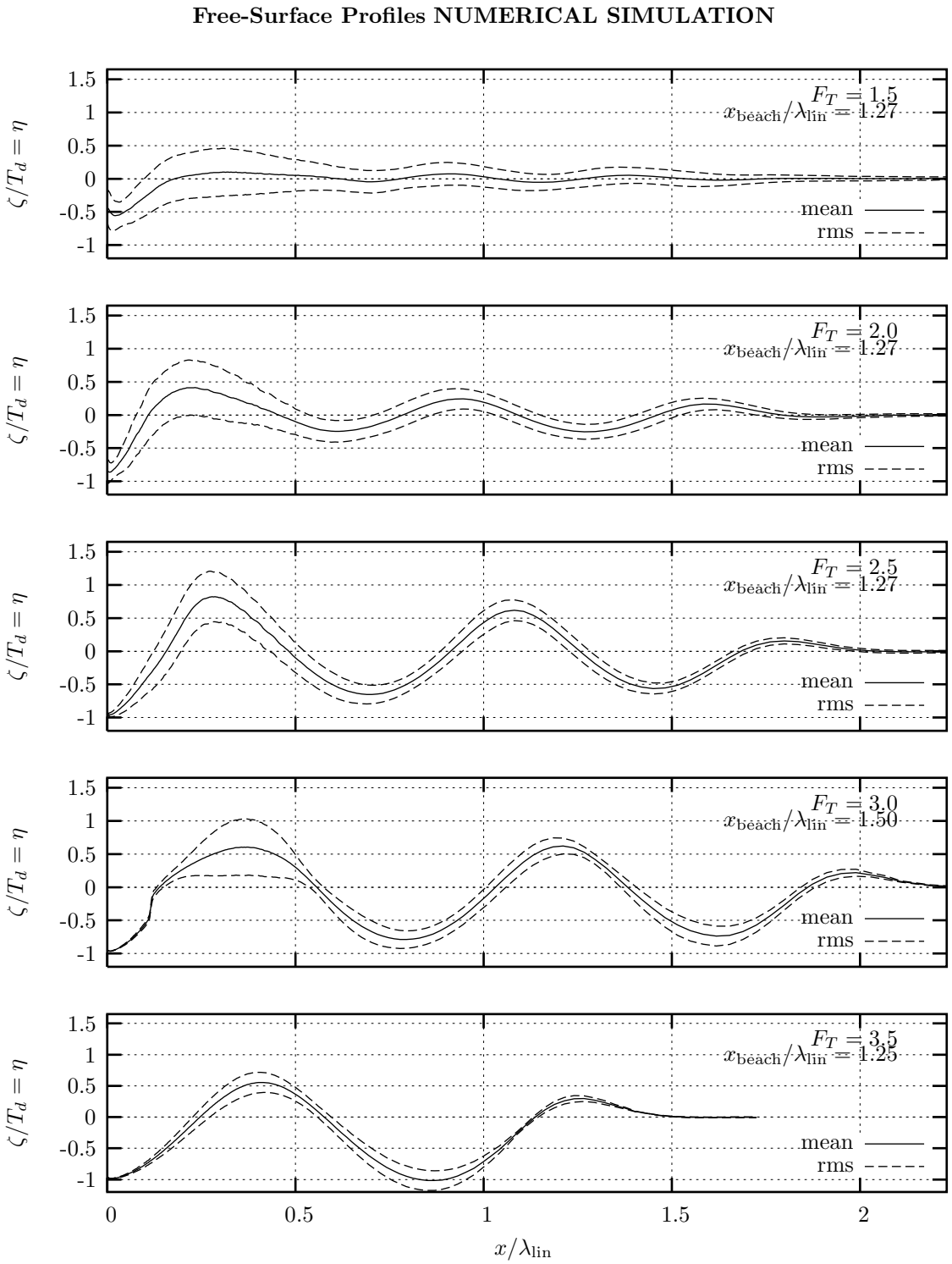

Figure B.5: Mean free-surface elevation from numerical simulations. Note that both axis are presented non-dimensionally, as opposed to dimensionally in the experimental results.

Free-Surface R.M.S. Measurements LASER INDUCED FLUORESCENCE

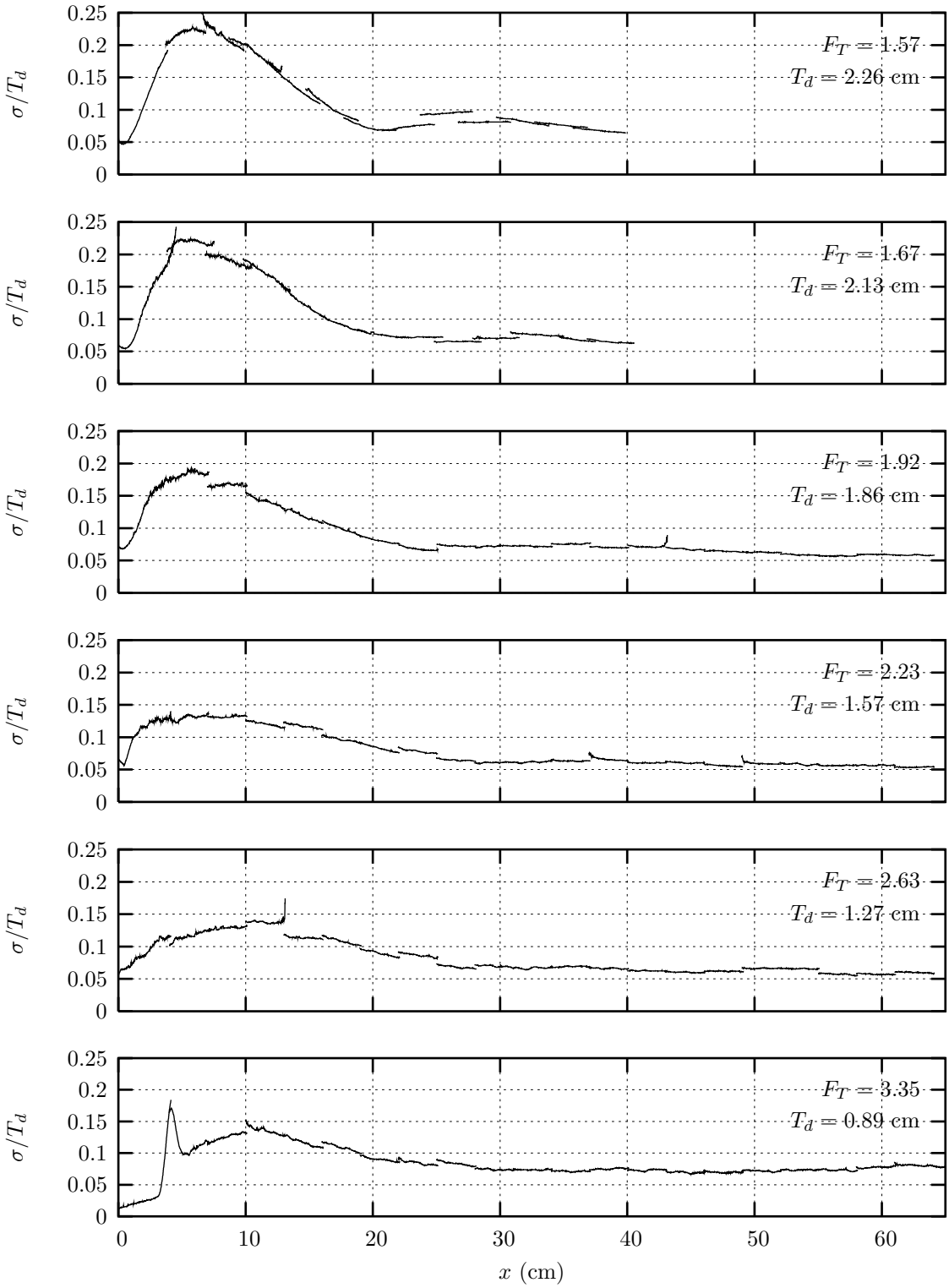

Figure B.6: Root mean square fluctuation of the free-surface for series 1.1 measured with the LIF technique.

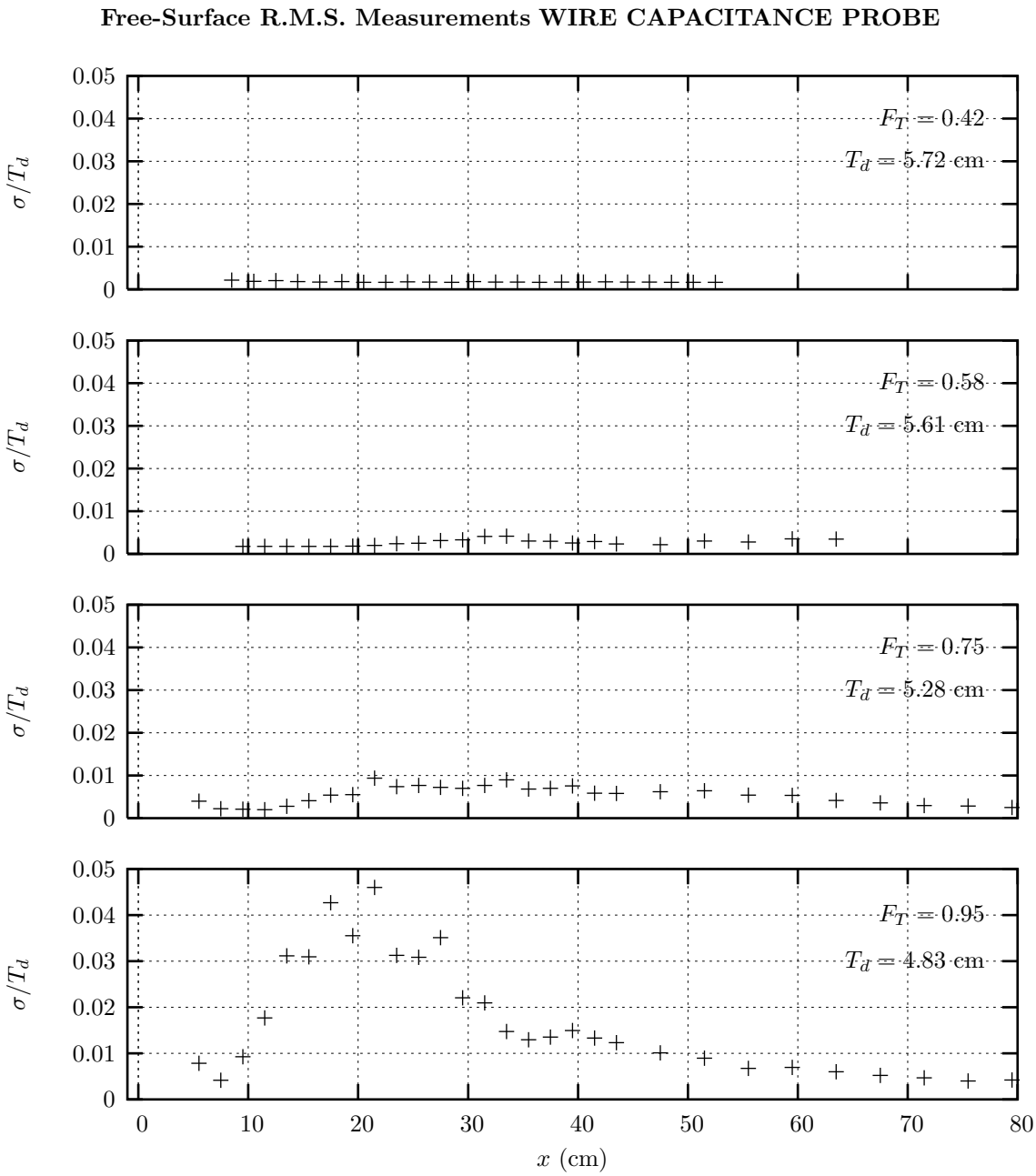

Figure B.7: Root mean square fluctuation of the free-surface for series 1.2, measured with a wire capacitance probe.

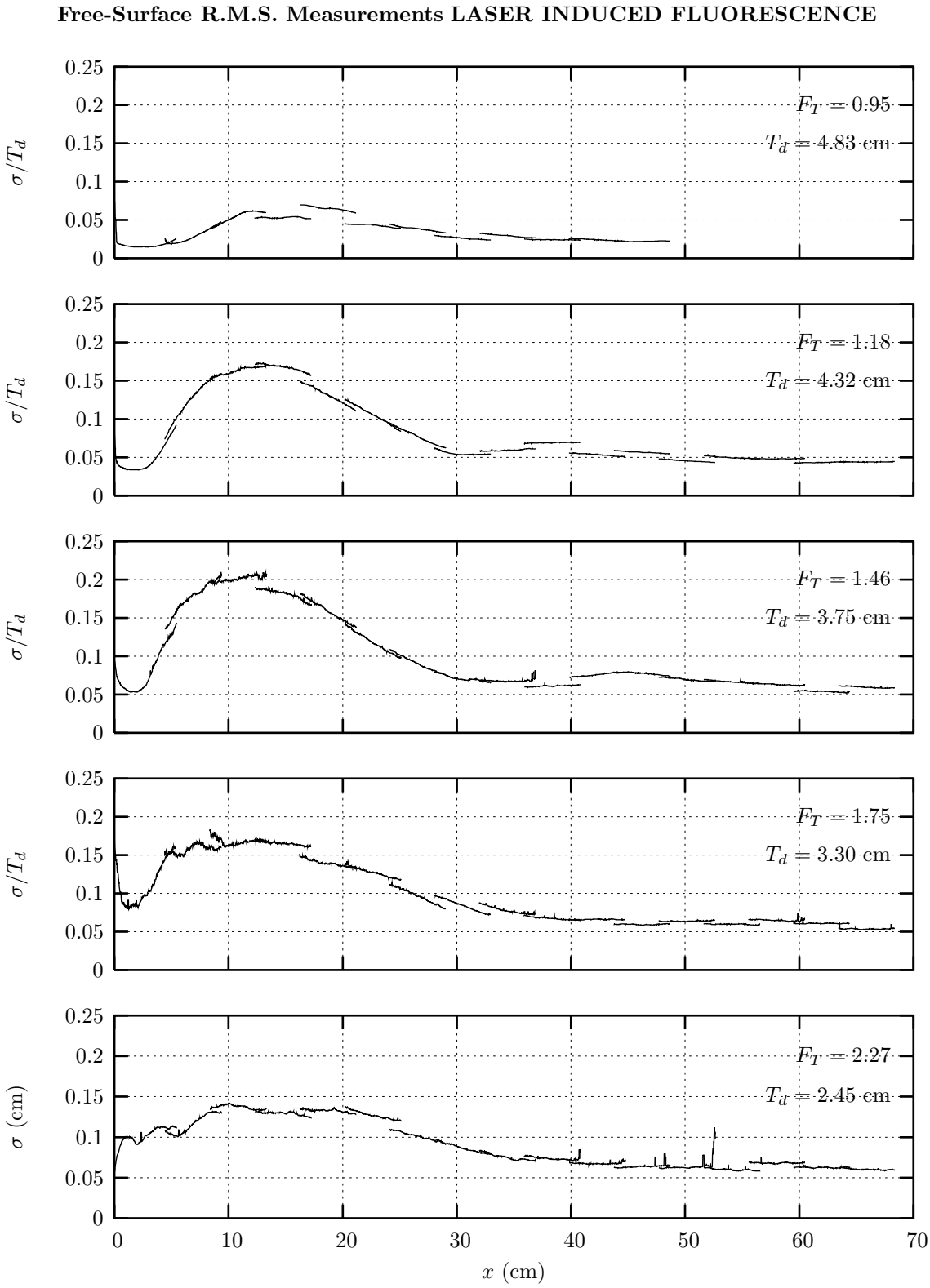

Figure B.8: Root mean square fluctuation of the free surface for series 1.2 measured with the LIF technique.

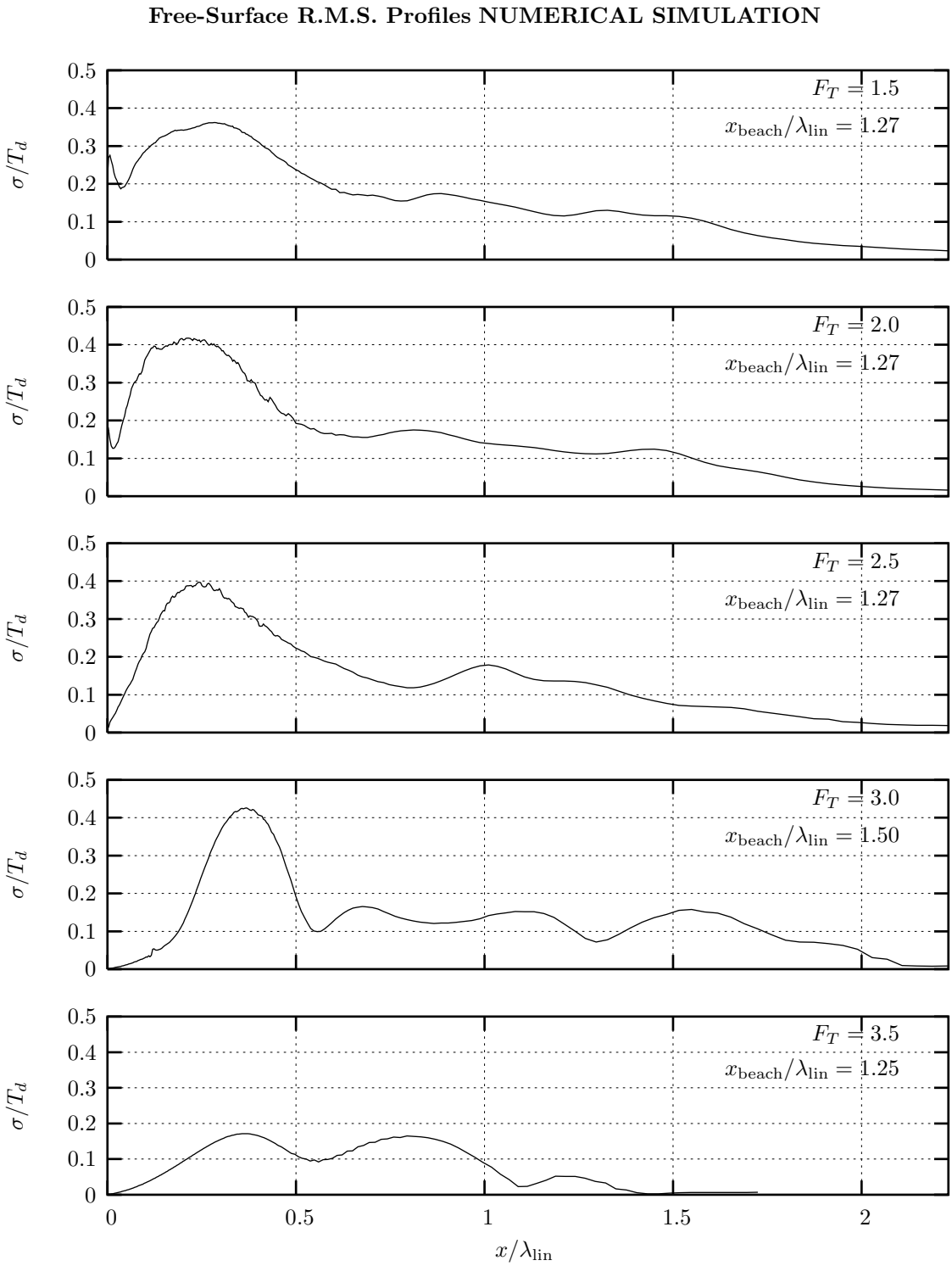

Figure B.9: Root mean square fluctuation of the free-surface from numerical simulations.

BIBLIOGRAPHY

Cheng, B. H. (1989). Computations of 3d transom stern flows. In *Fifth International Conference on Numerical Ship Hydrodynamics*, Washington, D.C., pp. 581–591.

Coleman, H. and W. G. Steele Jr. (1989). *Experimentation and Uncertainty Analysis for Engineers*. John Wiley & Sons.

Couser, P., J. F. Wellicome, and A. F. Molland (1998). An improved method for the theoretical prediction of the wave resistance of transom-stern hulls using a slender body approach. *International Shipbuilding Progress 45*(444), 331–349.

Cusanelli, D. (1998, June). Ship/model correlation of powering performance, pre and post stern flap installation trials on A. W. Radford (DD 968). Technical report, David Taylor Model Basin, Carderock Division, Naval Surface Warfare Center.

Cusanelli, D., P. A. Chang III, and S. McGuigan (1995, December). Stern flaps energy savings potential and effects on transom wave system for CG-47 class cruisers and DD-963 class destroyers (Model 5359). Technical report, David Taylor Model Basin, Carderock Division, Naval Surface Warfare Center.

Dalrymple, R. (1974). Water waves on a bilinear shear current. In *Conference of Coastal Engineering*, pp. 626–641.

Doctors, L. J. (1999, August-September). On the great trimaran-catamaran debate. In *Fifth International Conference on Fast Sea Transportation (FAST '99)*, Seattle, Washington.

Doctors, L. J. (2003, May). Hydrodynamics of the flow behind a transom stern. In *Twenty-Ninth Isreal Conference on Mechanical Engineering*, Haifa, Isreal.

Doctors, L. J. and A. H. Day (1997, July). Resistance prediction for transom-stern vessels. In *Fourth International Conference on Fast Sea Transportation (FAST '97)*, Sydney, Australia.

Doctors, L. J. and A. H. Day (2000, September). Steady-state hydrodynamics of high-speed vessels with a transom stern. In *Twenty-Third Symposium on Naval Hydrodynamics*, Val de Reuil, France.

Duncan, J. A. (1983a). The breaking and non-breaking wave resistance of a two-dimensional hydrofoil. *Journal of Fluid Mechanics 126*, 507–520.

Duncan, J. A. (1983b). A note on the evaluation of the wave resistance of two-dimensional bodies from measurements of the downstream wave profile. *Journal of Ship Research 27*(2), 90–92.

Hundrey, L. and G. Brodie (1998, March). Stern flap evaluation on USS Arthur W Radford (DD 968). Technical report, Carderock Division, Naval Surface Warfare Center.

Iafrati, A., A. D. Mascio, and E. F. Campana (2001). A level set technique applied to unsteady free surface flows. *International Journal of Numerical Methods in Fluids 35*, 281–297.

Karafiath, G. and S. Fisher (1987, May). The effect of stern wedges on ship powering performance. *Naval Engineers Journal 99*(3), 27–38.

Lapham, G., D. Dowling, and W. W. Schultz (1999). In situ force-balance tensiometry. *Experiments in Fluids 27*, 157–166.

Lapham, G., D. Dowling, and W. W. Schultz (2001). Linear and nonlinear gravity-capillary water waves with a soluble surfactant. *Experiments in Fluids 30*, 448–457.

Larsson, L., F. Stern, and V. Betram (2003). Benchmarking of computational fluid dynamics for ship flows: The Gothenburg 2000 Workshop. *Journal of Ship Research 47*(1), 63–81.

Le, H. and P. Moin (1991). An improvement of fractional step methods to the incompressible Navier-Stokes equations. *Journal of Computational Physics 92*, 369–379.

Le, H. and P. Moin (1994). Direct numerical simulation of turbulent flow over a backward facing step. Technical Report TF-58, Department of Mechanical Engineering, Stanford University.

Maki, K. J., L. J. Doctors, R. F. Beck, and A. W. Troesch (2005, June). Transom-stern flow for high-speed craft. In *Eighth International Conference on Fast Sea Transportation (FAST '05)*, St. Petersburg, Russia.

Milgram, J. H. (1969, March). The effect of a wake on the wave resistance of a ship. *Journal of Ship Research*, 69–71.

Oving, A. (1985, September). Resistance prediction method for semi-planing catamarans with symmetrical demihulls. Technical report, Maritime Research Institute Netherlands (MARIN), Wageningen.

Preston, J. H. (1972). The measurement of pressure in low velocity water flows. *Journal of Physics E: Scientific Instruments 5*, 277–282.

Reed, A., J. Telste, and C. Scragg (1991, August). Analysis of transom stern flows. In *Eighteenth Symposium on Naval Hydrodynamics*, Ann Arbor, Michigan, pp. 207–219.

Rosendfeld, M., D. Kwak, and M. Vinokur (1991). A fractional step method to the unsteady incompressible Navier-Stokes equations in generalized coordinate systems. *Journal of Computational Physics 94*, 102–137.

Saunders, H. (Ed.) (1957). *Hydrodynamics in Ship Design*, Volume 2, pp. 529–531. Society of Naval Architects and Marine Engineers.

Scorpio, S. (1997). *Fully nonlinear ship-wave computations using a multipole, accelerated, desingularized method*. Ph. D. thesis, University of Michigan.

Spalart, P. R. and S. R. Allmaras (1994). A one-equation turbulence model for aerodynamic flows. *La Recherche-Aérospatiale* (1).

Sussman, M. and E. Fatemi (1999). An efficient, interface-preserving level set redistancing algorithm and its application to interfacial incompressible fluid flow. *SIAM Journal of Scientific Computing 20*(4), 1165–1191.

Sussman, M. and E. G. Puckett (2000). A coupled level set and volume-of-fluid method for computing 3d and axisymmetric incompressible two-phase flows. *Journal of Computational Physics 162*, 301–337.

Sussman, M., P. Smereka, and S. Osher (1994). A level set approach for computing solutions to incompressible two-phase flow. *Journal of Computational Physics 114*, 146–159.

Telste, J. and A. M. Reed (1993, August). Calculation of transom stern flows. In *Sixth International Conference on Numerical Ship Hydrodynamics*, Iowa City, Iowa, pp. 79–92.

Tulin, M. P. and C. C. Hsu (1986). Theory of high-speed displacement ships with transom sterns. *Journal of Ship Research 30*(3), 186–193.

van Leer, B. (1977). Towards the ultimate conservative difference scheme III. upstream-centered finite-difference schemes for ideal compressible flow. *J. Comp. Phys. 23*, 263–275.

Vanden Broeck, J.-M. (1980). Nonlinear stern waves. *Journal of Fluid Mechanics 96*, 603–611.

Vanden Broeck, J.-M. and E. O. Tuck (1977). Computation of near-bow or stern flows, using series expansion in the Froude number. In *Second International Conference in Numerical Ship Hydrodynamics*, Berkeley, California.

Walker, D. T., D. R. Lyzenga, E. A. Ericson, and D. E. Lund (1996). Radar backscatter and surface roughness measurements for stationary breaking waves. *Proc. Royal Soc. Lond. A. 452*, 1953–1984.

Wang, Y., J. Sproston, and A. Millward (1995). A theoretical determination of the wave resistance of a fast displacement hull with a transom stern. *Journal of Ship Research 30*(2), 103–107.

White, F. M. (1991). *Viscous Fluid Flow*. McGraw Hill.

Wilson, R. and F. Stern (2005, June). URANS simulations for a high-speed transom-stern ship with breaking waves. In *Eighth International Conference on Fast Sea Transportation (FAST '05)*, St. Petersburg, Russia.

Wygnanski, I., F. Champagne, and B. Marasli (1986). On the large-scale structures in two-dimensional, small-deficit, turbulent wakes. *Journal of Fluid Mechanics 168*, 31–71.

ABSTRACT

TRANSOM STERN HYDRODYNAMICS

by

Kevin John Maki

Chair: Armin W. Troesch

The use of a transom stern on marine vehicles introduces many difficulties for the designer to predict performance characteristics. Particularly, the speed range in which the transom is partially wet is difficult to model for a full-scale ship.

In this thesis the hydrodynamics of a transom stern vessel are studied experimentally and numerically by examining the two-dimensional canonical problem of a backward-facing step with a free-surface (BFSFS). Comparisons are made with transom stern destroyer model tests, including the effects of a stern flap, to evaluate the merit of the BFSFS.

The first ever reported experiments are conducted on the two-dimensional problem in a low-turbulence water channel by measuring the free-surface by several methods including laser induced fluorescence, wire-capacitance wave probes, and a sonic probe. Additionally, velocity surveys are conducted using a pitot-tube and a special pressure-transducer apparatus which minimizes temperature and surface tension influences on very low speed velocity measurements.

Numerically, an unsteady Navier-Stokes solver is used with the Level Set method for interface tracking to simulate the BFSFS. The Spalart-Allmaras one-equation turbulence model is implemented.

The results from both experiments and numerical simulation are used to describe the free-surface in the context of four distinct flow regimes. Comparisons between the

present work and inviscid theories show that viscosity, and surface tension effects are important in predicting the wave slope. The wave-length behind the body is much shorter than predicted by linear theory. A previous stream-function bi-linear shear current theory is used to account for the viscous wake effect on the wave-length. A frequency analysis is performed that identifies a dominant vortex street occurring at a Strouhal number of 0.2.

The process of transom un-wetting is described for the canonical problem and compared to the un-wetting of the destroyer stern-flap model tests by means of assuming the pressure on the transom is hydrostatically dominated.